

Study of the Photo-Conversion Efficiency of Quantum Dots Sensitized TiO₂ Solar Cells with Visible-Infrared Absorption

Thesis in partial fulfillment of the requirements for the degree of

Doctor in Sciences (Optics)

by

M. en F. Diego Esparza

Advisor: Dr. Elder de la Rosa Cruz

León Gto., México

November 2016

Agradecimientos

Al Consejo Nacional de Ciencia Y Tecnología (CONACYT) por la beca otorgada para realizar el Doctorado en Ciencias ópticas. Al Centro de Investigaciones en Óptica (CIO) por ser como mi segunda casa y por permitirme ser parte de su programa de Doctorado en Ciencias.

Al Dr. Elder de la Rosa por permitirme ser parte de su exitoso grupo de investigación, por orientarme en cada etapa de mi investigación y por siempre estar muy atento en seguir avanzando y aportar de la mejor manera mi proceso como investigador.

A la Dra. Tzarara Lopez Luke por siempre tener tiempo de discutir y debatir resultados, por todo lo que logre aprender de ella, así como el apoyo para el desarrollo de toda mi investigación.

Al Dr. Isaac Zarazua Macias por todo el apoyo mostrado durante toda mi investigación, por compartir conmigo todos sus conocimientos en el área de celdas solares, así como por su sincera amistad.

Al Grupo de Dispositivos Fotovoltaicos y Optoelectronicos de la Universidad Jaime I, en especial al Dr. Ivan Mora Sero por permitirme realizar una estancia pre doctoral en sus laboratorios, por su entusiasmo y por todo el aprendizaje. Al Dr. Rafael Sánchez por todas sus enseñanzas en la parte de la química, así como su forma de trabajo y forma de sistemática de hacer las cosas.

Al Dr. Alejandro Torres Castro de la Universidad Autónoma de Nuevo León por recibirme en su laboratorio durante 2 estancias cortas de investigación, por su tiempo empleado para realizar los estudios de microscopia electrónica de transmisión mostrada en este trabajo de investigación.

A mi mesa de sinodales del examen pre doctoral: Dr. Ramon Carriles, Dra. Tzarara Lopez-Luke y Dra. Rosalba fuentes, así como mi mesa del examen doctoral: Dr. Luis Arturo Godínez Mora-Tova, Dr. Ramon Carriles y Dr Elder de la Rosa por sus comentarios sobre el trabajo de tesis así como su tiempo empleado en leer y sugerir los cambios pertinentes.

A la M en C, Christian Albor por su apoyo para analizar muestras por microscopia electrónica de barrido, así como al Ing. Carlos Juarez del laboratorio de películas delgadas por su apoyo en el depósito de diferentes películas, también por su buen optimismo en su trabajo.

A todo el grupo GNAFOMA que me apoyo durante todo mi proyecto de investigación.

Dedicatorias

Este trabajo se lo quiero dedicar a mi hermosa familia, a mi esposa Delia Guadalupe y a mi hijo Diego Mateo. Gracias por ser mi vida, lo que me mantiene con los pies en la tierra y ser lo más importante que tengo.

Agradecimientos

Quiero agradecer muy especialmente a mis queridos padres, mi madre Josefina Salazar Luna y mi padre Francisco Esparza Lopez, gracias por confiar en mí, ustedes son los responsables de todo lo que he logrado. A mis hermanos: Hilario, Yesenia y Lorena por esa unión que siempre hemos tenido y por permitirme ser parte de sus vidas.

Durante toda mi vida he tenido maestros que han marcado mi forma de ser y de pensar, hoy quiero agradecer a este selecto grupo de personas: al profesor Alejandro López, por inculcarme el amor al futbol y por todo el aprendizaje de su parte. Al Lic. Fernando Villalpando por todo su apoyo, por su generosidad por que saliera adelante y por permitirme ser parte de su familia. Al Dr. Iván Moreno por ser el responsable en sumergirme en el mundo de la ciencia y finalmente al Dr. Elder de la Rosa por permitirme cruzar fronteras en la ciencia e ir en busca de nuevo conocimiento, a todos GRACIAS.

Abstract

Quantum Dots (QDs) are currently being investigated for application into solar cells to enhance the cell efficiency based on the photovoltaic parameters such as photocurrent, photovoltage and fill factor. Our aim is to increase the photocurrent using different QDs, which absorption in the visible and infrared region. The most common QDs with absorption in the visible range are the Cadmium Sulphide (CdS) and Cadmium Selenide (CdSe) QDs. The effect of different sensitization techniques in the configuration $\text{TiO}_2/\text{CdS}/\text{CdSe}/\text{ZnS}$ is analyzed; with this configuration a photoconversion efficiency (PCE) of 4.7% is obtained. A strong absorption band centered at 650 nm reveals the contribution of colloidal CdSe QDs. The infrared region is studied with lead sulphide (PbS) QDs in the configuration $\text{TiO}_2/\text{PbS}/\text{CdS}/\text{ZnS}$, where we find that the infrared absorption is for the PbS, several authors use the CdS for protected the oxidation of PbS. The $\text{TiO}_2/\text{PbS}/\text{CdS}/\text{ZnS}$ QDSSCs have been compared with the efficient electron transport of the $\text{TiO}_2/\text{PbS}/\text{PFN}/\text{CdS}/\text{ZnS}$ configuration, where PFN is poly[(9,9-bis(3'-(N,N-dimethylamino)propyl)-2,7-fluorene)-alt-2,7-(9,9-dioctylfluorene)]. The PbS was used in $\text{TiO}_2/\text{PbS}/\text{PFN}/\text{CdS}/\text{ZnS}$ configuration to obtain a 3.6 % photo conversion efficiency (PCE) by the utilization of a PFN active layer, which increases short circuit current by the light scattering strategy. Moreover, the less toxicity of Bismuth sulfide (Bi_2S_3) has been applied to $\text{TiO}_2/\text{CdS}/\text{Bi}_2\text{S}_3/\text{ZnS}$ configuration instead of PbS, we found a PCE of 2.52%. It is important to note that the enhancement in the cell efficiency was explained by broadening the absorption spectra and energy level diagram to reduce the transport losses because of superficial defects. One of the most efficient colloidal materials, Cadmium Selenide Telluride (CdSeTe) QDs, was added into the $\text{TiO}_2/\text{CdS}/\text{CdSe}/\text{CdSeTe}/\text{ZnS}/\text{SiO}_2$ configuration, resulting in a record PCE of 7.4%. The general increase of absorption as well as a shift towards longer wavelengths up to 800 nm was observed clearly with the coating of colloidal CdSeTe QDs. Finally a preliminary result about perovskite solar cells and perovskite QDs is presented.

Preface

The world energy demand enhances the interest in making an economic and efficient energy solar cell. The photovoltaic cell can provide sufficient solar energy on the Earth, around 10^4 times more powerful than other energy sources as well as being environmentally friendly. The ratio efficiency/cost is the most important parameter in solar cells. Currently, the silicon solar cells exhibit a 25% of efficiency; however the cost of fabrication is high due to specific characteristics of material deposition. The third generation of solar cells based in nanomaterials present low cost in fabrication; however, the efficiency is very low. The solar cells studies with nanomaterials need to increase the efficiency of solar cells, incrementing the efficiency is analyzed with several configurations. One of the most promising materials are the quantum dots(QDs), however the use of only one type of QDs present low efficiencies, due to low absorption in the solar spectrum. In this work, the objective is the usage of different QDs in the visible and infrared absorption range and analyzes the charge carriers transport in the photovoltaic devices. The results are very promising to achieve a better efficiency with the wavelength dependent of QDs sensitized solar cells. The hypothesis is that the increment of the range absorption from visible to near infrared with the use of the QDs sensitized TiO_2 , and the use of passivated surface enhance the charge transport and in consequence increase the photo conversion efficiency.

The work is divided into 6 chapters as follows.

Chapter 1 presents the general overview of different kinds of solar cells based on nanomaterials along with a brief description on the QDs semiconductor material, quantum confinement effect, and optical properties. The architecture and physical mechanism of different quantum dots sensitized solar cells (QDSSCs) have also been described.

Chapter 2 is devoted to the description of experimental section for the preparation of TiO_2 film, colloidal QDs such as CdSe and CdSeTe, the counter electrode manufacturing, and cell assembling, for the different configuration of (QDSSCs) involved in the present investigation. Different measuring instruments and their operating conditions to study the

morphology, optical and electrochemical characteristics, and impedance spectroscopy were also explained in this chapter.

Chapter 3 explores the different configurations of QDSSCs with QDs in the visible range (CdS, CdSe). The increment of the photoconversion efficiency has been analyzed using CdS QDs and CdSe quantum rods. Different deposition techniques of the colloidal quantum rods are analyzed, the photoconversion efficiency increased due to the increment of electron transport within the material. However these types of QDs have an absorption range extending only until 650 nm. The extension to the near infrared range is possible with the use of other types of QDs.

Chapter 4 presents the results of quantum dots in the near infrared absorption range (PbS, Bi₂S₃ and CdSeTe). The first configuration analyzed is TiO₂/PbS/PFN/CdS/ZnS. Is presented an increment in the photocurrent, this increment could be attributed by increment in the sensitizer material or by the increment of the light scattering, the PbS and CdS has similar amount in the cell and their contribution could be attributed to the effect of light scattering by the PFN layer. Notice that the light scattering effect can enhance the current density, thus the cell efficiency was found to be 3.6%. Other interesting material is the Bi₂S₃ QDs, which presents lower toxicity than the PbS and its functionality is very close to the infrared absorption spectrum, however the Bi₂S₃ QDs show superficial defects. Electrochemical impedance measurements were also analyzed to understand the carrier recombination and transport processes. These types of defects on the surface depend of the QDs grown, for this reason we analyzed the results of colloidal QDs, this type of colloidal QDs reduces the superficial defects on the surface. The CdSeTe QDs extend the absorption light (800 nm) increasing the band regions in the optical absorption spectrum. The observed enhancement in the absorption of multiple QDs can increase the photocurrent of the cell. Finally, the open circuit voltage was increased by using SiO₂ layer to boost the photo conversion efficiency.

Chapter 5 explains the techniques learnt and results obtained during a one month visit to the Group of photovoltaic and optoelectronic devices in the University Jaume I, under adviser of Dr. Ivan Mora Sero in Castellon de la Plana, Spain. The work was focused to the

fabrication and synthesis of perovskite solar cells and perovskite quantum dots for a well-defined cell efficiency and Light Emitting Diode applications.

Chapter 6 Summarizes the results and conclusions that are drawn from the present investigations of the QDs in the devices. From the systematic analysis of both the present as well as earlier studies reported, it is suggested that there is a scope for further extension of the work for the better understanding and utilization of these materials to develop solar cells and light emitting diode devices.

Table of contents

Chapter 1 Introduction

- 1.1 A general overview of solar cells
- 1.2 Quantum dots
 - 1.2.1 Quantum confinement effect
 - 1.2.2 Optical properties of QDs
- 1.3 Quantum dots solar cells
 - 1.3.1 Schottky cell
 - 1.3.2 Depleted heterojunction cell
 - 1.3.3 Quantum Dot Sensitized Solar Cells (QDSSCs).

Chapter 2 Experimental section

- 2.1 TiO₂ films preparation
- 2.2 Synthesis of colloidal quantum dots
- 2.3 Methods of sensitizing solar cells
 - 2.3.1 Successive Ionic Layer Absorption and Reaction (SILAR)
 - 2.3.2 Electrophoretic method
 - 2.3.3 Pipetting method
- 2.4 Counter electrode manufacture & cell assembling
- 2.5 Characterization
 - 2.5.1 Morphological characterization
 - 2.5.1.1 Scanning Electron Microscopy (SEM)
 - 2.5.1.2 Transmission Electron Microscopy (SEM)
 - 2.5.2 Optical characterization
 - 2.5.2.1 UV-VIS absorption
 - 2.5.2.2 Fluorescence spectroscopy
 - 2.5.3 Electrochemical characterization
 - 2.5.3.1 JV curves
 - 2.5.3.2 Incident Photon to Current Efficiency (IPCE)
 - 2.5.4 Electrochemical impedance spectroscopy

Chapter 3. Quantum dots sensitized solar cells with absorption in the visible region.

- 3.1 Introduction
- 3.2 Solar cells photoanodes fabrication
- 3.3 Morphological characterization
- 3.4 Optical characterization
- 3.5 Electrochemical characterization
 - 3.5.1 CdS and CdSe quantum dots sensitized solar cells
 - 3.5.2 Combination of CdS/CdSe quantum dots sensitized solar cell
 - 3.5.3 Effect of ZnS in quantum dots sensitized solar cells
- 3.6 Electrochemical impedance

Chapter 4. Near infrared absorption of quantum dots sensitized solar cells

- 4.1 Introduction
- 4.2 Solar cells photoanode fabrication
- 4.3 Lead sulfide quantum dots sensitized solar cells
 - 4.3.1 Morphological characterization
 - 4.3.2 Optical characterization
 - 4.3.3 Electrochemical characterization
- 4.4 Bismuth sulfide (Bi_2S_3) quantum dots sensitized solar cells
 - 4.4.1 Optical characterization
 - 4.4.2 Electrochemical characterization
 - 4.4.3 Electrochemical impedance
- 4.5 Colloidal CdSeTe QDs
 - 4.5.1 Morphological characterization
 - 4.5.2 Optical characterization
 - 4.5.3 Electrochemical characterization
 - 4.5.3.1 CdS and CdSeTe QDSSCs
 - 4.5.3.2 CdS/CdSe/CdSeTe QDSSCs
 - 4.5.3.3 Tunable absorption of CdSeTe QDs
 - 4.5.4 Electrochemical impedance

Chapter 5. Perovskite devices

- 5.1 Introduction
- 5.2 Perovskite quantum dots
 - 5.3.1 Synthesis of perovskite quantum dots
 - 5.3.2 Optical characterization
- 5.2 Perovskite solar cells
 - 5.2.1 Fabrication of perovskite solar cells
 - 5.2.2 Morphological characterization
 - 5.2.3 Optical characterization
 - 5.2.4 Electrochemical characterization
 - 5.2.5 Perovskite quantum dots solar cells
- 5.3 Application in light emitting diodes

Chapter 6 Conclusions

Publications

References

Chapter 1

Introduction

1.1 A general overview of solar cells

Recently, there has been an enormous surge for finding economic and efficient energy sources to meet future energy needs. The energy needs are increasing in the coming years and the progressive environmental pollution is affecting the global warming. The world energy crisis has been a key factor for the development of new techniques and devices that can exploit sources of renewable energy. At present, around 18 TW of energy are required annually, 80% of this energy is provided by fossil fuels [1]. However, the use of fossil fuels produces some alarming effects such as, generation of carbon dioxide, methane and ozone thus leading to global warming and increased environmental pollution. The global increment in the use of energy is linked with the increment in the world population. It is estimated that by 2050 our global energy requirements will rise to 26.4-32.9 TW per year [2, 3]. Some of the most sustainable sources of energy are the renewable resources like: geothermal (12 terawatts (TW) per year), hydroelectric power (1.5TW per year) and solar energy (120,000 TW per year). Solar energy is an interesting candidate to be used as friendly energy alternative. The photovoltaic cells have attracted significant attention due to its enormous potential since incident solar energy on the earth is 10^4 times more powerful than other renewable energy resources as well as being environmentally friendly [2, 4].

The first photovoltaic device was developed in 1954, this solar cell was based on silicon and showed a photo conversion efficiency (PCE) of 6% [5]. The most common solar cells are based on silicon, having a PCE of 25.6% [6]. However, the manufacturing process is expensive.

In the last years, nanomaterials or nanostructures have emerged as promising alternatives for harvesting solar energy [7-10]. Three types of solar cells based on nanostructured materials are studied: 1) Organic solar cells, based on molecules or semiconducting polymers with some carbon nanostructure [11-14] having a record efficiency of 11.5% [6]; 2) Inorganic solar cells, based on inorganic semiconductor nanomaterials sensitized with another semiconductor or metallic nanoparticles [15-17]; 3) Hybrid solar cells, based on a mixture of organic-inorganic nanostructures taking advantage of the best properties of each component and possible synergetic effects [18, 19]. Actually this type of solar cell has a the world record efficiency of about 21% with the use of lead iodide perovskite in the solar cells [20-22].

In 1991, a novel type of low cost solar cell fabricated using dye adsorbed on nanocrystalline titanium dioxide (TiO_2) film as photoanode was reported. Due to this composition it was named, Dye Sensitized Solar cell (DSSC) [7, 23-29]. The first DSSC have a PCE of 7% under simulated sunlight irradiation [7]. Currently this type of solar cell presents a PCE of 13% using a molecular porphyrin dye [30] and it is possible to increase the PCE of DSSCs by using different methods. One alternative is to enlarge their light absorption into the near infrared (NIR) region.

The design of photovoltaic cells involves different types of technologies like silicon solar cells, thin films solar cells, polymer solar cells, organic solar cells and sensitized solar cells. In recent years, the sensitized solar cell has been a point of attraction for increasing the energy conversion efficiency of solar cells. The sensitized solar cells are divided in two groups namely: DSSCs based on organic dyes as photosensitizer and QDSSCs with QDs as photosensitizer. Comparing QDSSCs to the DSSCs, QDs have a potential to enhance the cell stability, and their special multi-electron generation character can enable the theoretically maximum efficiency to be as high as 44% [31], much higher than that of DSSCs.

1.2 Quantum Dots

The Quantum Dots (QDs) are a semiconductor crystalline material whose diameter of particle is of the order of several nanometers (2-10 nm), experiencing quantum confinement in all three spatial dimensions. QDs has come to focus in many areas of applications like biomarkers [32, 33], light emitting diodes [34, 35], and photovoltaic devices [36, 37]. These applications are due to the unique electronic and optical properties of QDs. The QDSSCs are an interesting research topic towards low-cost and photostable cell development because the QDs have high molar extinction coefficient and size depend optical properties [38, 39]. Other advantages of QDs are multi-electron generation [40], with which it is possible to obtain a maximum theoretical efficiency of 44% which is much higher than DSSCs. Currently the efficiency of QDSSCs (11%) [41-43] is still lower that of the DSSCs (13%) [29, 44, 45]. This is probably due to the loss of electrons between electrolyte and photo-electrode and the narrow absorption spectra of QDs. To increase the PCE in QDSSCs, it is necessary to develop properties of QDs referring to light harvesting ability, increasing electron transport rate and decreasing charge recombination in the device. One of these parameters, the increase in light harvesting ability, is associated with the quantum confinement effect in QDs.

1.2.1 Quantum confinement effect

The quantum dot behavior can be explained using quantum mechanics. The Schrödinger equation describes the wave function of a particle, in essence the most complete description possible of the particle [46]:

$$-\frac{\hbar^2}{2m}\nabla^2\Psi(r) + V(r)\Psi(r) = E\Psi(r)$$

where \hbar the Planck constant, m is the mass of particle and ∇^2 is the Laplacian operator:

$$\nabla^2 = \frac{\partial^2}{\partial x^2} + \frac{\partial^2}{\partial y^2} + \frac{\partial^2}{\partial z^2},$$

$\Psi(r)$ describes the wave function of the particle. Suppose, we consider a particle confined to a three-dimensional box, which is the representation of a quantum dot.

The length of the edges in the x,y and z dimensions are L_x , L_y and L_z . The wave function from the Schrödinger equation is derived to be:

$$\Psi_{n_x,n_y,n_z}(x,y,z) = \sqrt{\frac{2}{L_x} \frac{2}{L_y} \frac{2}{L_z}} \sin\left(\frac{n_x\pi}{L_x}\right) \sin\left(\frac{n_y\pi}{L_y}\right) \sin\left(\frac{n_z\pi}{L_z}\right)$$

The exact eigenvalue solution is:

$$E_{n_x,n_y,n_z} = \frac{h^2\pi^2}{2m} \left(\left(\frac{n_x}{L_x}\right)^2 + \left(\frac{n_y}{L_y}\right)^2 + \left(\frac{n_z}{L_z}\right)^2 \right)$$

Assuming that $L_x=L_y=L_z=L$, this becomes.

$$\Psi_{n_x,n_y,n_z}(x,y,z) = \left(\frac{2}{L}\right)^{3/2} \sin\left(\frac{n_x\pi}{L}x\right) \sin\left(\frac{n_y\pi}{L}y\right) \sin\left(\frac{n_z\pi}{L}z\right)$$

$$E_{n_x,n_y,n_z} = \frac{h^2\pi^2}{2mL^2} (n_x^2 + n_y^2 + n_z^2)$$

Because h and π are constant, m is the particle mass, which is known for an electron, L is a numerical length of the box and n_x , n_y and n_z , the eigenvalue, E_n (energy value of an energy state) demonstrate that for any integer n (i.e. 0,1,2,3) there are corresponding, discrete energy states. Moreover, the energy value E of the eigenvalue is inversely proportional to the square of edge length L of the cube, which mathematically represent the phenomenon of three dimensional quantum confinement: as the cube become increasingly confined (L is decreased) the energy increases.

1.2.2 Optical properties of QDs

When a bulk semiconductor material gradually decreases in size to a critical size (Bohr radius), quantum confinement effect occurs. The movement of the carriers will be strongly quantum limited. At the same time the density of electron states is changed from a continuous energy band of bulk material into quasi-discrete energy levels, similar to molecules. The band gap of the QD is increased with the increment in the quantum confinement effect. A smaller size of the QDs will lead to

a stronger quantum confinement effect. When the size of the QDs decreases, the bandgap and the splitting of the energy bands increase, making the optical spectrum to blue-shift with a more molecule-like behavior. As a result, the strong size-dependent optoelectronic properties of QDs make it possible to tune the absorption and PL of QDs by tuning the size (see Figure 1-1).

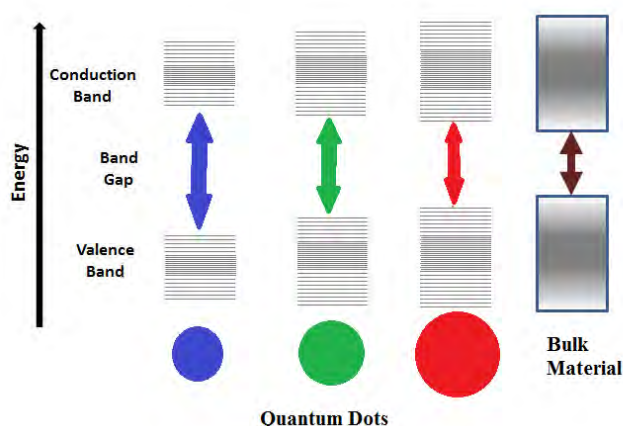


Figure 1-1. Schematic image of the energy bands as a function of particle size.

The properties of the semiconductors nanoparticles can be controlled by size, but also by shape. When the charge carriers experience quantum confinement in one dimension, the energy is only continuous in the two dimensional space, these materials are called quantum wells or quantum films. Similarly, when the carriers are confined in the two dimensional space and the energy is only in one dimensionally continuous, these materials are named as quantum wires or quantum rods (QRs). When the carrier is confined in all the three spatial directions, these materials are termed QDs, whose energy is completely quantized. The QDs and QRs have quantum effect, which results in unique optical properties like absorption and luminescence.

As shown in Figure 1-2, the absorption spectra of QDs changes with the size of the QDs.

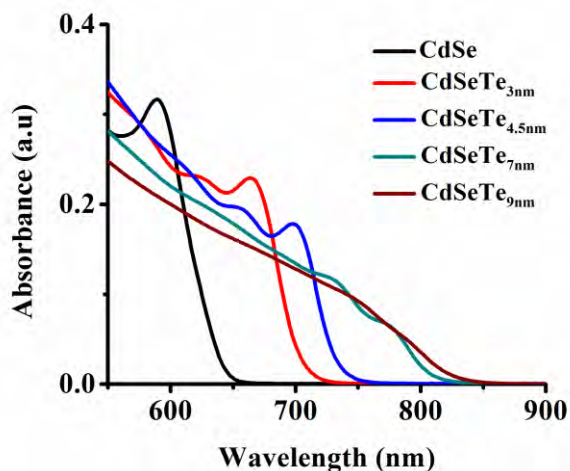


Figure 1-2 Absorption spectra of QDs with different sizes, the sub index shows the size of the QDs.

Similarly, the photoluminescence spectrum presents a different peak of emission, depending of the QDs size (see Figure 1-3).

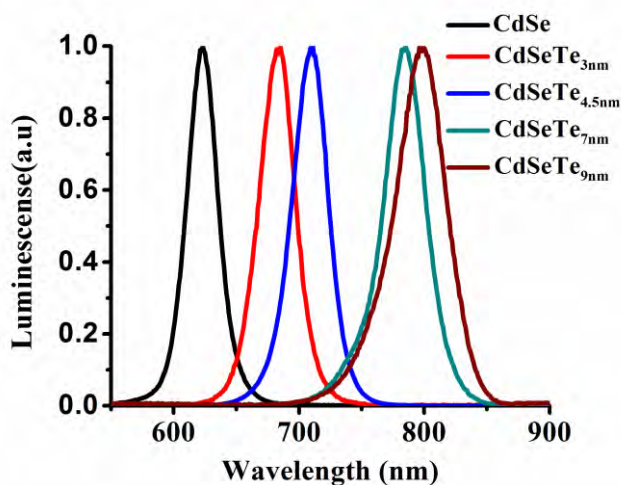


Figure 1-3 Photoluminescence spectra of QDs with different sizes.

When the QDs increase in size, the absorption and luminescence peak continuously shifts to the red. This behavior is caused by the decrease of QD bandgap. The decrease of bandgap is due to the increase in the QD size.

The size dependent optical properties and bandgaps of the semiconductor QDs derive from quantum confinement, and hence the QDs can be considered as

materials having properties intermediate between molecules and bulk material. Figure 1-4 shows the reduction in bandgap of the QDs with an increment in size of QDs, coming from a quantum confinement effect.

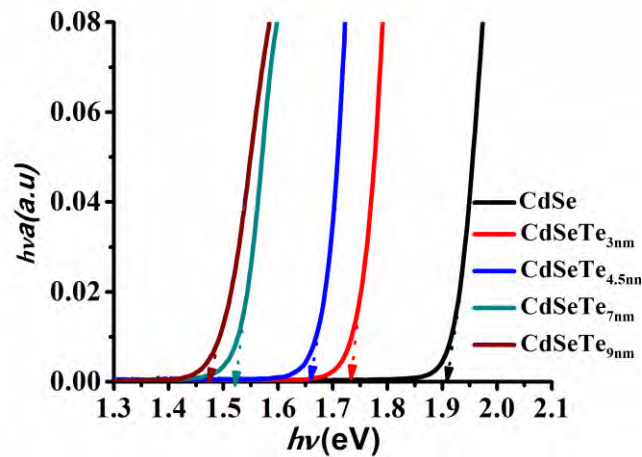


Figure 1-4. The Band Gap depends of the QDs size, when the QDs increase the band gap is reduced.

Due to the size-dependent effect, the size of QDs has become an important parameter for their development. Another point is the shape, which induces different optical properties, and for example the QRs, which are rod-like nanocrystals, with quantum confinement in two dimensions. The optical properties in this type of materials depend on the dimensions and the electronic levels which are further decided by the size of the smallest axis.

On the other hand, the quantum confinement of the materials depends on the Bohr radius in the materials, however in the case of the ternary or quaternary materials it is possible to change the optical properties with the concentration composition.

QDs have several applications in light emitting diodes [47, 48] bio labeling, bio sensing [49], imaging detection [50] and solar cells [51, 52] .

1.3 Quantum dots solar cells

Solar cells based on QDs are classified depending of its architecture such as 1) Schottky Cell, 2) depleted heterojunction cell and (3) Quantum Dot Sensitized Solar Cells (QDSSCs).

1.3.1 Schottky Cell

Figure 1-5 depicts the structure of a Schottky cell, which is composed of a conducting material contact interface, the QDs for absorbing light and Aluminium (Al) as metal contact. The interaction between the light and the QDs determines the absorption of light which generates the electron-hole. The electron then moves to the conduction band and the hole to the valence band. The next process is the injection of electron in the metal contact (Al) and the hole to photoelectrode. In this type of solar cell, the layer of QDs is sandwiched between the two conductive substrates. A low work function metal and a conducting glass are employed to collect the photogenerated electrons and holes, respectively.

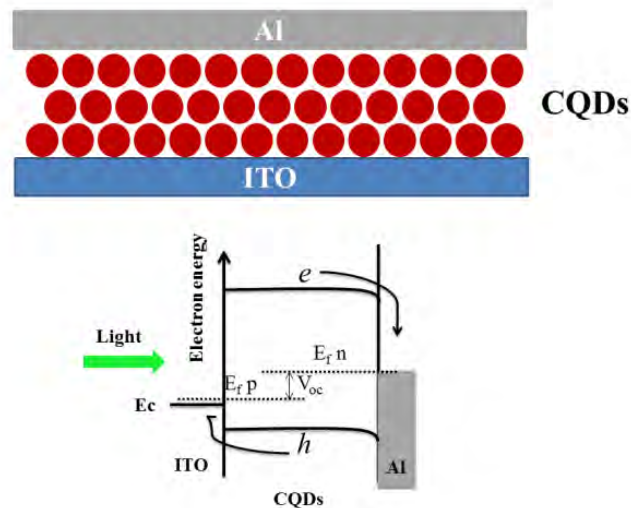


Figure 1-5 Schematic structure of Schottky cell.

1.3.2 Depleted heterojunction cell.

This type of solar cell is similar to the Schottky cell; however in this case, a wide bandgap n-type semiconductor is included. This layer is introduced between the conductive glass and the QDs (See Figure 1-6). In this case, the electrons flow towards the nanoporous oxide and the corresponding holes toward the metal. This type of solar cells is very similar to the organic heterojunction cell. The difference is that in organic cell, the active layer is a blend of two polymers, one acts as an electron donor and the other as an acceptor. The charge carrier is photogenerated near the interface between the two polymers.

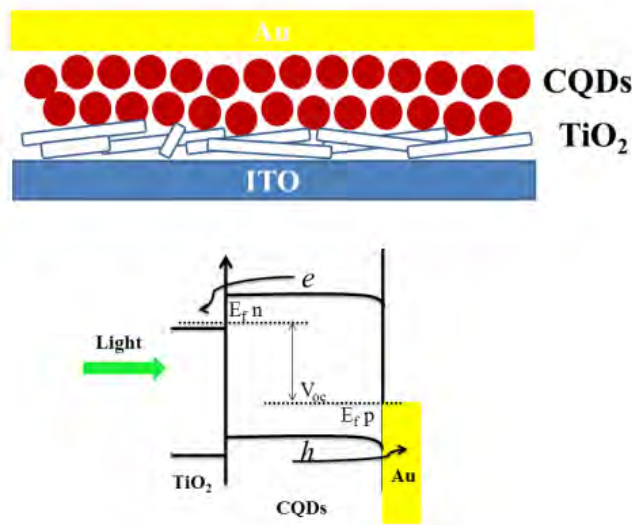


Figure 1-6. Schematic Structure of Depleted Heterojunction cell

1.3.3 Quantum dot sensitized solar cells.

These cells typically consist of TiO_2 NanoCrystals (NCs) acting as a highly porous wide bandgap semiconductor for electron collection, and dye molecules adsorbed on the surface of the TiO_2 NCs acting as sensitizers to harvest solar light. The operational mechanics is described in the next subsection. This type of cell are named Dye Sensitized Solar Cells (DSSC). The difference between DSSCs and the QDSSCs is that the dye is replaced by QDs. Figure 1-7 shows the typical QDSSCs, with a TiO_2 as a wide bandgap semiconductor or electron acceptor and an electrolyte as hole regenerator.

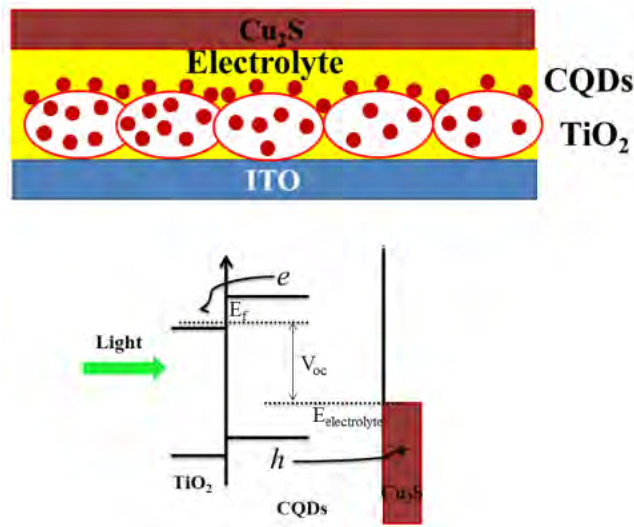


Figure 1-7. Schematic structure of quantum dot sensitized solar cells

The structure of QDSSCs is shown in Figure 1-8 [53], the QDSSCs consists of three parts namely, the photoelectrode, the electrolyte and the counter electrode. The photoelectrode is generally fabricated through the deposition of a layer of mesoporous monocrystalline semiconductor material (TiO₂, ZnO₂ or ZrO₂) on a conductive substrate (FTO or ITO). Next is the adsorption of the QDs onto the mesoporous semiconductor. The electrolyte is a liquid containing a redox couple (S^{2-}/S_x^{2-}), filling the space between the photoelectrode and the counter electrode to transport carriers. Finally the counter electrode is a passive electrode, normally a conductive glass coated with a catalyst layer (Pt, Au, Cu₂S), for the charge exchange between counter electrode and electrolyte.

The research in this field is focused principally on four strategic lines: the sensitizer materials, the interface between the wide semiconductor (TiO₂, ZnO or ZrO₂) with the QDs and electrolyte, the redox electrolyte, and the counter electrode.

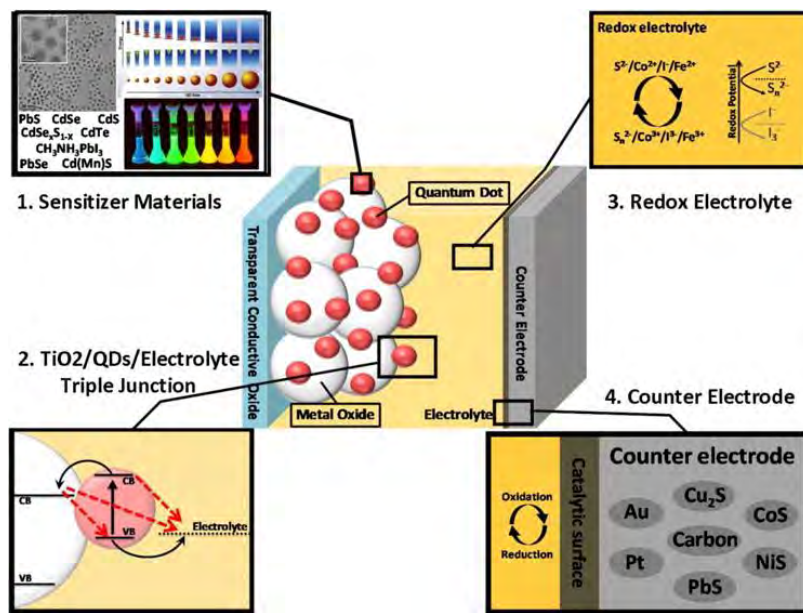


Figure 1-8. Schematic representation of QDSSCs (taken from[53]).

The sensitizer material is the most studied with different types of QDs (CdSe, CdTe, CdS, PbS, PbSe, Bi₂S₃, and InP) [15-17, 54-62]. Other configurations have been employed by mixing two different QDs, for example CdS/CdSe [63-67], CdS/CdTe [68, 69], PbS/CdS [70-72] configurations, improving the performance of QDSSCs. Another kind of QDs that has been implemented successfully is the ternary alloy, such as CdSe_xS_{1-x} [73, 74], CdSe_xTe_{1-x} [43, 75-77], or the use of core shell QDs such as CdSe/CdS [78, 79], CdTe/CdS [80], ZnTe/CdSe [81-83], CdSeTe/CdS [84-86], resulting in the rapid increase of QDSSCs conversion efficiency (~10%).

The increment of photovoltaic efficiency in QDSSCs depends on the internal physical process within the cells. These dynamics are the charge transfer processes occurring in the interface between the nanostructured TiO₂, the QDs sensitizer, and the aqueous polysulfide electrolyte [87-89]. Basically these physical processes are the transport resistance, the recombination resistance and the chemical capacitance in the cell and they are analyzed by Electrochemical Impedance Spectroscopy (EIS).

The work of the electrolyte solutions is to regenerate the oxidized QDs sensitizer by donating an electron. A good electrolyte with a redox mediator is

necessary in QDSSCs. The most common electrolyte is I^-/I_3^- redox couple, since it is the standard electrolyte for Dye Sensitized Solar Cells [29, 90, 91]; however, in QDSSCs the most used electrolyte is polysulfide due to corrosion of the semiconductor QDs caused by the I^-/I_3^- redox couple. Polysulfide electrolyte demonstrates high regeneration rates of oxidized QDs [92]. Other type of electrolytes used in QDSSCs are cobalt polypyridyl-based redox electrolytes [29].

The Counter electrode is the responsible for the discharge of electrons quickly. There exists various types of counter electrodes: Au [64], Cu_2S [93-96], CoS [97, 98], Pt [99, 100], NiS [97, 101], PbS [102, 103] and Bi_2S_3 [104].

Upon illumination, light is absorbed by the QDs promoting an electron from the Valence Band (VB) to the Conduction Band (CB) leaving a hole in the VB, and producing an exciton (electron-hole bounded state). Then, the electron has two possibilities, the first is to recombine with the hole, and the second is the injection to the wide semiconductor oxide. Depending on the application, the configuration of the device is chosen; for example, if the application is light emitting diode, the recombination process is important. However for solar cells, it is necessary that the CB of the wide semiconductor be lower than the CB of QDs, This condition increases the electron injection in a wide semiconductor. The working principle and typical energy diagram level structure of QDSSCs are shown in Figure 1-9.

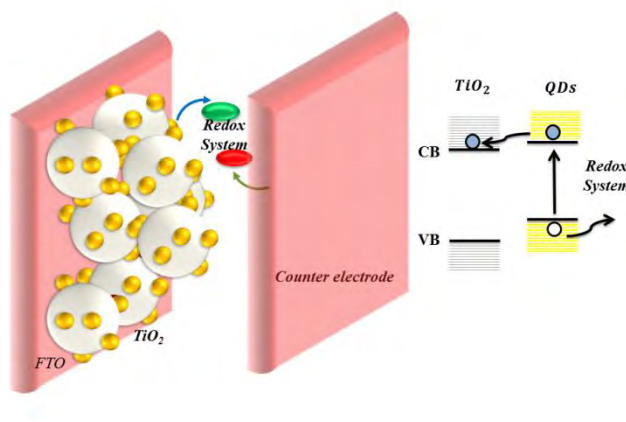
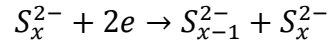
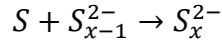
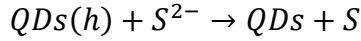
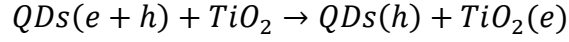
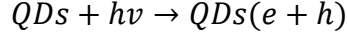


Figure 1-9. Schematically representation of QDSSCs with representative energy level diagrams.

The photogenerated holes are injected to the electrolyte and thus the QDs are restored. The oxidation species of the electrolyte diffuses to the counter electrode and is reduced by the migrated electrons from the external circuit. The electron-hole transfer dynamics can be expressed according to the following equations [15, 64]:



Other important parameters under consideration are the physical process in the QDSSCs when the hole and electron have been photogenerated in the QDs. The principal physical process are: 1) the excitation electron may be is recombination with the hole, 2) charge injection from an excited QD into TiO_2 , transport of electrons to the collecting electrode surface, 3) hole transfer to the redox couple, 4) regeneration of the redox couple, 5) recombination of electrons from the QD and the oxidized form of the redox couple, and 6) interfacial recombination of electrons from TiO_2 and the oxidized form of the redox couple. (Figure 1-10). The interfacial states formed at grain boundaries again produce recombination in the system, the interfacial states depend of the quality of crystallinity, nanostructure with good crystallinity present low interfacial states.

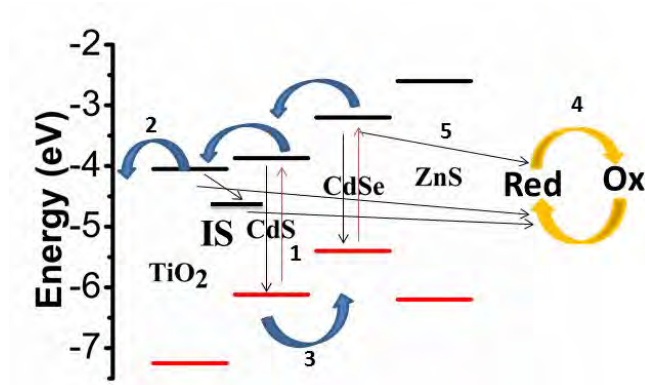


Figure 1-10 Schematic of the different physical process in the solar cells.

Chapter 2

Experimental Section and Characterization

2.1 TiO₂ films preparation

Materials: TiO₂ Paste (WER2-0 Reflector) and TiO₂ Paste (DSL 18NR-T) were purchased from DYESOL. Titanium (IV) isopropoxide (97%), acetylacetone (>99%), and fluorine-doped tin oxide (FTO), dimension 100 mm x 100 mm x 1.1 mm, resistivity of 7-10 ohm/sq, thickness of 250 nm and visible transmittance of 80-85% from MTI (TEC-15).

TiO₂ film Preparation. The FTOs were cleaned with water, acetone and ethanol in an ultrasonic bath for 15 min, before deposition of the TiO₂ films. The TiO₂ photoelectrodes were prepared by depositing three different layers stacked on one another. The first was a compact layer which was deposited as follows: a solution of titanium (IV) isopropoxide (0.2 M) with acetylacetone and ethanol (1:1,V:V) was deposited by spray pyrolysis over FTO to obtain a 150 nm thick layer, see Figure 2-1.1. The second film was a TiO₂ transparent layer, and consisted of TiO₂ paste, (DSL 18-NRT, 20 nm average particle size) deposited by Doctor Blade method obtaining a 9 μm thick layer, see Figure 2-1.2. The third layer was a scattering layer (opaque) obtained by depositing a 8 μm thick layer of Wer2-O Reflector paste (400 nm particle size) by Doctor Blade. All films were sintered for 30 min at 450 °C to obtain a good electrical contact between nanoparticles, see Figure 2-1.3.

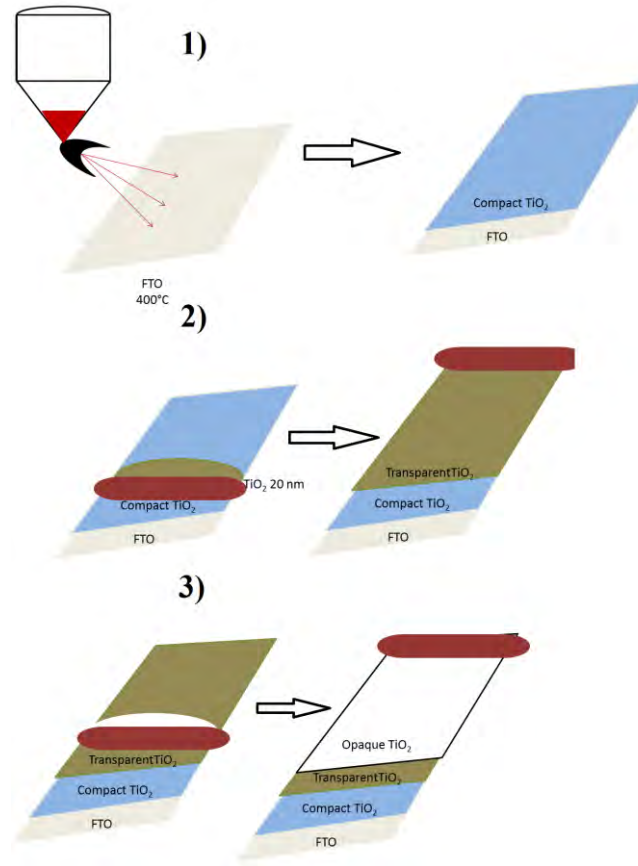


Figure 2-1. 1) Deposition by spray pyrolysis of the compact layer over the FTO substrate. 2) TiO_2 transparent layer, TiO_2 paste, (DSL 18-NRT, 20 nm average particle size) deposited by Doctor Blade method. 3) Scattering layer (opaque) obtained by depositing a 8 μm layer of Wer2-O Reflector paste (400 nm particle size) by doctor blade.

2.1.2 Synthesis of colloidal quantum dots

Materials: Technical-grade trioctylphosphine (TOP 90%), trioctylphosphine oxide (TOPO 99%), sodium sulfide (Na_2S 99%), cadmium oxide (CdO 99%), selenium powder (Se 99%), tellurium powder (Te 99%), 1-tetradecylphosphonic acid (TDPA 99%), all the materials were obtained from Sigma-Aldrich.

CdSe QRs: High-quality CdSe QRs and CdSeTe QDs were synthesized based on the protocol designed by Peng *et al* [105]. The CdO is used as Cd precursor; TDPA and TOPO are the ligands and coordinating solvents, respectively. The synthesis was performed in air-free conditions, wherein 0.05 g (~ 0.39 mmol) of CdO, 0.3 g (~ 1.1 mmol) of TDPA, and 4 g of TOPO were heated to 110 $^\circ\text{C}$, degassed under vacuum and then heated to 320 $^\circ\text{C}$ under

nitrogen flow [15]. A Se-TOP solution was prepared by adding 0.026 g of Se powder in 4.25 ml of TOP. After reaching 320 °C, the Cd-TDPA-TOPO solution was cooled to 270 °C prior to the injection of Se-TOP. Under nitrogen flow, 3 ml of Se-TOP was injected, and the temperature was then increased to 280 °C to facilitate particle growth. After this, the QRs were washed using methanol and dispersed in toluene.

CdSeTe QDs: CdO is used as Cd precursor; TDPA and TOPO are the ligands and coordinating solvents, respectively. A (Se-Te) TOP solution was prepared by adding 0.026 g of Se and 0.04 g of Te powder in 4.25 ml of TOP and stirring for 1 h to completely dissolve the Se-Te powders. It is worth to notice that the size of the CdSeTe QDs was tuned by changing the amount of Se used to prepare the (Se-Te)TOP solution. Four different sizes of CdSeTe QDs were prepared using the following amounts of Se 0.026 gr, 0.052 gr, 0.114 gr and 0.132 gr. The samples fabricated with those quantities were named as CdSeTe₆₈₄, CdSeTe₇₁₀, CdSeTe₇₈₄ and CdSeTe₈₀₀, correspond in size to 3, 4.5, 7 and 9 nm respectively.

2.3 Methods for deposition of sensitizer in solar cells

2.3.1 Successive Ionic Layer Absorption and Reaction (SILAR) method

This method is to directly grow QDs onto the electrode, following the next step: the TiO₂ electrode is introduced into a precursor material, for example cadmium acetate dissolved in ethanol, and subsequently into the reaction material for example a sodium sulfide solution to synthesize cadmium sulfide QDs (see Figure 2-2a). A single SILAR cycle consisted of 1 min dip-coating the TiO₂ electrode into the cadmium acetate and subsequently into the sodium sulfide solutions, also during 1 min. Between each dipping step, the electrodes were thoroughly rinsed by immersion in the corresponding solvent, in order to remove the excess of precursor.

Compare to the colloidal QDs, the QDs prepared by SILAR facilitates the electron injection into TiO₂, increasing the interaction between QDs and electrolyte due to not use organic ligand and the electrolyte can penetrate into the pores of TiO₂. The disadvantage is that present high surface defects and increase the recombination in the system.

2.3.2 Electrophoretic method

The photoanode (TiO_2 layers) cell was placed face to face with an FTO at a distance of 0.2 cm and immersed in a cuvette with 2.5 ml of colloidal QDs dispersed in toluene. 200 DC volts were applied, with the TiO_2 films in the positive terminal of the power supply. After 105 min the colloidal QDs are uniformly distributed on the surface of the TiO_2 NPs (see Figure 2-2b).

2.3.3 Pipetting method

The TiO_2 films were masked with tape with a circular aperture of 6.0 mm in diameter. Then, one drop (20 μL) of colloidal QDs was pipetted onto the TiO_2 film surface and after 15 min one drop of MPA:methanol (3:10 V:V) solution (20 μL) was pipetted on the decorated film. This process was repeated 10 times (See Figure 2-2c).

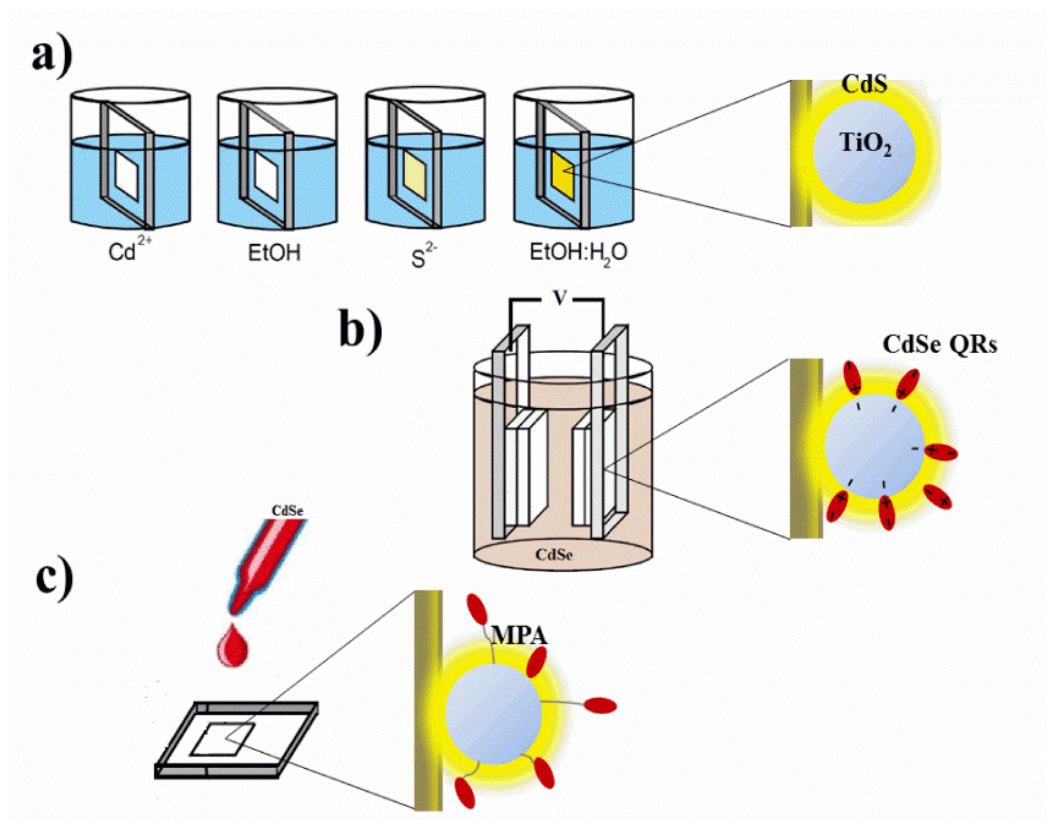


Figure 2-2. Schematic diagram of the different techniques used for deposition of QDs in TiO_2 film. **a)** Successive Ionic Layer Adsorption and Reaction (SILAR) method, **b)** electrophoretic method, **c)** pipetting method.

2.4 Counter electrode manufacture & cell assembling

Cu₂S counter electrodes were obtained by immersing brass foil in a HCl solution (38% in volume) at 90 °C for 1 hour. Then they were sulfated by adding a drop (20 µl) of polysulfide electrolyte. The composition of polysulfide electrolyte was 1.0 M Na₂S, 1.0 M S and 0.1 M NaOH dissolved in distilled water. The solar cells were constructed by assembling the Cu₂S counter electrode and sensitized TiO₂ film electrode with a binder clip separated by a Scotch spacer. Finally, the cells were filled with polysulfide electrolyte.

2.5 Characterization

2.5.1 Morphological characterization

2.5.1.1 Scanning Electron Microscopy (SEM)

It is possible to obtain detailed information about the morphology and composition of the different QDSSCs under study by microscopic techniques. Scanning electron microscopy is used to obtain surface images of the sample. In this technique, the electrons interact with the atoms on the surface, producing different signals, including backscattered electrons, secondary electrons and other types of signals.

In SEM is only analyze backscattered and secondary electrons. Secondary electrons is produced by the interaction between the beam electron and electrons near the surface of the samples. These electrons not have information about specific atoms and not contain information about the specific element o material. These present onlu information about the surface topography. The backscattered electrons, the beam electrons are reflected from the sample by scattering and are more energetic than secondary electrons. From this electrons, a compositional analysis of the sample can be obtained, for this reason is name electron dispersion spectroscopy (EDS) analysis

These images contain information about the morphology, size, shape and composition. SEM images were obtained from a JEOL JSM-7800F microscope and electron dispersion spectroscopy analysis was done with Oxford Instruments.

2.5.1.2 Transmission Electron Microscopy (TEM)

Transmission electron microscopy is similar to SEM; however, a more energetic beam of electrons is used to scan the sample, the electrons passing through it are the ones utilized to create the sample image on a fluorescent screen,. When the incident electron beam is transmitted through the sample, parts of its intensity are lost due to interactions with the sample [106]. This intensity loss is greater for thicker regions of the sample or regions with specimens of higher atomic number. The intensity loss, correspond to the dark area in the fluorescent screen, the image is complete when is considered the scattering processes and interaction by the electron flux passing through the sample. The TEM images of the sample surface consist of a wide range of grays because of the different scattering processes and interactions experienced by the electron flux and the sample. Transmission electron microscopy was obtained from a Transmission electron microscope JEOL2010F at 200 kV. The samples were suspended in methanol and chloroform (1:1) at room temperature and dispersed with ultrasonic agitation in an effort to separate the nanoparticles. Then, an aliquot of the solution was dropped on a 3 mm diameter lacey carbon copper grid.

2.5.2 Optical characterization

2.5.2.1 UV-VIS absorption

Ultraviolet-Visible (UV-Vis) absorption spectroscopy is used to characterize the light harvesting capability of the QDs in colloidal solution and deposited in the films. It is possible to obtain information about the size and the bandgap of the QDs from the UV-Vis spectrum [107]. The UV-Vis absorption spectra of colloidal CdSe QRs and CdSeTe QDs were measured by transmittance. This technique is the fraction of incident light at a specified wavelength that passes through a sample. The QDs deposited in the films is measured by diffuse reflectance. This technique is used for scattering samples, in this case is necessary to use an integrated sphere with a highly dispersive material that concentrate the light scattering by the sample in a detector, this measurement is obtained in the range from 360 nm to 800 nm using an Agilent Technologies Cary Series UV-Vis-NIR spectrophotometer (Cary 5000).

2.5.2.2 Photoluminescencespectroscopy

The phenomena of photoluminescence involve the absorption of energy in any semiconductors materials, in consequent is obtain emission of light, for example the QDs materials emit light when excited light are radiated [108] . Fluorescence is a form of luminescence. An electron in the substance absorbs a photon, followed by excitation from the ground state to the excited state and then relaxation to one of the various vibrational levels of the ground state, resulting in fluorescence. The measurement is by a fluorimeter, the fluorimeter is a devise used for measurement the light intensity and wavelength distribution of emission spectrum after excitation by a certain spectrum of light.

2.5.3 Electrochemical characterization

2.5.3.1 JV curves

The photocurrent in a solar cell involves two processes. The first process is the absorption of light to create electron-hole. These are generated in the solar cell when the incident photon has energy greater than that of the band gap. However one possible path for the electron-hole is recombination, in this case photocurrent is not generated. The second processes is the collection of charge carrier, this parameter increase if use a layer that separate electron and holes. In our case the charge carrier is separated; the electron is injected on the TiO₂ layer and the hole in the electrolyte.

The photoconversion efficiency (PCE) is the most important indicator to evaluate a solar cell. The PCE is defined as the ratio between the maximum electrical powers obtained from the solar cell to the incident light power. The PCE is obtained from the JV curves. The JV curve of a solar cell consists in applying a voltage sweep to the cell under illumination while measuring the photocurrent response as shown in Figure 2-3. The power is defined by the product between the current density and voltage, and then the maximum electrical power is the maximum value of this product, the rate between this value and the input intensity light define the photoconversion efficiency.

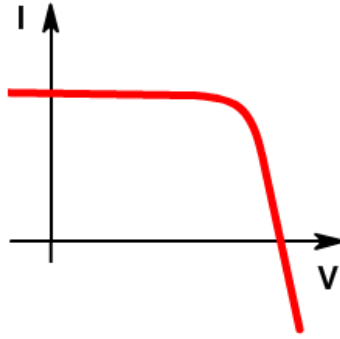


Figure 2-3 Typical IV curves for solar cells

In such a plot three parameters can be calculated that describe the internal processes in the cell. These parameters are the short circuit current, open circuit voltage and fill factor [109], see figure 2-4.

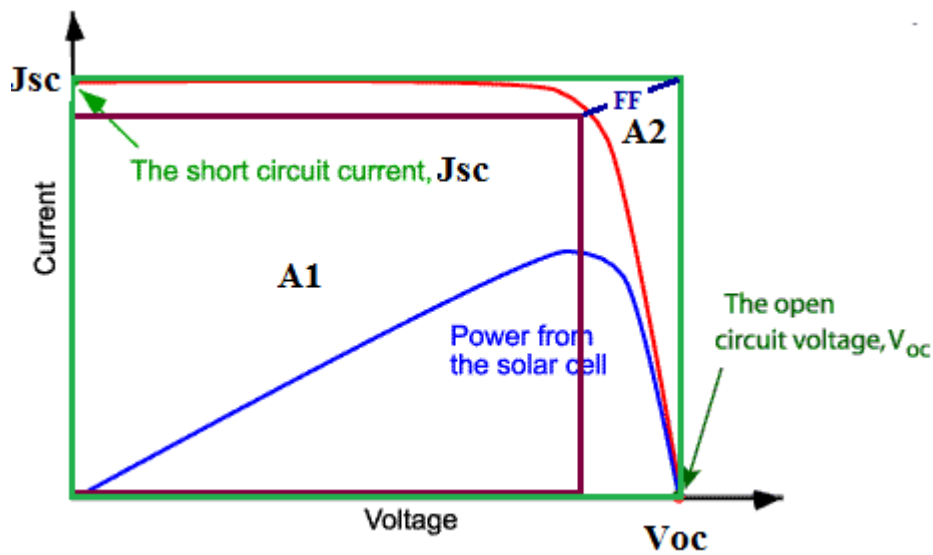


Figure 2-4 Parameters extracted from the JV curve of a solar cell: short circuit current (J_{sc}), open circuit voltage (V_{oc}) and Fill Factor (FF).

Short circuit current (J_{sc}): It is the current through the solar cell when the voltage across the solar cell is zero (i.e., when the solar cell is short circuited) and is the maximum current from a solar cell.

The J_{sc} is defined by the external quantum efficiency (QE) of the solar cell. $QE(E)$ is the probability that an incident photon of energy E will produce one electron to the external circuit. The J_{sc} is defined by:

$$J_{sc} = q \int b_s(E)QE(E)dE$$

Where $b_s(E)$ is the incident spectral photon flux density, the number of photons of energy in the range E to $E+dE$ which are incident per unit area in unit time, q is the electronic charge. QE depends upon the absorption of material, the efficiency of charge separation and transport, and the charge collection in the devices. Notice that J_{sc} depends on the photoabsorption of the cell and the light spectrum shape (b_s).

Open Circuit Voltage (V_{oc}): It is defined as the maximum voltage available from a solar cell and is obtained at a current equal to zero. The V_{oc} is determined by the maximum energy difference that can exist between electrons and holes when extracted from the solar cell. In QDSSCs, it is determined by the alignment of energy levels of the different materials in the cells [109]. If the energy levels alignment and the band gap are modified then V_{oc} changes, which in turn affects the other parameters in the cell.

When voltage is applied to the device, under dark conditions, the JV curve is obtained. The current depends on the voltage through the following equation [109]:

$$J_{dark}(V) = J_0 \left(e^{\frac{qV}{K_B T}} - 1 \right)$$

where J_0 is a constant, K_B is Boltzmann's constant and T is the temperature in degrees Kelvin. When the device is under illumination, the photocurrent obtained in the cell can be approximated as the sum of J_{dark} and J_{sc} , then:

$$J = J_{sc} - J_{dark}$$

$$J = J_{sc} - J_0 \left(e^{\frac{qV}{K_B T}} - 1 \right)$$

When the contacts are isolated, the potential difference has its maximum value, the open circuit voltage V_{oc} . This is equivalent to the condition when the dark current and short circuit current exactly cancel out, as expressed in the next equation:

$$V_{oc} = \frac{qV}{K_B T} - \ln \left(\frac{J_{sc}}{J_0} + 1 \right)$$

This equation shows that V_{oc} increases logarithmically with light intensity, this is important due to efficiency depend linearity of V_{oc} .

Fill Factor (FF): It is the rate between the electrons photogenerated in the conduction band and the electrons injected into the TiO_2 . To estimate the fill factor it is necessary to calculate the maximum electrical power obtained in the cell (P_m), this provides a specific photocurrent (J_m) and voltage (V_m). These three parameters define an specific area A_1 (see Figure 2.4). J_{sc} and V_{oc} define other area A_2 . The FF is defined as the ratio between A_1 and A_2 , this is [110]:

$$FF = \frac{A_1}{A_2}$$

$$FF = \frac{J_m V_m}{J_{sc} V_{oc}}$$

Photoconversion efficiency (PCE or η): The efficiency of a solar cell is given by the equation:

$$PCE = \frac{P_{max}}{P_{in}}$$

$$PCE = \frac{J_m V_m}{P_{in}}$$

Where P_{max} is the maximum obtainable electrical power of the cell, P_{in} is the incident illumination intensity, J_m is the current density obtained at maximum power, and V_m is the voltage obtained at maximum power.

It is possible to describe the PCE in terms of J_{sc} , V_{oc} and FF using the equation:

$$PCE = \frac{J_{sc} V_{oc} FF}{P_{in}}$$

$$PCE(\%) = \frac{J_{sc} V_{oc} FF}{P_{in}} \cdot 100$$

2.5.3.2 Incident Photon to Current Efficiency (IPCE)

It is defined as the ratio of the number of electrons that are photogenerated for each incident photon at a given wavelength (λ), and can be determined from the J_{sc} using the expression [111]:

$$IPCE(\%) = 1240 \cdot \frac{J_{sc} (Acm^{-2})}{\lambda(nm) \times I_{inc} (Wcm^{-2})} \cdot 100$$

where I_{inc} stands for the incident light intensity.

The relation between the IPCE spectrum and the J_{sc} can be expressed using the next equation [25, 112]:

$$J_{sc} = q \int b_s(\lambda) IPCE(\lambda) d\lambda$$

The IPCE spectrum can help to determine which material contributes to the photogeneration at each λ and how efficient it is. With this characterization it is possible to select one or another material to complement the photogeneration or use a specific region of the solar spectrum and increase the photocurrent.

The current density curves were measured with a Gamry potentiostat (reference 600) scanning from 0 to 600 mV at 100 mV s⁻¹. The samples were illuminated with an Oriel Sol 3A solar simulator while measuring current. The light intensity was adjusted by employing an NREL calibrated Si solar cell having a KG-2 filter for one sun light intensity (100 mW cm⁻²). The Incident Photon to Current Efficiency (IPCE) spectra was measured with a monochromator (Newport model 74125).

2.5.4 Electrochemical Impedance Spectroscopy (EIS)

Electrochemical impedance spectroscopy is an excellent technique for characterizing electrochemical systems [113-115]. EIS can help to identify different physical process within the cell, such as: a) electron transport in the TiO_2 , influence by the free carrier density, and electron mobility [114, 116-118]; b) recombination process between electrons in the TiO_2 and the redox species in the electrolyte [89, 119]; c) charging of capacitive elements in the system, including the Helmholtz capacitance in the TiO_2 /electrolyte interface and the capacitance related to filling the conduction band and surface states of the TiO_2 [113, 120]. Also, the lifetime, the diffusion coefficient and the diffusion length might be obtained [115].

Electrochemical Impedance is obtained by applying a potential perturbation to an electrochemical system at equilibrium and measuring the resulting current. The perturbation signal usually has a sinusoidal waveform, and then the current response is a sinusoid with the same frequency as the potential perturbation but shifted in phase.

The sinusoidally modulated potential signal can be expressed as a function of time:

$$\Delta E(t) = E_0 \sin(\omega t)$$

where $\Delta E(t)$ is the potential perturbation at a time t , E_0 is the signal amplitude, and ω is the radial frequency, which is related to the frequency by $\omega = 2\pi f$. The current response to that perturbation has the form:

$$\Delta I(t) = I_0 \sin(\omega t + \phi)$$

$\Delta I(t)$ is the current at a time t , I_0 the current amplitude, and ϕ the phase shift.

The impedance is defined as the ratio:

$$Z(t) = \frac{\Delta E}{\Delta I} = \frac{E_0 \sin(\omega t)}{I_0 \sin(\omega t + \phi)} = Z_0 \frac{\sin(\omega t)}{\sin(\omega t + \phi)}$$

$$Z(t) = Z_0 (\cos \phi + i \sin \phi)$$

$$Z(t) = Z' + iZ''$$

where $i = \sqrt{-1}$, and Z' and Z'' are the real and imaginary parts of the impedance, respectively.

It is common to use the so called Nyquist plot to display the impedance data. In Nyquist plots the real part of the impedance is plotted in the X-axis and the corresponding imaginary part on the Y-axis. Low frequency data are represented on the right side of the plot and high frequency data on the left see Figure 2-5.

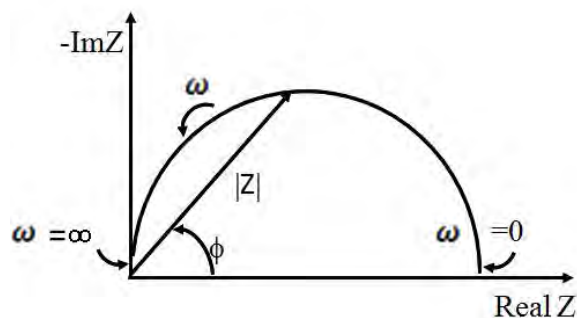


Figure 2-5 Nyquist plot.

From this plot, it is necessary to extract the information about the electrochemical processes; one strategy involves the fitting of the impedance data to an equivalent circuit model. These models consist of a network of electrical circuit elements (resistors, capacitors, etc). These elements are assigned by the electrophysicochemical processes in the system.

In our work, the EIS data were fit using the transmission line model shown in Figure 2-6 [121-124]. In this model, R_s is the series resistance that is related to the electron flux resistance in the FTO and the wires, R_t is the transport resistance arising from the opposition to the electron flux, Z_d is the Warburg element and represents Nernst diffusion in the electrolyte, R_c and C_c are the charge-transfer resistance and double-layer capacitance at the counter electrode, finally R_{rec} and C_μ are the recombination resistance and the chemical capacitance that come from the resistance against recombination of electrons from the TiO_2 CB with states in the electrolyte or the sensitizers and from the variation of the electron chemical potential, respectively.

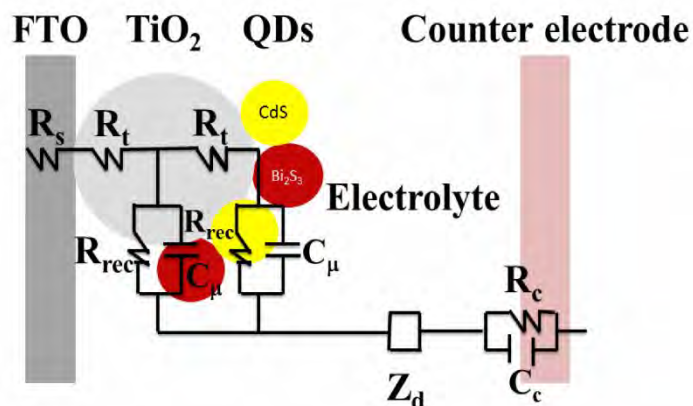


Figure 2.6 Transmission line for the diffusion–recombination model used to fit the impedance measurements. R_{rec} is the charge-transfer resistance of the charge recombination process between electrons in the TiO_2 film and the electrolyte; C_μ is the chemical capacitance of the TiO_2 film; R_t is the transport resistance of the electrons in the TiO_2 film; Z_d is the Warburg element showing the Nernst diffusion of the electrolyte; R_c and C_c are the charge-transfer resistance and double-layer capacitance at the counter electrode.

Electrochemical Impedance Spectroscopy (EIS) measurements were carried out by applying a small voltage perturbation (10 mV rms) at frequencies from 100 kHz to 0.1 Hz for different forward bias voltages in dark conditions. Experimental results were fitted with the ZView software.

Chapter 3

Quantum Dots Sensitized Solar Cells with Absorption in the Visible Region

3.1 Introduction

In order to obtain higher efficiencies CdS and CdSe QDs have been widely studied [38, 93, 125-130], due to their high quantum efficiency in the visible region (up to 60 % at 450 nm and up to 80% at 600 nm, respectively), obtaining photoconversion efficiencies up to 2.3% and 5.4 % respectively [125, 131-133].

The mixing of different kinds of QDs as sensitizers has been reported as a promising procedure to obtain higher efficiencies by expanding the absorption wavelength region for light harvesting [64, 134-136], increase electron injection, and also enhance the charge transport [137]. In particular, CdS and CdSe have been combined by different methods in various architectures, like ternary compounds as CdSeS ($\eta=4.05\%$) [138, 139], CdS/CdSe deposited by chemical bath deposition ($\eta=3.5\%$) [140] and by SILAR ($\eta=5.21\%$) [56]. Another method used for TiO_2 sensitization is electrophoretic deposition reaching an $\eta=1.7\%$ for CdSe QDs [141] and 3.2% for CdSeS QDs [139]. One key factor in many deposition methods is the addition of inorganic ligands to enhance electronic transport and successfully passivate surface defects in colloidal QD, playing an important role mediating electron transfer reactions in the surface chemistry of colloidal QDs [142, 143].

Conventional QDSSCs are based on photoanodes composed for semiconductors QDs sensitized to the visible absorption. In this chapter is analyzing two QDs with absorption in the visible light: CdS and CdSe, with a different combination of deposition technique.

3.2 Solar cell photoanode fabrication

TiO₂/CdS/ZnS (reference sample): CdS and ZnS were prepared by SILAR method. CdS QDs were added as was explained above. (Section 2.3.1). The optimization of this

process reveals that seven SILAR cycles were done to obtain a uniform coverage of the TiO₂ nanoparticles (NPs) with CdS QDs. To enhance the photovoltaic performance ZnS is deposited by SILAR in order to passivate CdS surface and reduce the recombination of electrons in the TiO₂ to the polysulfide electrolyte [123, 144-147]. ZnS passivation was obtained by using 0.1 M of Zn(CH₃COO)₂·2H₂O and 0.1 M of Na₂S both dissolved in water as Zn²⁺ and S²⁻ sources respectively. The films were dipped for 1 min/dip in the solutions during 2 SILAR cycles.

TiO₂/CdS/CdSe/ZnS: this sample was fabricated as follows: After the CdS QDs sensitization, CdSe QRs were deposited by electrophoresis (see section 2.3.2). Next, a CdSe-MPA film was added by pipetting method (Figure 2-c). This process was repeated 10 times. Then, ZnS QDs were added as was explained above. In this chapter is used different deposition technique and is used S for SILAR, E for Electrophoretic and P for Pipetting.

3.3 Morphological Characterization

Figure 3-1a shows a typical TEM image of CdS QDs sensitized TiO₂ nanoparticles prepared by SILAR method. The average size of CdS QDs is 3 nm, presenting a high coverage of QDs onto TiO₂ NP surface. Figure 3-1b shows the TEM image of colloidal CdSe QRs showing average dimensions of 10 nm long and 5 nm wide. Therefore, the CdS nanoparticles and CdSe nanorods are in the regime of quantum confinement [148].

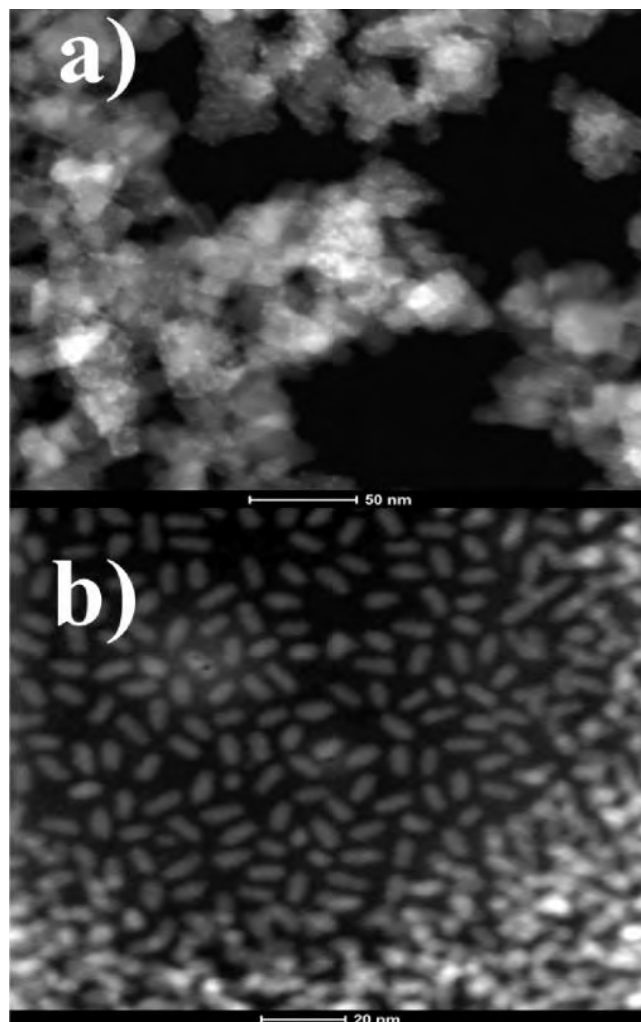


Figure 3-1. Transmission electron microscopy images of a) $\text{TiO}_2/\text{CdS(S)}$ where CdS(S) QDs were deposited by SILAR method showing an average size of 3 nm and b) colloidal CdSe QRs showing an average size of 10 nm long and 5 nm wide.

SEM images of TiO_2 , $\text{TiO}_2/\text{CdS(S)}/\text{ZnS(S)}$, $\text{TiO}_2/\text{CdSe}/\text{ZnS}$ and $\text{TiO}_2/\text{CdSe}/\text{ZnS}$ are shown in Figure 3-2. The TiO_2 transparent layer deposited by Doctor Blade method without sensitizers forms a homogenous highly porous film with nanoparticle average size of 20 nm, (see Figure 3-2a). The TiO_2 nanocrystals are uniformly covered by QDs and QRs, and filling partially the pores as is shown in Figure 3-2b and c. Figure 3-2d shows the TiO_2 films sensitized with CdSe by pipetting method and the pore filling is more clearly observed.

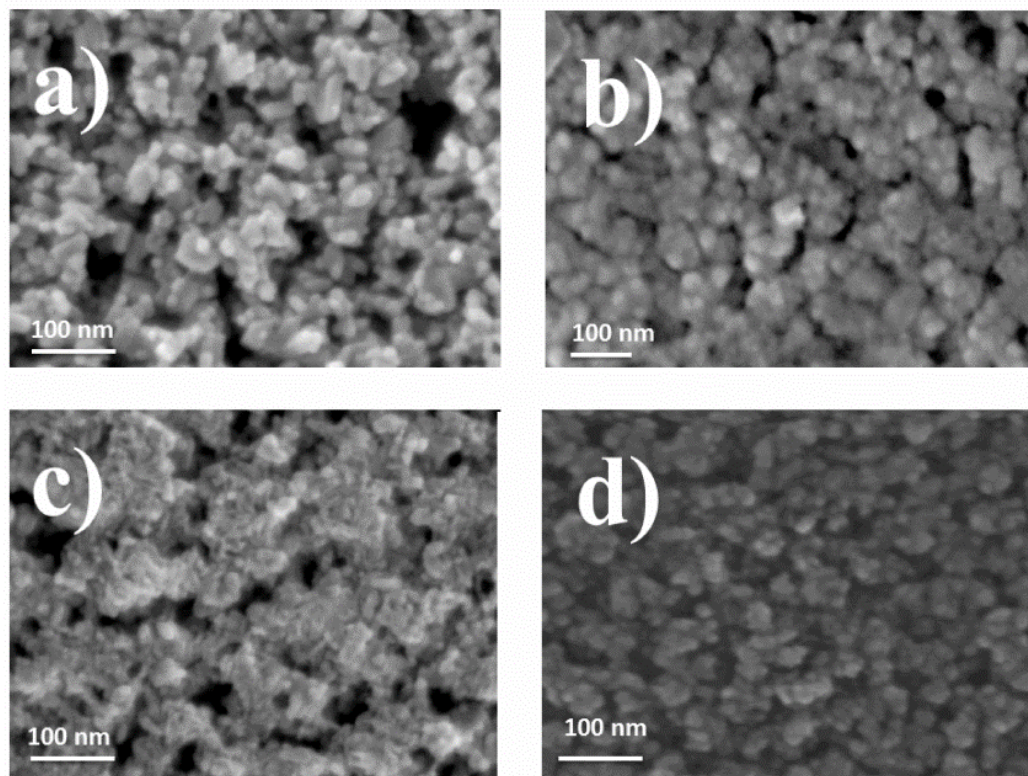


Figure 3-2. Scanning electron microscopy images of different configurations a) TiO_2 transparent layer, b) $\text{TiO}_2/\text{CdS}(\text{S})/\text{ZnS}(\text{S})$, where $\text{CdS}(\text{S})$, c) $\text{TiO}_2/\text{CdSe}(\text{E})/\text{ZnS}(\text{S})$ and d) $\text{TiO}_2/\text{CdSe}(\text{P})/\text{ZnS}$ where $\text{CdSe}(\text{P})$. In all cases $\text{ZnS}(\text{S})$ was.

The cross-section SEM images and EDS analyses of CdSe sensitized TiO_2 device are displayed in figure 3-3. In Figure 3-3a all layers composing the device are observed. From right to left, the first film observed is the FTO followed by the TiO_2 compact layer (190 nm), the transparent layer (9 μm) composed of 20 nm TiO_2 nanoparticles, and finally the opaque layer (8 μm) composed of 200 nm TiO_2 nanoparticles. The Cd and Se atoms distributions detected by EDS mappings are shown in Figure 3-3b and 3-3c, respectively. EDS characterization highlights the uniform distribution of CdSe QRs inside of the mesoporous TiO_2 films increasing the concentration in the transparent layer, which is consistent with the higher superficial area of the nanoparticles in this layer. Distribution plots of Cd^{2+} atoms along different TiO_2 films sensitized by pipetting and electrophoresis methods are presented in Figure 3-3d. Notice that pipetting produces a concentration profile that decreases along the transparent TiO_2 layer, obtaining lower concentration close to the FTO substrate. However, the electrophoretic method produces an inverse profile with high

QRs concentration close to the substrate. This is expected because pipetting depends on the natural diffusion of QRs while in the electrophoretic process sensitizers are attracted to the FTO electrode. Therefore, the highest concentration is obtained when combining both pipetting and electrophoretic methods producing an adequate gradient of QDs along TiO₂ are being higher close to FTO.

The effective coverage of the TiO₂ with CdSe QDs by different sensitization techniques is obtained [127]. The amount of the atomic percentage of cadmium is calculated with the EDS mapping. If we consider CdSe QRs as a capsule geometrically figure and monodispersed particle with a length of 10 nm and width of 5 nm, then the total surface area covered by the QRs particle would be of 39 cm², 49 cm² and 53 cm² for P, E and EP, respectively. The TiO₂ particle electrode was considered as a spherical particle of 20 nm of diameter obtaining a surface area of 180 cm². Finally, by dividing the surface areas (CdSe QRs/ TiO₂), we find an approximate value coverage TiO₂ equal to 22% for electrophoretic, 24% for pipetting due to the major diffusion of the QDs and 30% for the combination technique due to the increased amount of material. In conclusion, the density of CdSe QRs depends on the sensitization technique; the combination of techniques increases the coverage of CdSe on TiO₂. This is only one approximately due to is not consider agglomeration of QDs or different monolayer, for this considerations is only the approximation.

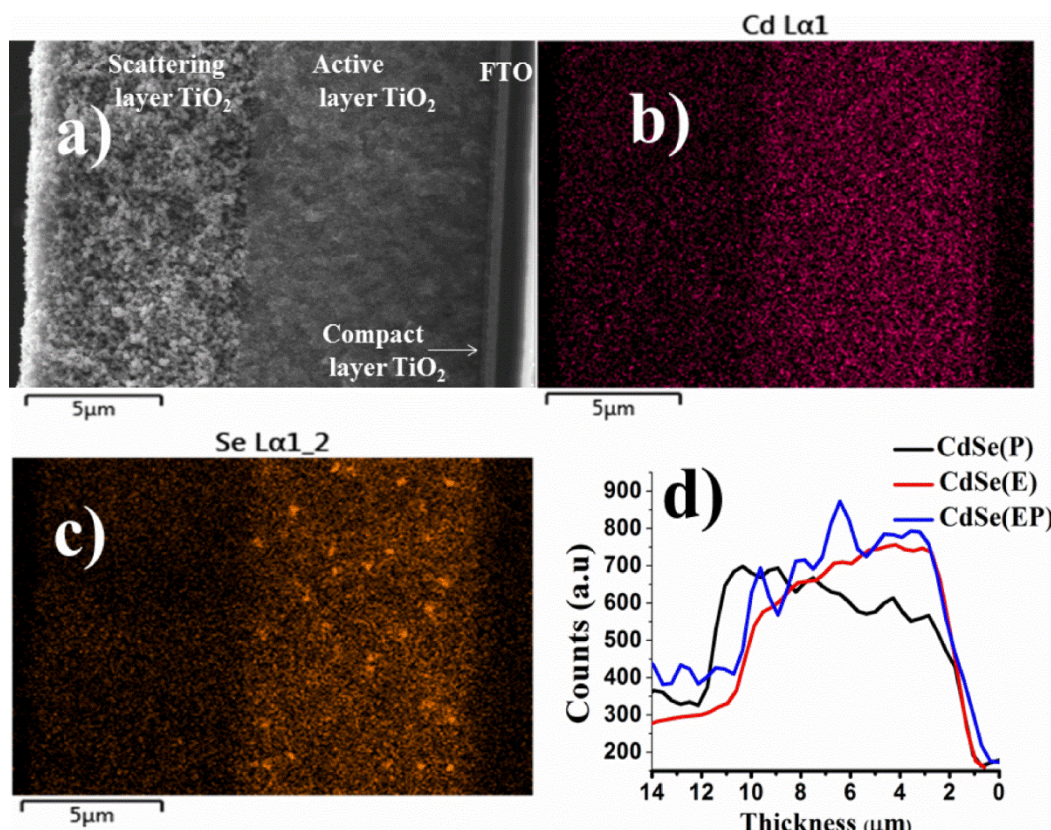


Figure 3-3. a) Cross-section SEM images of TiO₂/CdSe QRs films sensitized by electrophoretic and pipetting methods with TiO₂ compact layer (190 nm), active layer (9 μm) and scattering layer (8 μm); b) and c) EDS mapping of Cd²⁺ atoms and Se atoms, respectively by electrophoretic and pipetting method, d) Cd²⁺ distribution through TiO₂ films as a function of deposition depth for different methods.

3.4 Optical characterization

The UV-Vis absorption and photoluminescence (PL) spectra of colloidal CdSe QRs in solution are shown in Figure 3-4a. It is observed well defined absorption bands located at 590 nm and a weaker band centered at 480 nm. The former band originates from the ground-state transition when a 1s electron-heavy hole pair is generated. The higher energy band is probably a combination of two transitions: one is again a 1s transition that involves the hole from the spin-orbit split-off valence band, and the other is the first excited-state transition [148]. The PL spectrum shows one peak at 620 nm when excited at 390 nm. This peak corresponds to the transition from conduction to valence band of QRs. Consequently, the derivate of the absorption spectrum (Figure 3-4b) has two local maximums one at 2.05

eV corresponding to the band gap, and another one at 2.4 eV for the transition from the valence band to the first excited state.

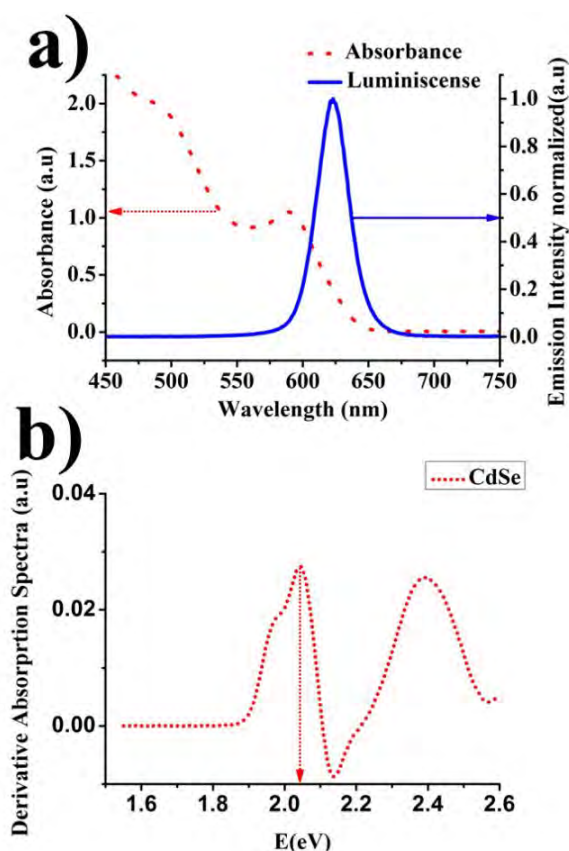


Figure 3-4. a) Absorption and emission spectra of CdSe colloidal QRs, the emission was obtained after excitation at 396 nm. b) Derivative absorption spectrum of CdSe colloidal QRs showing the band gap at 2.05 eV.

The absorption spectra of different configurations of sensitized TiO_2 are shown in Figure 3-5. The shoulder in the absorption spectra centered at 450 nm is associated to CdS [88]. The introduction of CdSe QRs produces an additional absorption band in the red region centered at 625 nm. The red shift of the absorption peak, compared to colloidal QRs (see figure ??), is probably a result of the agglomeration produced during the film preparation. Interestingly, such red band is stronger when deposited by pipetting than deposited by electrophoresis. An increment in the overall absorption band was observed when QRs were introduced by both, E and P, techniques. This increment in the absorption coefficient confirms the concentration increase of sensitizer QRs and is expected to

improve the photovoltaic conversion efficiency of all devices with this configuration. The ZnS band gap is about 3.6 eV which corresponds to an absorption band at 320 nm[146] and does not influence significantly the absorption in the visible range.

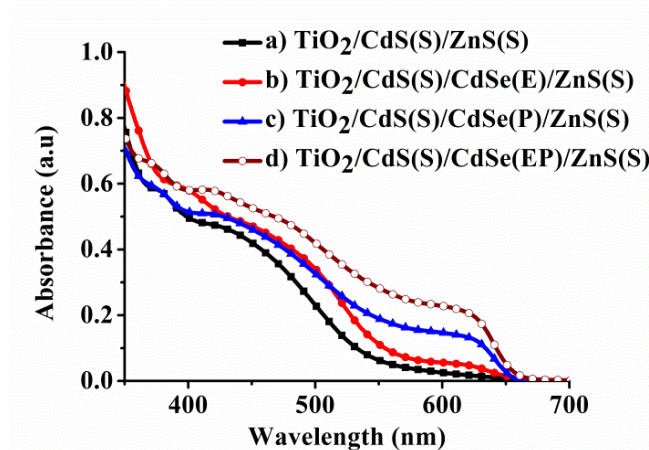


Figure 3-5. Absorption spectra of CdS QDs and CdSe QRs sensitized TiO₂ layers by different techniques, TiO₂/CdS(S)/ZnS(S), TiO₂/CdS(S)/CdSe(E)/ZnS(S), TiO₂/CdS(S)/CdSe(P)/ZnS(S) and TiO₂/CdS(S)/CdSe(EP)/ZnS(S), where S stand for SILAR, E for Electrophoretic, and P for pipetting.

3.5 Electrochemical characterization

3.5.1 CdS and CdSe quantum dots sensitized solar cells

The current density-voltage (J-V) profiles for TiO₂ films sensitized with CdS QDs and CdSe QRs in the different configurations, TiO₂/CdS(S)/ZnS(S), TiO₂/CdSe(E)/ZnS(S) and TiO₂/CdSe(P)/ZnS(S) are displayed in Figure 3-6a. The measured short-circuit current density and open-circuit voltage are summarized in Table 3-1. The fill factor and photoconversion efficiency were calculated using equations 3-1 and 3-2 [24].

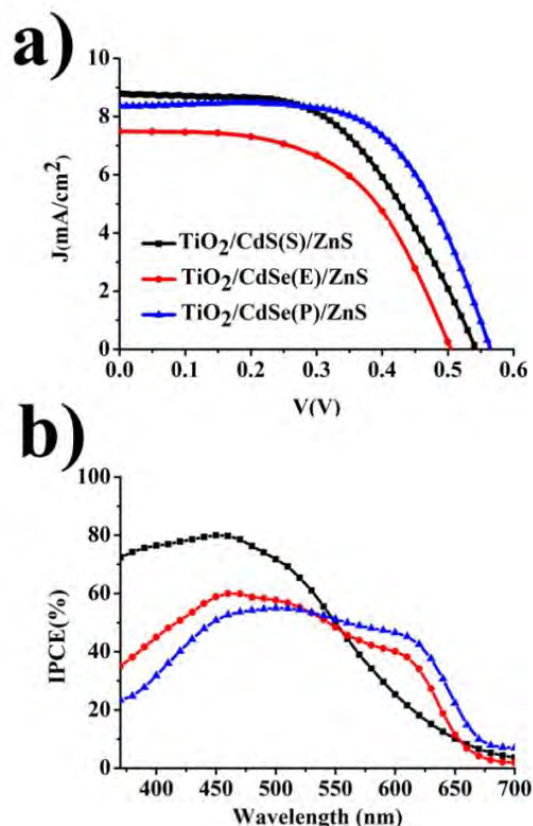


Figure 3-6. J-V (a) and IPCE (b) curves for $\text{TiO}_2/\text{CdS}(\text{S})/\text{ZnS}(\text{S})$, $\text{TiO}_2/\text{CdSe}(\text{E})/\text{ZnS}(\text{S})$, $\text{TiO}_2/\text{CdSe}(\text{P})/\text{ZnS}(\text{S})$ devices.

The $\text{TiO}_2/\text{CdSe}(\text{E})/\text{ZnS}$ configuration presents a $J_{\text{sc}} = 7.4 \text{ mA}/\text{cm}^2$ and a $V_{\text{oc}} = 504 \text{ mV}$ resulting on a photoconversion efficiency of $\eta = 2.1\%$. Meanwhile, when CdSe QRs are deposited by pipetting ($\text{TiO}_2/\text{CdSe}(\text{P})/\text{ZnS}$) a $J_{\text{sc}} = 8.4 \text{ mA}$ and $V_{\text{oc}} = 564 \text{ mV}$ were obtained, this results on a higher efficiency of $\eta = 2.9\%$. This difference is consistent with the higher concentration of CdSe QRs by pipetting than that obtained by electrophoretic deposition as was observed from EDS in figure 3-3 and corroborated in the absorption spectra from figure 3-5. Interestingly, notice the strong increment of the FF from 55% for sample sensitized by electrophoresis to 63% for those sensitized by pipetting. This fact indicates that when the QRs are deposited by pipetting the charge carrier transport is improved and/or the recombination processes are reduced [149, 150]. This is probably the result of QRs gradient where larger concentration on the top of compact TiO_2 film provides a better interaction with electrolyte, thus reducing the recombination. Furthermore, the FF is higher than the 53% presented for sample sensitized with CdS(S) which presents a

photoconversion efficiency of 2.5%. This result suggests that QDs directly grown on the surface of TiO₂ by SILAR method introduce more defects [130], and then more recombination, than colloidal nanoparticles.

SAMPLE	J _{sc} (mA/cm ²)	V _{oc} (mV)	FF(%)	η (%)
TiO ₂ /CdS(S)/ZnS(S)	8.7	542	53.5	2.5
TiO ₂ /CdSe(E)/ZnS(S)	7.4	504	55.2	2.1
TiO ₂ /CdSe(P)/ZnS(S)	8.4	564	63.1	2.9

Table 3-1. Photovoltaic parameters J_{sc}, V_{oc}, FF, and η extracted from J-V curves of the QDs sensitized TiO₂ solar cells prepared with different technique depositions, SILAR (S), Electrophoresis (E) and Pipetting (P).

The incident photon to current conversion efficiency curve of the TiO₂/CdS/ZnS, TiO₂/CdSe(E)/ZnS and TiO₂/CdSe(P)/ZnS are presented in Figure 3-6b. There, it is observed that the origin of the photocurrent is different according to the composition of the sensitizer. TiO₂/CdS(S) photoelectrodes have higher quantum efficiency (QE=80% at 450 nm) but in a narrow spectral range that decays rapidly for $\lambda > 550$ nm due to the larger bandgap (E_g) of CdS in comparison to CdSe. Devices sensitized with CdSe QRs, either by electrophoresis or pipetting methods, have lower QE (60% at 450 nm) but relatively constant up to 630 nm (IPCE=40%) which correspond to the absorption of CdSe QRs, see figure 3-6b. This extra 80 nm of photogeneration region provides enough electrons to obtain almost the same photocurrent than that provided by CdS QDs despite the lower quantum efficiency. Therefore, CdS QDs present high photogeneration in a limited region of the solar spectrum; while, CdSe QRs photogenerate in a wider region of the solar spectrum but with a lower QE due to the limited QR loading. Then, CdS QD and CdSe QR can be successively deposited to expand the region of the photogeneration maintaining high QE that would result on an increase in the J_{sc} maintaining relatively high V_{oc}, FF and photoconversion efficiency.

3.5.2 Combination of CdS/CdSe quantum dots sensitized solar cells

The combination of CdS QD prepared by SILAR with colloidal CdSe QR to sensitize TiO₂ improves the photoconversion efficiency of solar cell devices. Figure 3-7a shows the J-V

curve for devices sensitized in four configurations, $\text{TiO}_2/\text{CdS}(\text{S})/\text{ZnS}$, $\text{TiO}_2/\text{CdS}(\text{S})/\text{CdSe}(\text{E})/\text{ZnS}$, $\text{TiO}_2/\text{CdS}(\text{S})/\text{CdSe}(\text{P})/\text{ZnS}$ and $\text{TiO}_2/\text{CdS}(\text{S})/\text{CdSe}(\text{EP})/\text{ZnS}$, and Table 3-2 shows the J_{sc} , V_{oc} , FF and η of such samples calculated from the J-V curves. The addition of CdSe QRs increases the J_{sc} from 38%, for pipetting, to 54% for electrophoresis co-sensitized compared to CdS QDs single sensitized TiO_2 device. These results show an increment of 50% for the combination of both techniques suggesting that an excess of QRs could produce a shielding effect where not all the sensitizer harvests the impinging light. Such increase in the photocurrent is the result of the absorption bandwidth enlargement (~ 100 nm compared to CdS) as is confirmed from the IPCE displayed in figure 6b. CdSe QRs also increases the V_{oc} with an overall increment of 6% when sensitizer is introduced by both techniques (EP), although pipetting method produces a strong increase larger than 15.6% (from 542 mV to 626 mV). This variation suggests an upward shifting of the Fermi level as a result of the interaction between CdS QDs and CdSe QRs and it depends on the deposition method. Interestingly, the FF decays strongly from 53.5% for $\text{TiO}_2/\text{CdS}(\text{S})$ to 49% for $\text{TiO}_2/\text{CdS}(\text{S})/\text{CdSe}(\text{E})$ that represent a loss of 9%. However, it presents a dramatic increase of $\sim 14\%$ when CdSe QRs are introduced by combining both electrophoresis (E) and pipetting (P) method. A reduction or enhancement on the FF is associated to an increase or a decrease of the recombination charge, respectively. Therefore, these experimental results suggest that a homogenous distribution of CdSe QRs along the TiO_2/CdS , as the one obtained when combined electrophoresis and pipetting method (see figure 5-3d), promotes a major mobility and then reduces the recombination charge. This confirms that neither electrophoresis nor pipetting methods alone, but both methods combined, produces the major enhancement on the performance of the solar cell device. In fact, the photoconversion efficiency for CdS/CdSe is higher than CdS alone in all cases. But, when combining electrophoresis and pipetting the photoconversion efficiency was 4.6% that represents an increment of 84% compared to CdS QD single sensitized.

SAMPLE	$J_{\text{sc}}(\text{mA}/\text{cm}^2)$	$V_{\text{oc}}(\text{mV})$	FF(%)	$\eta(\%)$
$\text{TiO}_2/\text{CdS}(\text{S})/\text{ZnS}(\text{S})$	8.7	542	53.5	2.5
$\text{TiO}_2/\text{CdS}(\text{S})/\text{CdSe}(\text{E})/\text{ZnS}(\text{S})$	13.4	589	49	3.9

TiO ₂ /CdS(S)/CdSe(P)/ZnS(S)	12.0	627	53.4	4.0
TiO ₂ /CdS(S)/CdSe(EP)/ZnS(S)	13.1	575	60.9	4.7

Table 3-2. Photovoltaic parameters J_{sc} , V_{oc} , FF, and η extracted from J-V curves of the QDs and QRs sensitized TiO₂ solar cells with different configuration and combined techniques (SILAR, Electrophoresis and Pipetting).

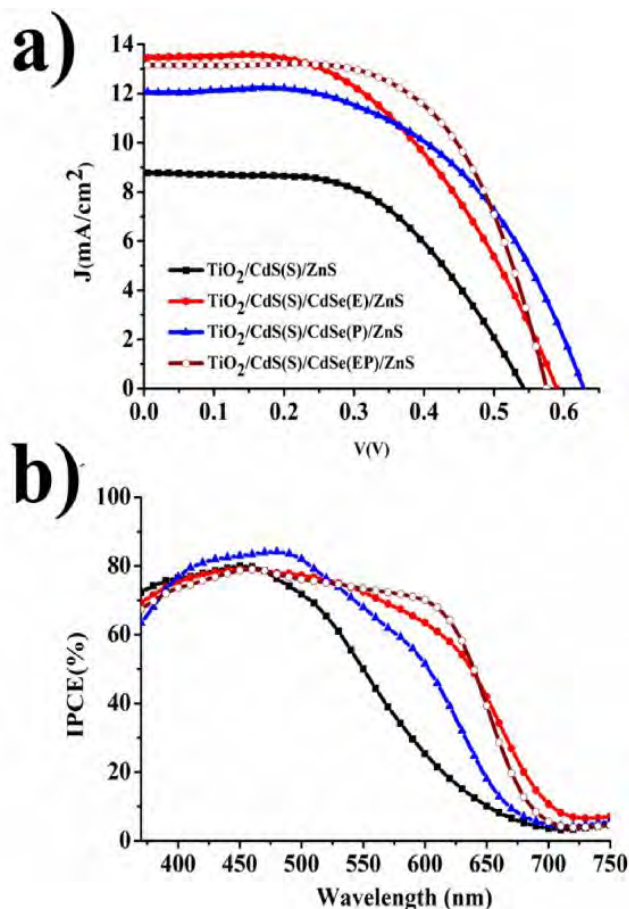


Figure 3-7. J–V (a) and IPCE curves (b) of TiO₂/CdS(S)/ZnS(S), TiO₂/CdS(S)/CdSe(E)/ZnS(S), TiO₂/CdS(S)/CdSe(P)/ZnS(S) and TiO₂/CdS(S)/CdSe(EP)/ZnS(S) devices. The working electrode areas were 0.125 cm². A Cu₂S counter electrode was used, and aqueous 1 M Na₂S, 1M S and 0.1M NaOH served as the electrolyte. The performance of the solar cells was measured under AM 1.5 radiation with an incident power of 100 mW/cm².

A detailed analysis of the IPCE spectra displayed in Figure 3-7b shows that the addition of CdSe QRs effectively increases the light harvesting region with no reduction of the external quantum efficiency (EQE) corresponding to the CdS light absorption band. Both CdS and CdS/CdSe-sensitized TiO₂ solar cells exhibit strong photoconversion response over the visible range with EQE greater than 75%. However, the CdS sensitized electrode decays faster below 70% after 510 nm to be completely extinguished at 700 nm.

This behavior was observed by other groups [151, 152]; they showed that employing a Cu_2S counter electrode leads to a red shift from 600 nm to 700 nm for the CdS sensitized TiO_2 . They hypothesized that the Cu_2S counter electrode also absorbs some light and contributes to the cell current; however, further study is required to understand this phenomenon. For CdS/CdSe co-sensitized electrodes such decay start after 550 nm for QRs deposited by pipetting and after 575 nm for those deposited by electrophoresis. Indeed, for CdSe introduced by both electrophoresis and pipetting decay start after 610 nm. This means that the combination of CdS with CdSe introduced by electrophoresis and pipetting extend the light harvest region more than 230 nm, from 380 to 610 nm with an EQE of 70% being completely extinguished at 700 nm. Such synergistic effect is clearly observed by comparing the IPCE between single CdSe QRs (see figure 3-7b) with CdS/CdSe cosensitized TiO_2 . This is the reason for the J_{sc} and FF enhancements and explains the strong increment of photoconversion efficiency. The near infrared absorbance of CdSe QRs nanocrystals is due to the particle size, increasing the photoabsorption range obtaining a maximum photoconversion efficiency of 4.7 %.

. To understand the dynamics of electrons, the band-edge levels of TiO_2 , CdS, CdSe and CdS/CdSe electrodes were determined from Mott-Schottky plots [153] and the band gap was obtained from the absorption spectra; the final energy diagram is shown in Figure 3-8. The calculated TiO_2 conduction band (CB) is -4.03 eV, and when the sensitization is done with CdS QDs and CdSe QRs, the CB increases to -3.83 eV and -3.22 eV, respectively. This results on an increment of the electron injection efficiency through the cascade mechanism as described in figure 3-8. Finally, it is observed that the CdS/CdSe CB is -3.49 eV due to the Fermi-level alignment [137] showing the CB above the TiO_2 CB obtaining a favorable electron injection and an increase in V_{oc} from 542 mV to 575 mV.

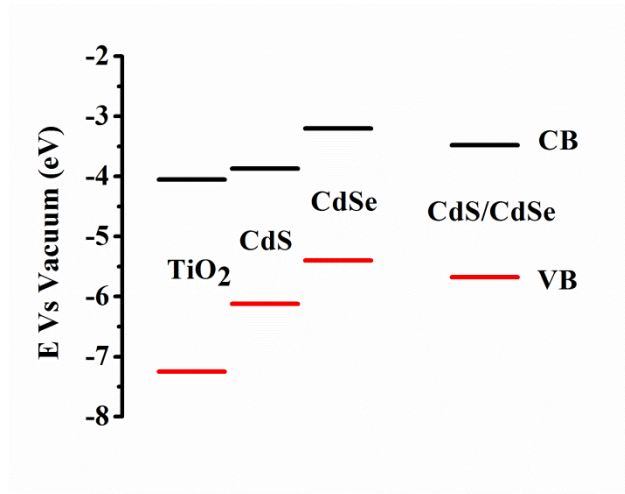


Figure 3-8. Energy diagrams level for TiO₂, CdS, CdSe and CdS/CdSe QDs and QRs. The CB position was determined from Mott-Schottky plots.

A multilayered semiconductor sensitizer structure composed of three differently sized CdSe quantum rods was studied. Based on detailed structural, optical, and photoelectrical studies, the increased photocurrent is attributed to broadened light absorption while the increased voltage is due to a shift in the relevant energy levels [37].

3.5.3 Effect of ZnS in quantum dots sensitized solar cells

The current density-voltage (JV) curves for CdS/ZnS and CdS/CdSe/ZnS with different cycles of ZnS are displayed in the Figure 3-9. From these results, J_{sc} , V_{oc} , FF and PCE were calculated (Table 3-3). For the case of CdS/ZnS, the J_{sc} is not affected by the number of the ZnS cycles obtaining similar results of 8.8 and 8.9 mA/cm² for 2 and 4 cycles, respectively. The IPCE showed similar curves (inset Figure 3-9). The V_{oc} and FF increase with more cycles of ZnS QDs form 0.542V to 0.579V and 52.4% to 62.1% for 2 and 4 SILAR cycles, respectively. The PCE increases from 2.5% to 3.2% for 2 and 4 ZnS SILAR cycles in the configuration. The behavior is similar when the sensitized is CdS and CdSe, the V_{oc} and FF increases from 0.587 V to 0.636 V and 49.2% to 54.2%, respectively. The PCE increases from 3.9% to 4.9% for 2 and 4 ZnS SILAR cycles respectively. The total enhancement due to the effect of ZnS SILAR cycles is 25%. The results suggest that the ZnS acts as a surface passivator, incrementing the charge transport and the photocurrent in the QDSSCs.

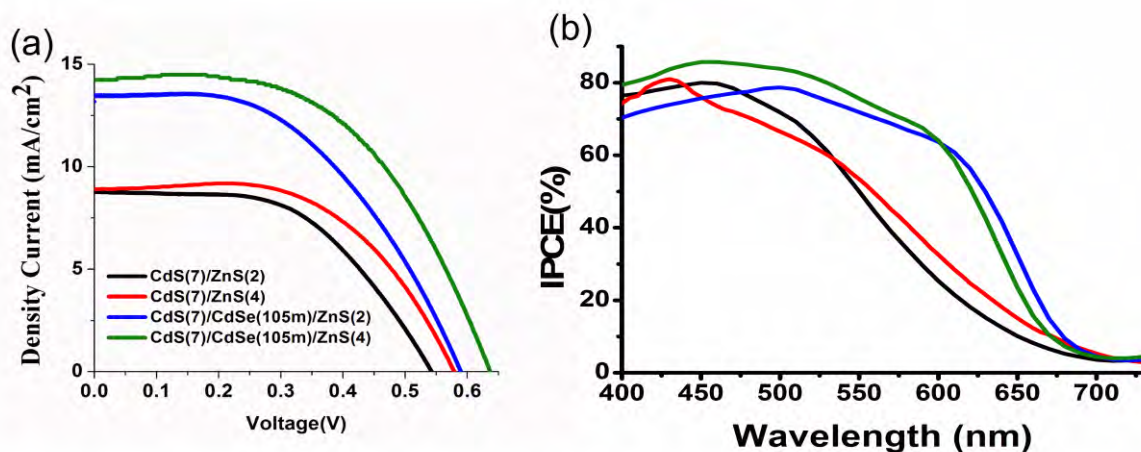


Figure 3-9. (a) JV curve for CdS/ZnS and CdS/CdSe/ZnS configurations comparing the number of ZnS SILAR cycles. (b) The IPCE curve for these configurations.

Sample	Jsc(mA/cm ²)	Voc(V)	FF(%)	η(%)
CdS(7)/ZnS(2)	8.8	0.542	52.4	2.5
CdS(7)/ZnS(4)	8.9	0.579	62.1	3.2
CdS(7)/CdSe(105m)/ZnS(2)	13.5	0.587	49.2	3.9
CdS(7)/CdSe(105m)/ZnS(4)	14.2	0.636	54.3	4.9

Table 3-3. Principal parameters in the solar cells, short current density, open circuit voltage, Fill Factor and photoconversion efficiency.

3.6 Electrochemical Impedance

Electrochemical impedance spectroscopy (EIS) measurements were carried out to explain the trends observed in the solar cell parameters when CdS QDs and CdSe QRs are combined in terms of the internal physical processes. The transmission line model shown in Figure 2.6 was used to fit the impedance measurements [88, 121]. Figure 3-10 shows the C_μ , R_{rec} and R_t extracted from the EIS measurements under dark conditions for the $TiO_2/CdS(S)/ZnS$ and $TiO_2/CdS(S)/CdSe/ZnS$ sensitized solar cells. C_μ is plotted as a function of $V_f = V_{app} - V_{series}$ which is the voltage drop at the active electrode obtained as the applied voltage, V_{app} , corrected by the voltage drop due to the series resistance (V_{series}) [88, 121]. The chemical capacitance is proportional to the density of states (DOS) in the band gap, which in turn increases exponentially with the proximity to the conduction band (CB). Therefore, an increase in C_μ reflects the upward displacement of the Fermi level (and then

the CB). As R_{rec} and R_t are exponentially dependent on the electron level density (i.e. the distance of Fermi level to the CB), a new potential is defined in order to remove the effect of the CB shift such that the measurements are at the same equivalent CB position:

$$V_{\text{ecb}} = V_F - \Delta V_i$$

where ecb means equivalent conduction band and ΔV_i is the voltage shift of the capacitance with respect to the reference sample, $\text{TiO}_2/\text{CdS}/\text{ZnS}$ films, see Figure 3-10a. After the voltage correction C_μ overlaps as is shown in Figure 3-10b. Comparing R_{rec} and C_μ for the cells, it is possible to understand the origin in the V_{oc} variation [88, 121]. Higher V_{oc} observed in the multi-sensitized cells (EP) could be due to three processes: (1) An increase in the light absorption. (2) A shift in the TiO_2 CB, and/or (3) a change in the recombination rate. An increase in the photo absorption will result in an increment in J_{sc} and would consequently produce an increase of V_{oc} . The second effect, a shift in the TiO_2 CB, produces a displacement of the TiO_2 electron quasi-Fermi level which determines the V_{oc} , then an upward shift of the TiO_2 CB would mean an increase in the V_{oc} . This upward displacement of the conduction band is identified by a shift to higher potentials of C_μ , as the 25 mV shift observed for $\text{TiO}_2/\text{CdS}(\text{S})/\text{CdSe}(\text{E})/\text{ZnS}(\text{S})$ sample in comparison with $\text{TiO}_2/\text{CdS}(\text{S})/\text{ZnS}(\text{S})$ sample in Figure 3-10a. But this is not the case of the EP samples that presents no shift respect the reference sample. The third effect, the recombination rate, can be also determined with EIS by analyzing the R_{rec} . An increase of this parameter indicates a reduction in the electron recombination processes from the TiO_2 CB to acceptor states either in the electrolyte or the sensitizers [87, 149].

Comparing $\text{TiO}_2/\text{CdS}(\text{S})/\text{CdSe}(\text{E})/\text{ZnS}(\text{S})$ and $\text{TiO}_2/\text{CdS}(\text{S})/\text{ZnS}(\text{S})$ samples in Figure 3-10c, it is observed that the multi-sensitized cell has lower R_{rec} indicating an increment in the electron recombination and then a reduction of the V_{oc} . Therefore, the V_{oc} is increased by an increment in the photogeneration and a shift in the TiO_2 CB when CdSe QRs were added by electrophoresis ($\text{TiO}_2/\text{CdS}(\text{S})/\text{CdSe}(\text{E})/\text{ZnS}(\text{S})$). And at the same time, it is reduced by an increase in the recombination processes that result in the increase of 47 mV observed in the J-V curve. In contrast, a negative shift of 50 mV was observed in C_μ and at the same time an increase in R_{rec} were obtained when the CdSe QRs was added by pipetting ($\text{TiO}_2/\text{CdS}(\text{S})/\text{CdSe}(\text{P})/\text{ZnS}(\text{S})$). This, combined with the increase of IPCE,

indicates that for such samples V_{oc} also increases by an increase in photogeneration. But contrary to the sample sensitized by electrophoresis, it is reduced by downshift of the CB and increased by a reduction in the recombination processes resulting in a higher increase of V_{oc} (85 mV).

Finally, when the CdSe QRs were deposited by both methods ($TiO_2/CdS(S)/CdSe(EP)/ZnS(S)$), C_{μ} is almost the same than for $TiO_2/CdS/ZnS$ cells indicating that the TiO_2 CB is keep in the same level. Downward and upward shifts produced in P and E samples, respectively, are compensated producing no final shift in the CB of EP sample. R_{rec} is reduced which means a downshift of the electron quasi-Fermi level by an increase in recombination processes that would result in a V_{oc} decrease. However, the photogeneration in this sample is as high as in $TiO_2/CdS(S)/CdSe(E)/ZnS(S)$ samples compensating the effect of R_{rec} an resulting in a similar increase of V_{oc} (33mV).

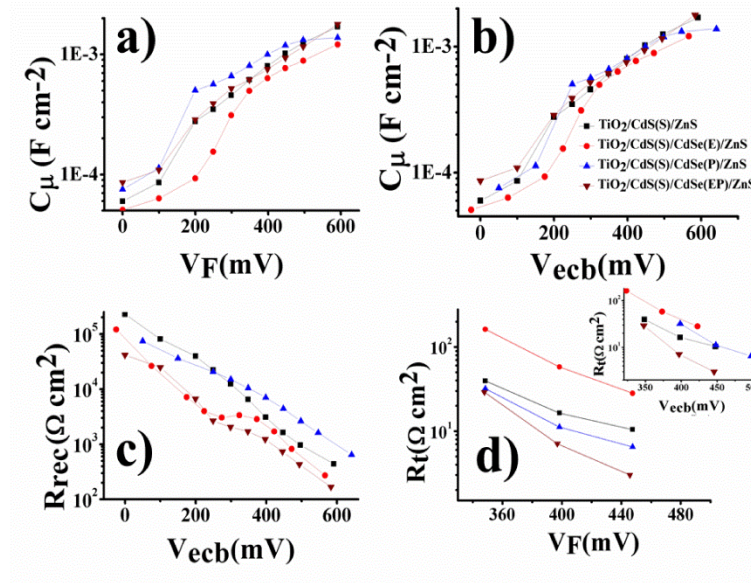


Figure 3-10. Impedance spectroscopy characterization of the $TiO_2/CdS(S)/ZnS(S)$, $TiO_2/CdS(S)/CdSe(E)/ZnS(S)$, $TiO_2/CdS(S)/CdSe(P)/ZnS(S)$ and $TiO_2/CdS(S)/CdSe(EP)/ZnS(S)$. a) and b) Chemical capacitance, C_{μ} . c) Recombination resistance R_{rec} , d) Transport resistance R_t as function of Final voltage V_f and inset R_t as a function of voltage equivalent conduction band V_{ecb} .

One important parameter to obtain the high efficiency of the $TiO_2/CdS(S)/CdSe(EP)/ZnS(S)$ samples is the FF. Variations in this parameter can be due to a change in the Transport resistance (R_t) [121, 132]. It has been previously reported that R_t can vary depending on the sensitization process. Analyzing the R_t behavior in the V_F

convention, it could be observed that the addition of CdSe QRs by electrophoresis ($\text{TiO}_2/\text{CdS}(\text{S})/\text{CdSe}(\text{E})/\text{ZnS}$) results on an increase of R_t indicating a reduction in the electron transport which results in the reduction of the FF observed in Table 3-2. When the CdSe QRs are added by pipetting the R_t decreases being a little lower and resulting in almost the same FF. Finally, when both methods are used together (EP), a reduction in R_t is observed, resulting in the meaningful increase of FF obtained for this sample. When R_t is analyzed in the ecb convention (inset of Figure 3-10 d), the behavior is preserved by all the samples except $\text{TiO}_2/\text{CdS}(\text{S})/\text{CdSe}(\text{P})/\text{ZnS}$, probably, is due to the use of inorganic ligand which in enhance electron transport and successfully passivate surface defects in colloidal QD, playing an important role mediating electron transfer reactions in the surface chemistry of colloidal QDs [142, 143]. This indicates that in this particular case the improvement in R_t is due to the CB upward shift instead to a real electron transport resistance reduction. While for the $\text{TiO}_2/\text{CdS}(\text{S})/\text{CdSe}(\text{EP})/\text{ZnS}$ there is a real improvement of the electron transport.

Chapter 4

Near infrared absorption of quantum dots sensitized solar cells

4.1 Introduction

Semiconductor QDs have been a point of attraction to increase the energy conversion efficiency of solar cells. The features that make QDs a perfect choice for incorporation into solar cells are the tunability of their band gap from the infrared to the ultraviolet region through control of size and composition, and their high molar extinction coefficients. [38, 88, 154-158]. In fact, successive deposition of CdSe QDs with various sizes has been reported as a promising procedure to obtain high efficiencies, due to the improvement of light absorption, [159, 160] which in turn, increases the photocurrent in different regions from the visible to near infrared, leading to the increase in electron injection and charge transport [75, 137, 161]. Furthermore, the photo electrochemical properties can be enhanced using different morphologies of sensitizer like quantum rods(QRs), due to the enhancement of electron injection efficiency compared with QDSSCs [162]. The use of heterostructures such as CdSe/CdTe, ZnTe/CdSe core-shell or ternary alloy QDs such as CdSeTe [81, 161, 163-165] have also increased device efficiency by extending the absorption range, providing fast charge separation and lower charge recombination.

As explained above, light absorption in the visible range has been enhanced, but there are currently efforts to increase the photocurrent produced in QDSSCs by absorption of the infrared component of the solar spectrum. To reach this goal, it is necessary to synthesize different compositions of QDs [166]. These QDs with absorbance in the range of 600-850 nm enlarge the absorption range in the QDSSCs, increasing the photocurrent.

4.2 Solar cells photoanode fabrication

TiO₂/PbS/PFN/CdS/ZnS: PbS, CdS and ZnS were prepared by the SILAR method (Figure 1a). For the deposition of PbS QDs by the SILAR method, Pb(CH₃COO)₂·2H₂O(0.02M) in methanol and Na₂S (0.02 M) in methanol:water (v:v = 1:1) were used as sources of Pb²⁺ and S²⁻, respectively. A single SILAR cycle was performed to

form the PbS layer. The PFN was dissolved in toluene (2mg/ml) and was deposited by spin coating at 2000 rpm. This layer was dried at 60°C during 5 minutes. Finally, ZnS QDs were deposited in all samples using two SILAR cycles. All samples were coated with ZnS to protect the PbS layer from the corrosive effect of the polysulfide electrolyte [123, 147].

TiO₂/CdS/Bi₂S₃/ZnS: Sensitization was performed by the SILAR method, where a single cycle consisted of dip-coating into the corresponding solutions for 1 min each, between dipping steps the electrodes were thoroughly rinsed by immersion in the corresponding solvent in order to remove any precursor excess. For the Bi₂S₃ deposition, the sample was introduced in 0.05M BiN₃O₉·5H₂O dissolved in methanol and in 0.05M Na₂S in methanol:water (V:V=1:1) as Bi²⁺ and S²⁻ sources, respectively.

TiO₂/CdS/CdSe/CdSeTe/ZnS: The TiO₂/CdS/CdSe cell was placed face to face with an FTO at a distance of 0.2 cm and immersed in a cuvette with 2.5 ml of colloidal CdSeTe QDs dispersed in toluene. CdSeTe QDs were deposited by electrophoresis with 200 DC volts applied with the TiO₂ films in the positive terminal of the power supply. After 105 min the CdSeTe QDs were uniformly distributed on the surface of the TiO₂ NPs. Finally, ZnS QDs were deposited by two SILAR cycles as explained above.

TiO₂/CdS/CdSe/CdSeTe/ZnS/SiO₂: The TiO₂/CdS/CdSe/CdSeTe/ZnS photoanodes were immersed for 15 min in a cuvette with 0.01M solution of tetraethyl ortosilicate in ethanol containing 0.1 M of NaOH, this is rinsed with water and dried with air.

4.3 Lead Sulfide quantum dots sensitized solar cells

4.3.1 Morphological characterization

The adsorption of QDs on the surface of the TiO₂ after deposition is important in order to favor electron extraction. Figure 4-1a shows a TEM image of the TiO₂ nanoparticles (second transparent layer) deposited onto FTO. The average size of the TiO₂ nanoparticles (NPs) was 20 nm (Figure 4-1b). After deposition of PbS/CdS onto the TiO₂ substrate by the SILAR technique, QDs are formed on the TiO₂, (see the tiny brilliant points on TiO₂ grains in Figure 4-1c). The measured average size of the QDs is ~ 4 nm (see Figure 4-1d). We measured the size of hundreds of nanoparticles from 50 different TEM

images to determine the size distribution for the TiO_2 and the PbS/CdS NPs. Since it is not possible to distinguish the PbS from the CdS QDs in the TEM images (figure 4-1c), and we obtained only one value for the size distribution, we concluded that both nanoparticles have similar sizes. According to the experimental procedure CdS is partially deposited on top of the TiO_2 and partially on the PbS, we expect the last option to be dominant considering the affinity between Cd and S on the surface of the PbS nanoparticles.

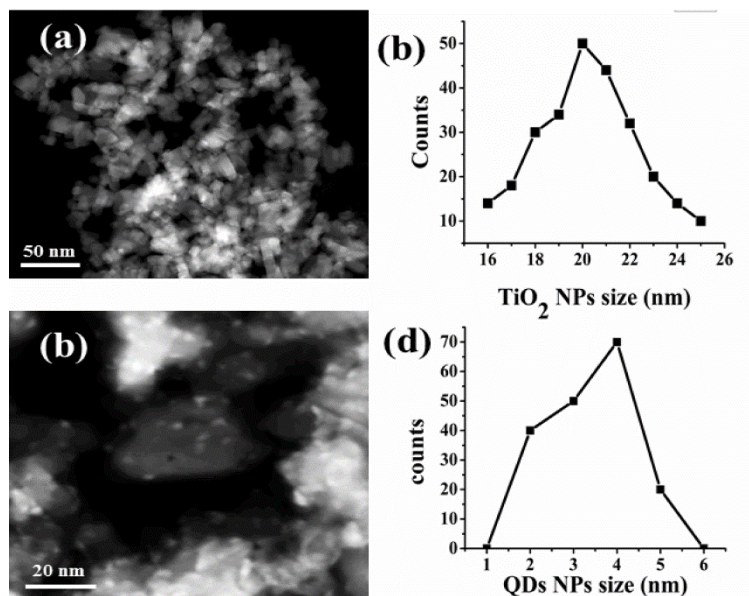


Figure 4-1. (a) TEM image of TiO_2 nanoparticles without sensitization, (b) TiO_2 nanoparticles size distribution, (c) TEM image of PbS/CdS sensitized TiO_2 nanoparticles, (d) PbS/CdS nanoparticles size distribution.

Figure 4-2a shows SEM images of the TiO_2 nanoparticles, while Figures 4-2b and 4-2c show the TiO_2 sensitized substrates at the same magnification, without and with PFN, respectively. Figure 4-2c shows an image of the substrate for the configuration $\text{TiO}_2/\text{PbS}/\text{PFN}/\text{CdS}$. It is clear that the presence of PFN changed the surface morphology of the films because a granular layer with a much smaller feature size was observed (Figure 4-2c). We believe that when PFN is deposited directly over the TiO_2 film, part of it diffuses into the film and another part is deposited on top of it. Therefore, PFN alters the TiO_2 film surface morphology as is observed by comparison of figure 4-2a (TiO_2 with no PFN) with figure 4-2c (TiO_2 with PFN). PFN can diffuse into the film because the structure displayed in figure 4-2c shows some relatively large voids; this means that PFN is able to penetrate into the pre-existing opaque TiO_2 film. A schematic representation of the

TiO₂/PbS/PFN/CdS system is presented in Figure 4-2d. Both, the PbS and the CdS QDs, cover the TiO₂ with the polymeric network trapping the nanoparticles.

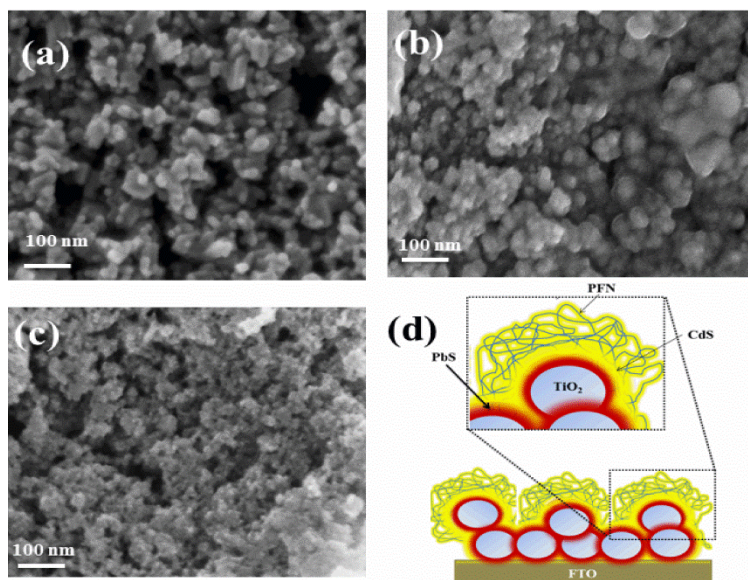


Figure 4-2. SEM images of: (a) TiO₂ nanoparticles (T0), (b) TiO₂/PbS/CdS (TPC*) and (c) TiO₂/PbS/PFN/CdS (TPPC*) (d) Schematic representation of QDs and PFN deposited on TiO₂.

4.3.2 Optical Characterization

The absorption spectra of all samples under study were obtained in order to observe the changes upon the addition of the different components in the final device. All the spectra were taken without the counter electrode, electrolyte, and ZnS protection layer. The samples have been referred as TC*, TPC*, and TPPC* to distinguish them from their counterparts in the solar cells. The spectra are shown in Figure 4-3a, the figure includes an extra sample labeled T0 consisting of only the TiO₂ layers, and the absorption spectrum of PFN. The TiO₂ film absorbs primarily in the UV region of the spectrum (sample T0). Upon addition of the CdS QDs (sample TC*) the absorption spectrum broadens towards the visible (VIS) region where a broad-band peak centered at 450 nm, characteristic of CdS [88] is observed. The contribution of PbS (sample TPC*) is characterized by a well-defined absorption band in the VIS region and a weak absorption tail into the near infrared region (NIR, up to 1000 nm) [72]. A significant absorption increase in the VIS-NIR region was observed after the incorporation of PFN (sample TPPC*). The polymer PFN absorbs only in the 300 to 420 nm range and it does not contribute, or contributes weakly, to the photo-generation of electrons [167]. Therefore, it is reasonable to interpret that the increment of

absorption in the sample containing PFN is associated to a light trapping effect produced by increased incident photon scattering within the polymeric network [168, 169]. These results were verified by diffuse reflectance measurements of the $\text{TiO}_2/\text{PbS}/\text{CdS}$ films with and without PFN, shown in Figure 4-3b. The increment in the diffuse reflectance after the incorporation of PFN, shows the effect of light scattering; similar results were obtained by submicrometer-sized mesoporous TiO_2 beads employed as scattering layer in dye sensitized solar cells [170]. A comparison of the surface morphologies of samples TPC^* and TPPC^* (see Figures 4-2b and 4-2c) supports our interpretation, since a higher light scattering is expected from the surface with smaller-scale structure.

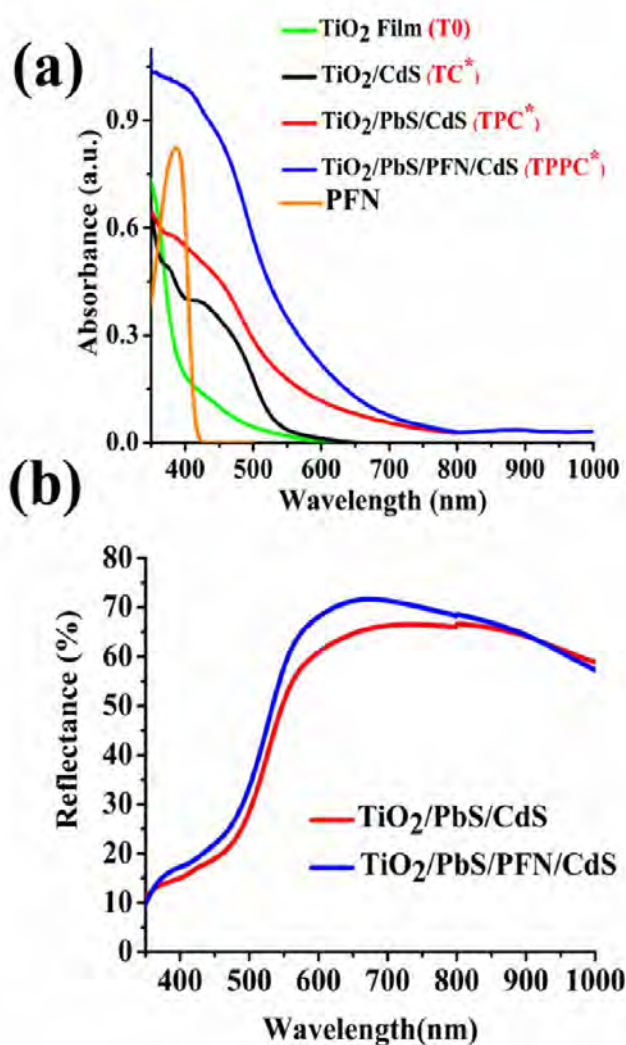


Figure 4-3. (a) Absorption spectra of samples T0 , TC^* , TPC^* , TPPC^* and PFN, (b) Diffuse reflectance spectra of sample TPC^* and TPPC^* .

4.3.3 Electrochemical Characterization

Figure 4-4 displays the J-V curves for the Hybrid Quantum Dots Sensitized Solar Cells (HyQDSSCs); the corresponding short-circuit current density, open-circuit voltage, fill factor, and photoconversion efficiency are summarized in Table 4-1. The results show an increment of photocurrent of up to ~53% with the introduction of PbS but the voltage and fill factor were reduced up to ~20% and ~15%, respectively; as a result the photoconversion efficiency remains unchanged. With the addition of both PbS and PFN the photocurrent increased up to ~100% and the voltage was reduced only ~5%; although the FF was reduced by ~25%, the photoconversion efficiency increased up to ~45%. Such results confirm the contribution of PFN to diminishing the PbS deterioration reported previously [72], resulting in an improvement of the photoconversion efficiency. Understanding the physical mechanism behind such processes can provide information to help design more efficient photovoltaic devices.

A comparison of the J-V curves corresponding to the samples with and without PbS QDs (TPCZ and TCZ) shows an increment in the short circuit current and a decrement in the open circuit voltage after incorporation of the PbS nanoparticles. This increment in J_{sc} is attributed to the increased light absorption induced by the presence of PbS, while the reduction in V_{oc} is due to the movement in the fermi level and to an increment of the recombination rate [123, 144]. After the addition of PFN between PbS and CdS (sample TPPCZ), the current increased from 13.3 mA/cm² to 17.6 mA/cm², as a result, the efficiency increased by 38.5%, from 2.6% to 3.6% (compare samples TPCZ and TPPCZ). We propose that this current increment is due to PFN acting as a charge transport layer, as a protecting layer to avoid direct contact between the TiO₂/PbS layer and the electrolyte, and to an increased intralayer light scattering [171]. As proof of the roles of PFN as charge transport and scattering layers, we deposited it in different positions inside the solar cell: when PFN was deposited between the TiO₂ and the PbS (sample TPPCZ1), the current decreased, from 17.6 to 15.2 mA/cm², in comparison with the sample TPPCZ where PFN was located between PbS and CdS, see Figure 4-4 and Table 4-1. The deposition of PFN after CdS (sample TPCPZ) is detrimental for the current because the PFN is not helping the charge transport, the scattered light is not efficiently absorbed, and both PbS and CdS are

isolated from the polysulfide electrolyte; therefore, the current decreases dramatically from 17.6 mA/cm² to 5 mA/cm².

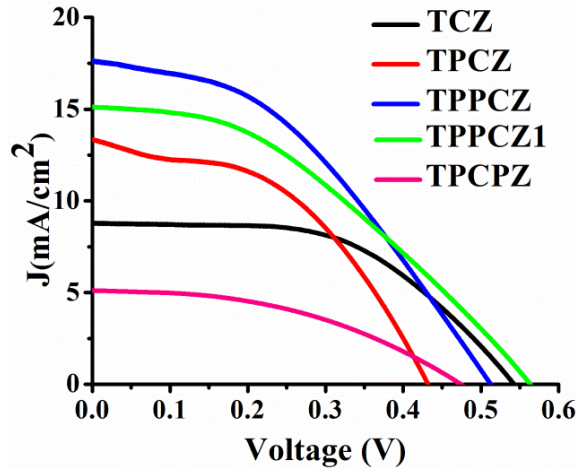


Figure 4-4. J-V curves of the different solar cells.

Samples	Configuration	$J_{sc}(mAcm^{-2})$	$V_{oc}(V)$	FF (%)	$\eta(\%)$
TCZ	TiO ₂ /CdS/ZnS	8.7	0.542	53.5	2.5
TPCZ	TiO ₂ /PbS/CdS/ZnS	13.3	0.432	45.9	2.6
TPPCZ	TiO ₂ /PbS/PFN/CdS/ZnS	17.6	0.513	40.3	3.6
TPPCZ1	TiO ₂ /PFN/PbS/CdS/ZnS	15.0	0.560	38.1	3.2
TPCPZ	TiO ₂ /PbS/CdS/PFN/ZnS	5.0	0.475	44.0	1.1

Table 4-1. Performance parameters for the QDSSCs studied in this work.

It is well known that the CdS layer helps to reduce the deterioration of the PbS QDs when it is deposited on top of them, since it avoids their interaction with the electrolyte resulting in a reduction of the recombination rate [123]. Thus, the additional layer of PFN also contributes with the protection of the TiO₂/PbS layer, decreasing even more the recombination rate between interfaces. According to the literature, the PbS conduction band (CB) is aligned with, or higher than, the TiO₂ CB when the nanoparticle size is between 3 and 5 nm. Consequently, the electrons can be easily transferred from PbS to TiO₂ [172]. The QDs synthesis and deposition were performed according to the procedure described in the literature [123]; therefore, we expect that the PbS CB would be aligned with that of the TiO₂ as observed in Figure 4-5 where a schematic energy diagram shows the effect of PFN

in different positions. Notice how the CdS certainly protects the PbS from the polysulfide electrolyte avoiding its deterioration, but this layer makes a barrier trapping the charge in PbS leading to recombination, see Figure 4-5a. This explains the reduction of the fill factor as has been reported in the literature [72] and will be explained later. When PFN is located between PbS and CdS (figure 4-5c), it should block electrons from CdS, but not from PbS, from being injected toward the TiO₂. In addition, PFN is also trapping holes from PbS which in turn, avoids recombination of electrons generated in PbS and this improves the charge transport. Blocking electrons from CdS results on a reduction of the FF (see table 4-1); such effect is worse when PFN is between the TiO₂ and the PbS (figure 4-5b) because the polymer is also blocking electrons from the PbS. From these results we conclude that the role of PFN is to improve hole transport (not electrons) and light scattering. There is CdS directly attached to the TiO₂, on top of PbS without PFN in the middle, and on top of PbS with PFN in the middle. In the last case, the CdS does not contribute to electron injection, thus explaining the reduction of the FF. When PFN is located between the TiO₂ and the PbS (TPPCZ1), see Figure 4-5b and Table 1, it acts like a barrier to avoid electron injection into the TiO₂; this explains the strong reduction of FF to 38.1%. The small increment of J_{sc} is the result of the contribution of PFN and perhaps some scattering produced by the interface PFN/PbS. As mentioned before, when PFN is located between PbS and CdS (see Figure 4-5c), the transport of holes is promoted and the recombination rate in the TiO₂/PbS interface is reduced. Such layer increases the light scattering and the absorption of the PbS QDs, which in turn, produces a strong increment of J_{sc} . However, the presence of CdS produces an effect similar to that described in Figure 4-5a, which explains the reduction of FF to 40.3%. The energy diagram presented in figure 4-5c also suggests that PFN is not favoring electron transfer from the CdS towards the TiO₂ because the LUMO of PFN is slightly higher than that of CdS. Nonetheless, CdS should be contributing to the current as observed in sample TCZ in Figure 4-4, meaning that electrons are transported from CdS through PFN. This is confirmed from the external quantum efficiency (QE) observed from the IPCE plot as will be discussed later. Finally, PFN is acting as a barrier when it is placed after CdS (see Figure 4-5d) avoiding the interaction with the electrolyte. This explains the strong diminution in J_{sc} , V_{oc} , and FF values; this produced a decrease in photoconversion efficiency.

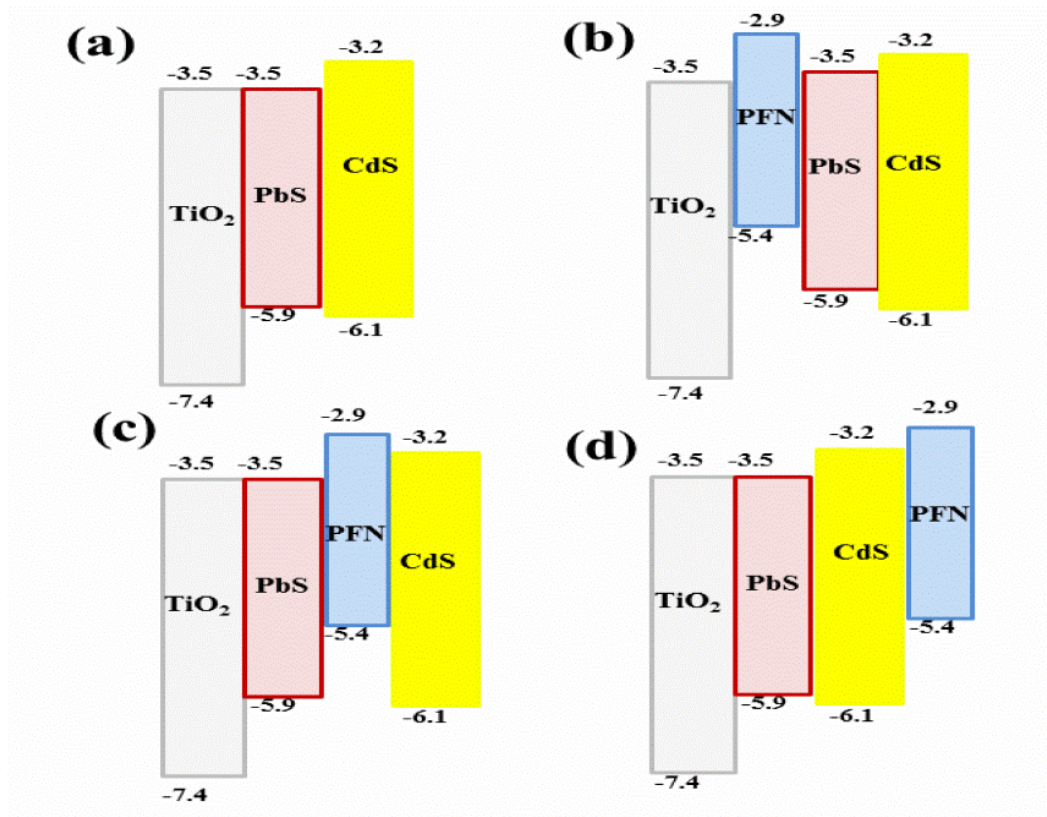


Figure 4-5. Energy level diagrams of devices: (a) TCZ, (b) TPCZ, (c) TPPCZ and (d) TPCPZ.

The IPCE values for all samples under study were calculated and are displayed in Figure 4-6. There, it is clearly observed that absorption of light in the infrared region is helping to photogenerate electrons and this absorption occurred as a result of PbS addition, compare sample TCZ with TPCZ, TPPCZ and TPPCZ1. This figure also shows the increment of IPCE upon incorporation of PFN, compare sample TPCZ with TPPCZ and TPPCZ1. Notice that the shape of the IPCE curve for those samples is maintained. This suggests that the enhancement comes from an increment of light absorption produced by intralayer light scattering. In fact, the strong decrease of the IPCE values for TPCPZ sample confirms that PFN after CdS isolates both active materials (PbS and CdS) from the electrolyte and interrupts the charge flux through the device. This barrier behavior was confirmed from sample TPPCZ1 where a strong reduction of IPCE was also observed. This suggests that PFN between PbS and CdS (sample TPPCZ) is promoting the hole transport from the former active material (PbS), see Figure 4-5c.

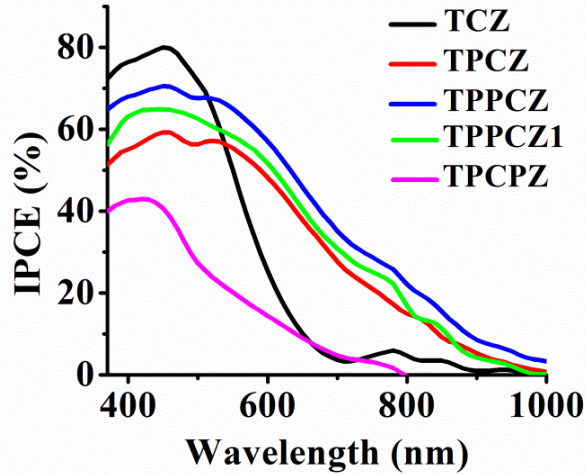


Figure 4-6. IPCE curves of devices fabricated in this work.

In order to understand the behavior of the physical processes that influence the overall efficiency of the cell, electrochemical impedance spectroscopy was performed. The analysis of the EIS curves was based on the model reported by Bisquert et. al. (see figure 2-6) [123, 124].

The variation in V_{oc} is typically associated to three factors: 1) an increment in short circuit current density, 2) an upward or downward displacement of the TiO_2 CB, and 3) the recombination resistance [173]. An increment in the photoabsorption will result in an increase in J_{sc} and, consequently, a shift in the J-V curve that will increase the V_{oc} . As previously discussed, the photoabsorption in the samples is increased, therefore we would expect a shift in the J-V curves so that V_{oc} , would increase; however, this is not observed.

Figure 4-7a shows the C_{μ} extracted from the EIS measurements under dark conditions as a function of V_F which is the voltage drop at the QDs sensitized electrode, it is obtained with the formula $V_F = V_{appl} - V_{series}$ [173], where V_{appl} is the total applied voltage and V_{series} is the voltage drop at the series resistance introduced by the electrical contacts. Here, it is clear that C_{μ} increases in comparison with TCZ, this means that the TiO_2 CB in the sample has a downward displacement with respect to the reference sample TCZ after addition of PbS. If PFN is introduced in the solar cell (sample TPPCZ) a downward movement of the TiO_2 CB is observed, but the displacement is less than for TPCZ. To compare the recombination resistance for the different samples, it is necessary to remove the effect of the band alignment when the TiO_2 is sensitized with QDs, so that the effect of

the TiO₂ CB shift is excluded. This procedure implies an equal electron density n , and is carried out by translating V_F until all the chemical capacitance curves overlap among them as shown in figure 4-7b. After this, a common equivalent conduction band V_{ecb} is obtained, defined as: $V_{ecb} = V_F - \Delta V_i$ [123], where ΔV_i is the voltage shift needed to overlap the chemical capacitance curves. The behavior of R_{rec} (figure 4-8a) indicates that the introduction of the PbS QDs (TPCZ samples) considerably reduces R_{rec} , which means an increase in the recombination processes; this will downshift the electron quasi Fermi level and reduce the V_{oc} . When PFN is added (TPPCZ sample) an increase in R_{rec} is observed in comparison to the TPCZ sample, but still being lower than the obtained for the TCZ sample. This implies that the introduction of PFN will reduce the recombination processes produced by the PbS QDs, but the system will still have higher recombination than the TCZ sample. Finally, considering the combination of the TiO₂ band shift and the changes in the recombination processes, the V_{oc} in TPCZ and TPPCZ should be lower than that in TCZ ($V_{oc}^{TCZ} \geq V_{oc}^{TPPCZ} \geq V_{oc}^{TPCZ}$), this is corroborated in the J-V curves of Figure 4-4 and in table 4-1.

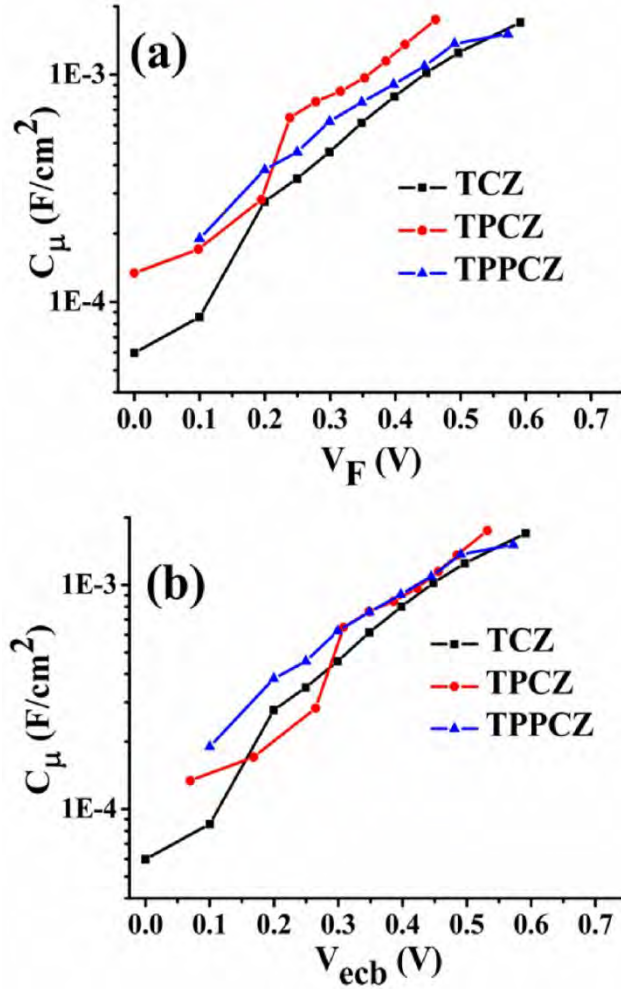


Figure 4-7. Chemical capacitance (C_μ) curves (a) as a function of voltage drop in the sensitized electrode, and (b) as a function of common equivalent conduction bands.

The FF is affected by the β value, a parameter related with the recombination rate (U_n) by the expression $U_n \sim n^\beta$ where n is the electron density. Therefore, low β values produce higher recombination rates that decrease the fill factor [124]. The β values were calculated from the slope of the R_{rec} vs V_F curve [123]. A decrement in transport resistance or an increment of the β value, increase the FF. In order to find the effect of PFN on the FF, we compare the behavior of samples TPCZ and TPPCZ. R_t and β values are lower in sample TPPCZ with respect to TPCZ, therefore a higher FF is expected from the R_t behavior; however, the β value is lower leading to a lower FF (see figure 4-8b). This means that the β value is a dominating parameter in our system since the FF decreased from 45.9 to 40.3 for sample TPPCZ with respect to sample TPCZ. Therefore, the presence of PFN was useful to reduce the recombination rate, to increase the charge transport rate as well as

light absorption, and to facilitate the electron extraction from the devices. The main result is an increment in V_{oc} , J_{sc} , and in the photoconversion efficiency from 2.6% to 3.6% for samples with only QDs versus QDs and PFN (samples TPCZ and TPPCZ).

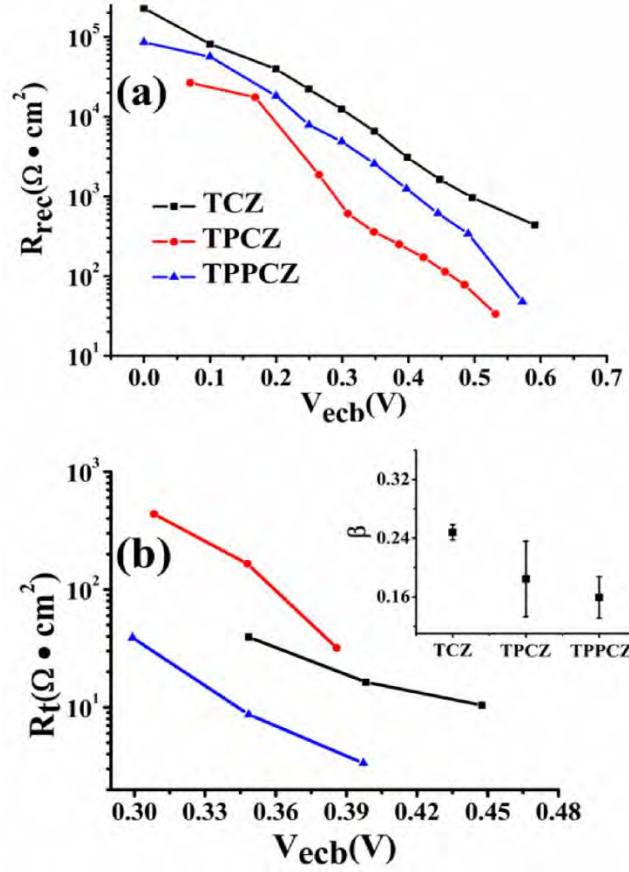


Figure 4-8. (a) Recombination resistance curves and (b) transport resistance as functions of common equivalent conduction band. Inset in Figure (b) shows the values of the β parameter.

4.4 Bismuth Sulfide (Bi_2S_3) Quantum Dots Sensitized Solar Cells

4.4.1 Optical characterization

The UV-VIS spectra of all samples under study, as well as the spectrum for a TiO_2 film similar to the one used in the cells, are shown in Figure 4-9. All the spectra have their maximum absorbance below 350 nm, this is attributed to the TiO_2 film. The band gap of ZnS is approximately 3.6 eV (345 nm); thus, we do not expect major absorption contributions from this component in our spectra [146]. The absorbance of the TCZ sample reaches up to 550 nm with a broad shoulder centered at 450 nm, corresponding to the absorption of CdS QDs [88]. The introduction of the Bi_2S_3 QDs (samples TCBZ and

TBCZ) extends the absorption band into the near infrared region, up to 800 nm, highlighting the importance of such sensitizer [174, 175]. Sample TCBZ shows higher absorbance than TBCZ due to the higher amount of QDs deposited by the difference in the number of SILAR cycles, six and three cycles for CdS and Bi₂S₃, respectively for TCBZ, and two cycles for both components in the TBCZ sample.

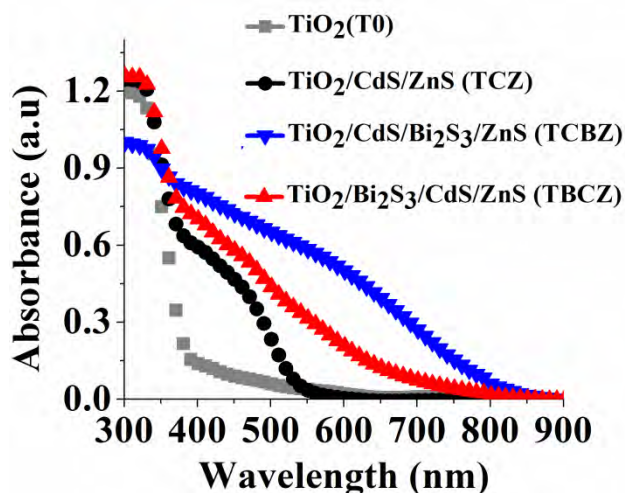


Figure 4-9. Absorption spectra of Bi₂S₃ and CdS QDs sensitized TiO₂ layer: TiO₂ (T0), TiO₂/CdS/ZnS (TCZ), TiO₂/ Bi₂S₃/CdS/ZnS (TBCZ), TiO₂/CdS/ Bi₂S₃/ZnS (TCBZ).

4.4.2 Electrochemical characterization

The current density-voltage (JV curves) for the different configurations of sensitized TiO₂ films are displayed in Figure 4-10. The resulting short circuit current densities, open-circuit voltages, and the calculated fill factors and efficiencies are summarized in Table 4-2. A J_{sc} of 7.9 mA/cm², V_{oc} of 512 mV, FF of 41.9%, and efficiency of 1.69% were obtained with the reference sample TCZ. The addition of Bi₂S₃ after CdS QDs (sample TCBZ) results in an increment of the photocurrent to 9.3 mA/cm² and of the FF to 2.52% representing an increment of 53%. However when Bi₂S₃ is deposited before the CdS QDs, there is a decrement of the photocurrent to 2.7 mA/cm² and of the V_{oc} to 378 mV, resulting in an efficiency of only 0.56%. The relative increment of 50% in the photoconversion efficiency in TCBZ is explained by the extended photo-absorption spectral range of the Bi₂S₃ QDs, and by the relative energy positions of the valence and conduction bands (VB and CB, respectively) of both sensitizers.

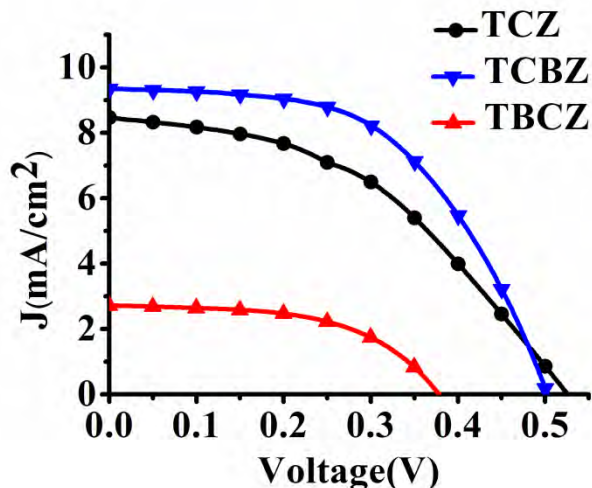


Figure 4-10. J–V curves of the different configurations under study

Sample	Configuration	$J_{sc}(\text{mA}/\text{cm}^2)$	$V_{oc}(\text{mV})$	FF(%)	$\eta(\%)$
TCZ	TiO ₂ /CdS/ZnS	7.9	512	41.9	1.69
TCBZ	TiO ₂ /CdS/Bi ₂ S ₃ /ZnS	9.3	502	53.7	2.52
TBCZ	TiO ₂ /Bi ₂ S ₃ /CdS/ZnS	2.7	378	54.8	0.56

Table 4-2. Performance parameters of solar cells studied in this work.

The energy diagrams for all samples under study were determined from Mott-Schottky plots [153] and are displayed in figure 4-11; the energy gap (E_g) was obtained from the absorption spectra. In that figure, panel (a) corresponds to the sample TCZ, where it is clear that the electron transport towards the electrode is favored in this configuration by the down-cascading arrangement of the CBs. The introduction of Bi₂S₃ QDs (configuration TCBZ) provides an energetically favorable arrangement of the TiO₂, CdS, and Bi₂S₃ conduction and valence bands (see Figure 4-10b) resulting on an increment of J_{sc} and FF of the system.

A detailed analysis of the device with the configuration TBCZ corroborates that such conduction band arrangement is responsible for the decreased characteristics of the photovoltaic device. From the diagram shown in panel 4-10c, it is clear that both, electrons and holes, face potential barriers at the Bi₂S₃/CdS interface. Although Bi₂S₃ and CdS QDs absorb light and electrons can move to the TiO₂ electrode from the Bi₂S₃, the generated holes are mostly blocked from reaching and interacting with the electrolyte. This is because

the CB and VB of CdS are below the corresponding energy bands of Bi_2S_3 . As expected, a significantly lower value (2.7 mA/cm^2 and a η of 0.56%) than those from the reference sample (TCZ) were obtained, despite the absorption spectrum of TBCZ extending into the near infrared.

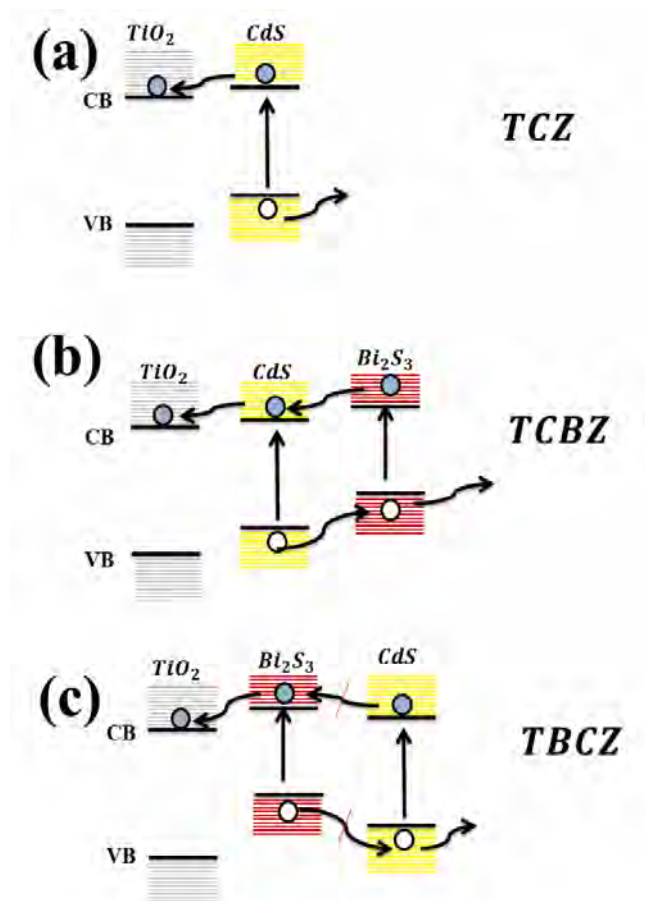


Figure 4-10. Energy level diagrams with different configurations of QDs sensitized TiO_2 films; (a) TCZ, (b) TBCZ, and (c) TCBZ configurations.

The IPCE curves for the three devices under consideration are shown in Figure 4-11a. All samples have a maximum IPCE between 410 and 480 nm, dominated by the photo-absorption of CdS [88]. The reference sample TCZ shows a maximum conversion efficiency of $\sim 45\%$ compared to the $\sim 60\%$ obtained for the TCBZ architecture that represents the highest IPCE value among all the samples under study. Notice the tail in the curve extending up to 900 nm associated to the incorporation of the Bi_2S_3 QDs, demonstrating that such sensitizer contributes to the improvement of the solar cell.

In contrast, there is a strong decrement in the IPCE for the sample TBCZ that reaches a maximum of only 20%; the curve does not show a contribution in the region corresponding to the Bi_2S_3 absorption. This indicates that the Bi_2S_3 in the TBCZ configuration does not inject electrons and at the same time interferes with the photogeneration or transport process of the CdS, resulting in a very low J_{sc} as discussed above (see Figure 4-10 and Table 4-2). The current for TBCZ is clearly reduced with respect to the reference TCZ. This is due to misalignment in the energy levels and by the low amount of material in the sample.

In addition to the JV curves, the integrated J_{sc} as a function of wavelength was estimated by integrating the product of the spectral curve of solar emission and the IPCE measured under low illumination; the result is shown in Figure 4-11b. The resulting J_{sc} average is lower, for all samples, in comparison to the measured JV curves. This disagreement can be attributed to the light reflecting in the surface due to the low illumination, since the intensity illumination for JV curves was considerably higher [176]. We see that the J_{sc} curve is enhanced, in comparison to sample TCZ, for wavelengths greater than approximately 600nm by the addition of Bi_2S_3 after the CdS QDs (sample TCBZ), showing the contribution of the Bi_2S_3 for this configuration. In contrast, for the TBCZ configuration the J_{sc} curve is almost flat after 600 nm, meaning that the Bi_2S_3 contributes little in this configuration.

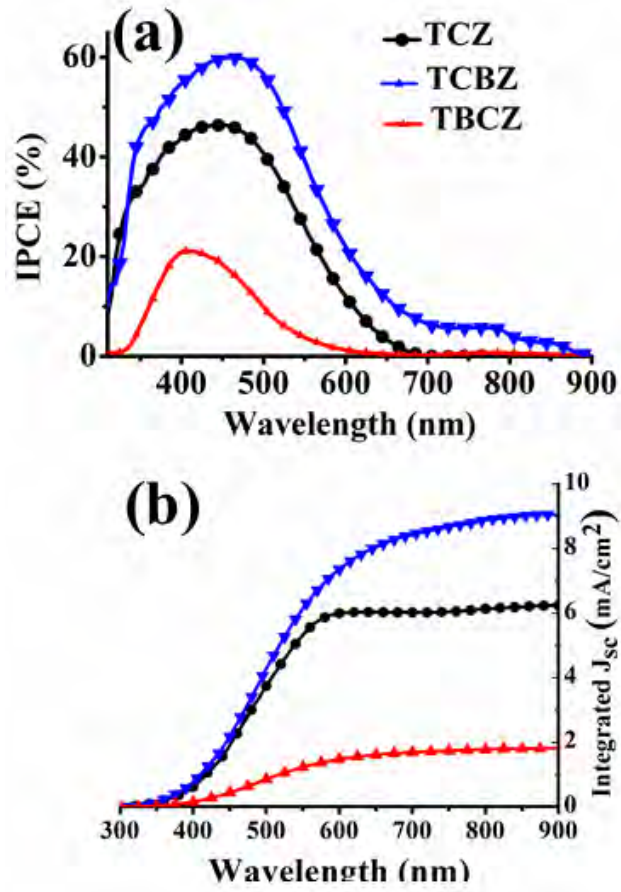


Figure 4-11. (a) IPCE curves for the three configurations under study. (b) Integrated J_{sc} obtained from the IPCE curve.

4.4.2 Electrochemical impedance

To better understand the physical processes behind the behavior of the relevant parameters for the cells, we performed electrochemical impedance spectroscopy measurements. The EIS data were fit using the transmission line model shown in Figure 2-6 [121-124].

The results from the EIS experiments are displayed in Figure 4-12. In particular, panel (a) shows C_μ extracted from the EIS measurements under dark conditions for the different configurations. In this plot, C_μ is presented as a function of $V_f = V_{app} - V_{series}$ [173], where V_{app} is the applied voltage during the measurement and V_{series} is the voltage drop due to the series resistance [88, 121]. As mentioned before, an increase in C_μ for a fixed voltage suggests a displacement of the TiO_2 CB towards lower energies. As R_{rec} and R_t are exponentially dependent on the energy level density [173] (i.e. the distance to CB), in order to correctly evaluate these parameters we need to define a new potential in such a way that the measurements be at the same equivalent position with respect to the CB for each device. This is accomplished by defining an equivalent conduction band potential (V_{ecb}) [123] as:

$$V_{ecb} = V_F - \Delta V_i;$$

in this expression ΔV_i is the voltage shift necessary so that the C_μ curves overlap, the result of this procedure is shown in Figure 4-12b. It is clear that for the sample TBCZ the value of C_μ has a plateau for $V_{ecb} > 300$ mV; this behavior is similar to the one observed in TiO_2 nanostructured electrodes in aqueous electrolyte without light absorber, and in DSSCs with ionic liquid as hole conductor [177]. According to the literature, the existence of this plateau in the graph is strong evidence that band unpinning occurs by the charging of deep surface states [144]. These surface state defects might induce recombination through mono-energetic levels in the band gap reducing the photocurrent [178]. This result is consistent with the poor J_{sc} and IPCE observed for this sample. On the other hand, the TCBZ configuration displays similar general characteristic of the chemical capacitance as the TiO_2 film with no plateau feature, leading to a good mobility of electrons/holes [178]. Using the transmission line model presented in Figure 2-6, the values for R_{rec} , the resistance against recombination of electrons from the TiO_2 conduction band to acceptors levels in the

electrolyte and TiO_2/QDs interface, were obtained and are displayed in Figure 4-12c. Higher values of R_{rec} mean less recombination.

Results indicate that the introduction of the Bi_2S_3 QDs in the configuration TCBZ slightly decreases the recombination resistance, implying an increased electron-hole recombination. This increment in the recombination processes results in a small downshift of the electron Fermi level and the V_{oc} , as observed in figure 4-12a [87, 149]. In the case of TBCZ the reduction in R_{rec} is a little stronger than for TCBZ; however, the reduction in V_{oc} is much larger than the expected for the increment in the recombination process. This is because the strong reduction in the photocurrent due to a lower number of electrons in the TiO_2 conduction band and a lower position of the Fermi level. This, together with the barrier for hole injection and the surface state defects mentioned earlier, explains the low performance of this sample. The configuration TCBZ does not suffer from these problems.

The behavior of V_{oc} is controlled by three competing processes: 1) light absorption intensity, 2) shifts in the TiO_2 CB, and/or 3) recombination rate. An increase in the photoabsorption will result in an increment in J_{sc} and V_{oc} ; however, as stated before, an increment in R_{rec} indicates a reduction in the electron recombination leading to a reduction of V_{oc} [87, 149]. When we compare the configuration TCBZ to TCZ, there is an increment in the absorption due to the incorporation of Bi_2S_3 but the EIS measurements show a partial decrement of the R_{rec} indicating a higher recombination rate.

Variations in the fill factor can be due to changes in the transport resistance, R_t [132, 173]. A detailed analysis of R_t , the resistance to the electron movement, shows that all samples have almost the same resistance; however, the sample TCBZ has a slightly lower value (see Figure 4-12 d). A lower value of R_t means a more efficient electron transport having an impact on the FF [121, 132], corresponding to a higher observed FF for this sample of 53%.

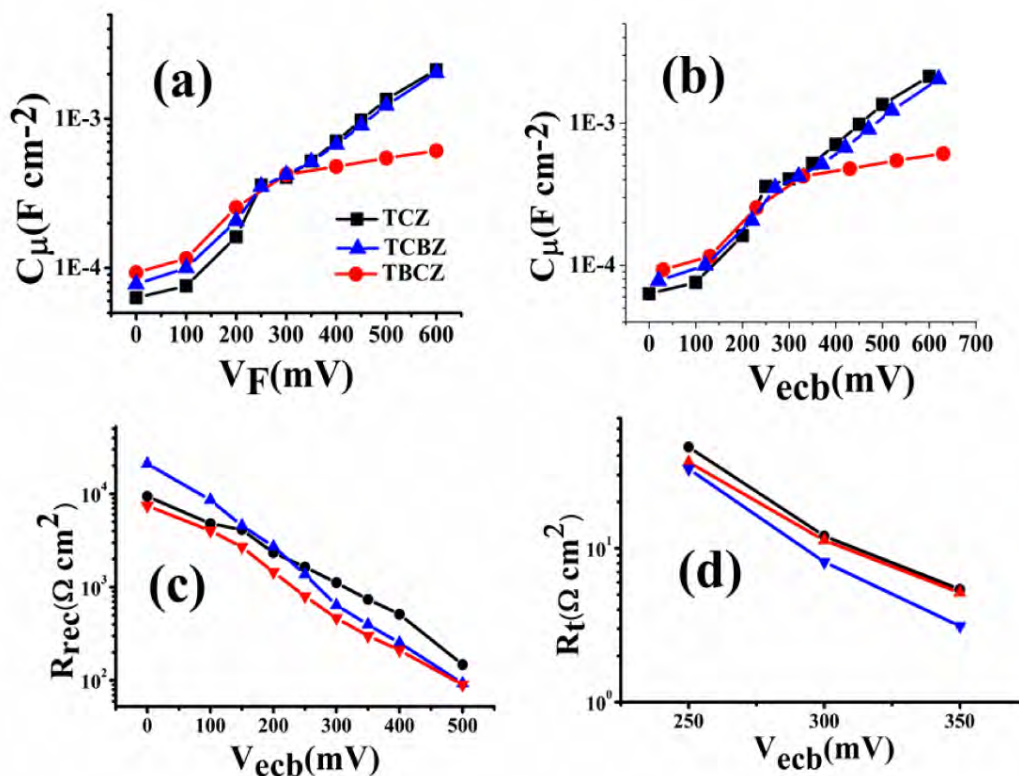


Figure 4-12. Electrochemical impedance spectroscopy characterization of TiO₂/CdS/ZnS (TCZ), TiO₂/Bi₂S₃/CdS/ZnS (TBCZ), TiO₂/CdS/ Bi₂S₃/ZnS(TCBZ) films: (a) Chemical capacitance C_{μ} as a function of voltage drop in the electrode. (b) Chemical capacitance C_{μ} as a function of common equivalent conduction band. (c) Recombination resistance, R_{rec} . (d) Transport resistance R_t as a functions of voltage equivalent conduction band V_{ECB} .

4.5 Colloidal CdSeTe QDs

4.5.1 Morphological characterization

The QDs synthesized by different techniques were characterized by TEM. The measured average size of CdS, and ZnS QDs synthesized on TiO₂ nanoparticles by SILAR method is 3 nm, measured directly from HRTEM images. The colloidal CdSe QRs have an average size of 10 nm length and 5 nm width, in correspondence with our previous work [63]. The Figure 4-13 shows a typical HRTEM image of CdSeTe₈₀₀ QDs showing the crystalline structure, and its size distribution showing an average size of ~ 9.5 nm. It was observed that the particle size depended of the Se concentration. In this work, concentration was changed from 0.026 to 0.132 g; resulting in nanocrystals of size ranging from 3 nm to 9.5 nm, see Figure 4-13. The relation between size and peak absorption is: 3nm correspond to 684nm,

4.5nm to 710nm, 7nm to 784nm and 9nm to 800 nm, in the image is labeled the type of quantum dot with the absorption peak.

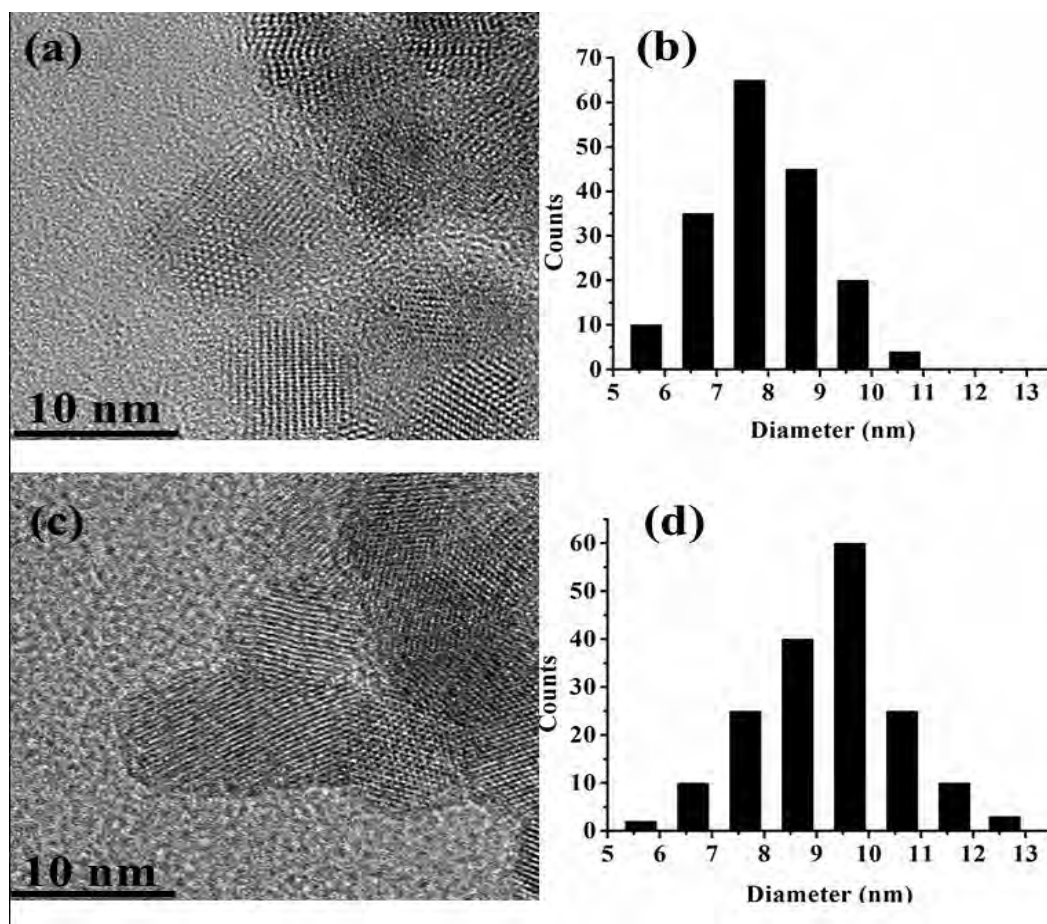


Figure 4-13. HRTEM image and their particle size distribution of (a-b) CdSeTe₇₈₄ QDs and (c,d) CdSeTe₈₀₀ QDs.

4.5.2 Optical characterization

The UV-VIS absorption spectra of CdSe QRs and different CdSeTe QDs are shown in Figure 4-14. It is observed a well-defined absorption bands at 650 nm, 684 nm, 710 nm, 780 nm and 800 nm for labeled CdSe, CdSeTe₆₈₄, CdSeTe₇₁₀, CdSeTe₇₈₀ and CdSeTe₈₀₀, respectively. Hereafter we refer to CdSeTe₈₀₀ QDs (just CdSeTe QDs) if nothing else is indicated. The red-shift in the spectrum is produced by the increase in particle size and it also depends the concentration of selenium [164]. Note that, in addition to the band gap

shift to longer wavelengths there is a reduction of absorbance in the visible region for larger QDs.

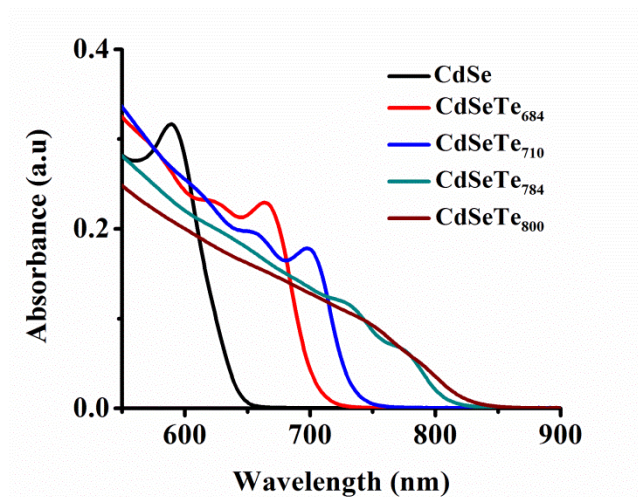


Figure 4-14. Absorption spectra of different CdSeTe QDs synthesized in the lab.

The cross-section SEM images and EDS analysis of substrates with multi-stacked QDs with configuration of CdS/CdSe/CdSeTe are displayed in Figure 4-15. All layers composing the device are observed in figure 4-15. From right to left, the first film observed is FTO followed by TiO₂ compact layer (190 nm), the transparent layer (9 μ m) composed of 20 nm TiO₂ nanoparticles, and finally the TiO₂ scattering layer (8 μ m) composed of 200 nm TiO₂ nanoparticles.

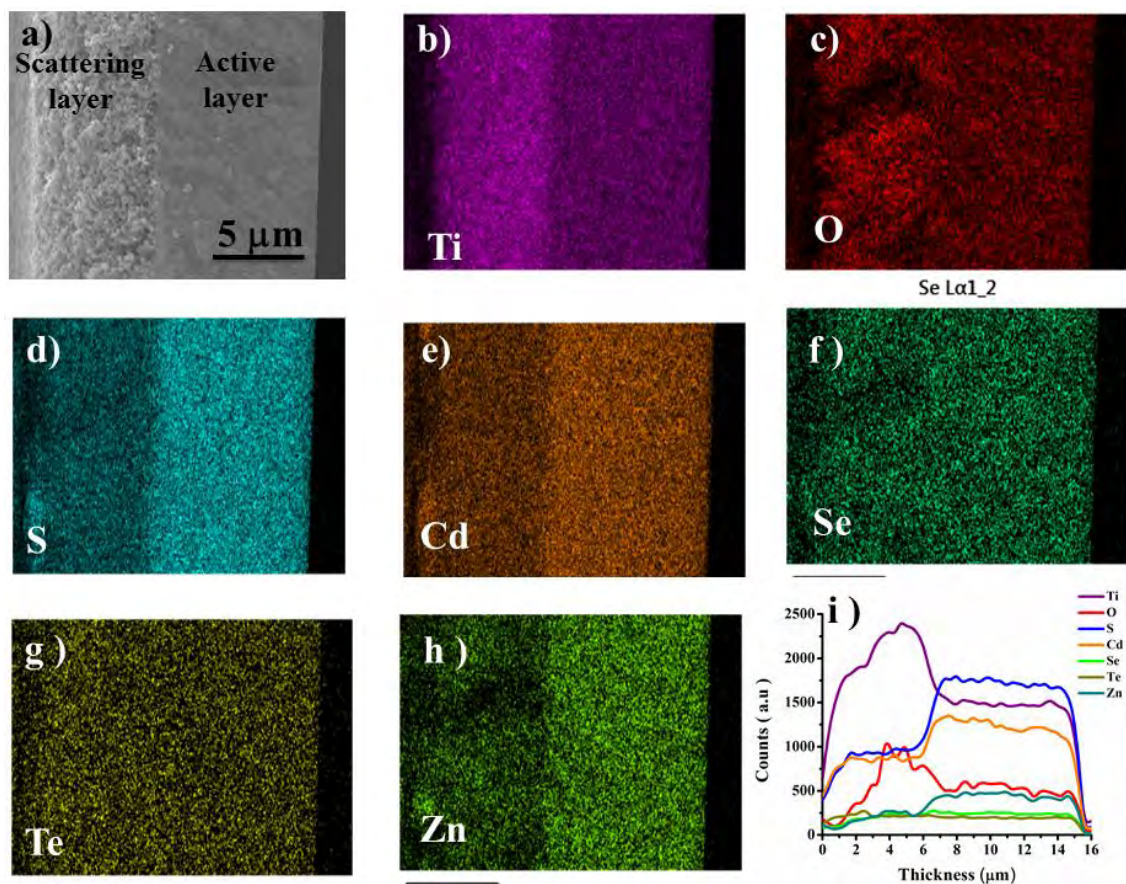


Figure 4-15. (a) Cross-section SEM images of $\text{TiO}_2/\text{CdS}/\text{CdSe}/\text{CdSeTe}$ QDs films sensitized by electrophoretic and pipetting method with TiO_2 compact layer (190 nm), transparent layer (9 μm) and scattering layer (8 μm); b)-h) EDS mapping of Ti, O, S, Cd, Zn, Te and Se atoms respectively i) The distribution through TiO_2 films as a function of multi-stacked QDs.

The Ti, O, S, Cd, Se, Te and Zn atoms distributions detected by EDS mappings are shown in Figure 4-15b through 4-15h, respectively. EDS characterization highlights the uniform distribution of multi-stacked QDs inside the mesoporous TiO_2 films increasing the concentration in transparent layer, which is consistent with the higher effective surface area of the TiO_2 nanoparticles in this layer, see figure 4-15i. The homogenous high porous TiO_2 transparent and opaque layer uniformly covered by QDs and QRs are observed from SEM images in figure 4-16.

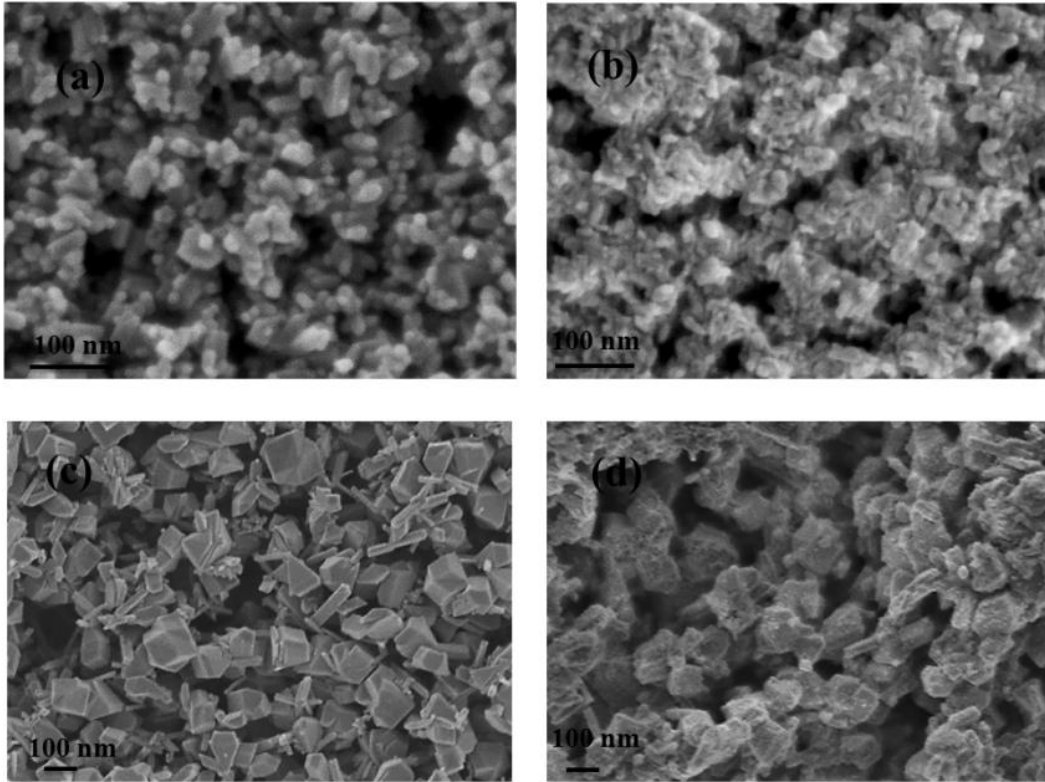


Figure 4-16. Scanning Electronic Microscopy (SEM) images of different configuration. a) TiO_2 transparent layer, b) $\text{TiO}_2/\text{CdS}/\text{CdSe}/\text{CdSeTe}/\text{ZnS}$, where CdS were deposited by SILAR method, c) TiO_2 opaque layer d) $\text{TiO}_2/\text{CdS}/\text{CdSe}/\text{CdSeTe}/\text{ZnS}$ where CdSe and CdSeTe were deposited by electrophoretic method. In all cases ZnS(S) were deposited by SILAR method.

The absorption spectra of the samples where the TiO_2 was sensitized with different types of QDs are depicted in Figure 4-17 (those samples are not complete solar cells). The shoulder in the absorption spectra centered at 450 nm is associated to CdS deposited by SILAR process [88]. The CdSeTe QDs increases the absorption band to the infrared up to 800 nm. Interestingly, in the configurations $\text{TiO}_2/\text{CdS}/\text{CdSeTe}/\text{ZnS}$ and $\text{TiO}_2/\text{CdSeTe}/\text{CdS}/\text{ZnS}$ the absorption band extends into the infrared up to 800 nm. In fact, the absorption is extended to the infrared region with the introduction of CdSeTe QDs adsorbed on TiO_2 . The ZnS band gap is about 3.6 eV, which corresponds to an absorption band at 320 nm and does not influence significantly the absorption in the visible range.

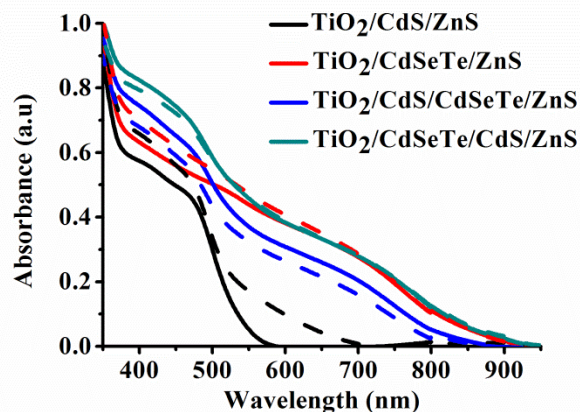


Figure 4-17. Absorption spectra of CdS and CdSeTe gradient QDs sensitized TiO_2 solar cells, $\text{TiO}_2/\text{CdS}/\text{ZnS}$, $\text{TiO}_2/\text{CdSeTe}/\text{ZnS}$, $\text{TiO}_2/\text{CdS}/\text{CdSeTe}/\text{ZnS}$ and $\text{TiO}_2/\text{CdSeTe}/\text{CdS}/\text{ZnS}$.

4.5.3 Electrochemical characterization

4.5.3.1 CdS and CdSeTe quantum dots sensitized solar cells

To have a better understanding of the working mechanisms in multi sensitized cells, the current density-voltage (J-V) curves of several configurations were measured, the results were consistent with our previous studies in this kind of solar cells [63]. Even though the PCE of CdSeTe sensitized cell is considerably low, absorption measurements suggest that this is not due to degradation of the CdSeTe QDs by the electrolyte [75]. When CdS and CdSeTe QDs are used in the configuration $\text{TiO}_2/\text{CdS}/\text{CdSeTe}/\text{ZnS}$, a considerable improvement of the PCE is observed (128 % with respect to the reference sample, $\text{TiO}_2/\text{CdS}/\text{ZnS}$, see Figure 4-18 and Table 4-3. This efficiency is principally due to an increment in the current J_{sc} in the cells (from 10 to 20 mA/cm^2), suggesting the contribution of photogenerated electrons in both, CdS and CdSeTe QDs. However when CdSeTe was situated between TiO_2 and CdS ($\text{TiO}_2/\text{CdSeTe}/\text{CdS}/\text{ZnS}$) the obtained PCE was as low as the one obtained for $\text{TiO}_2/\text{CdSeTe}/\text{ZnS}$ cells (1.3%), with a J_{sc} of 4 mA/cm^2 indicating a reduction in the photogeneration process or in the charge carrier recollection.

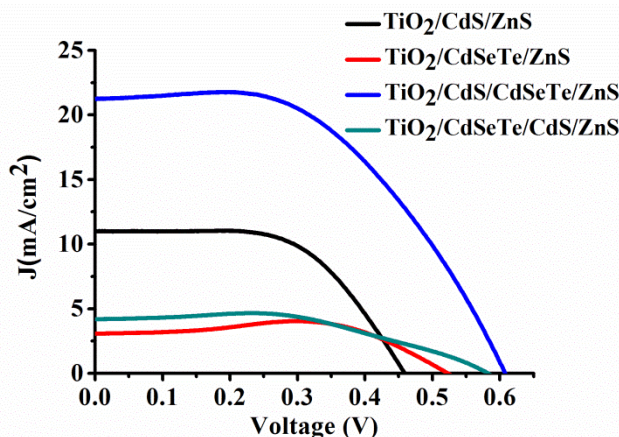


Figure 4-18. J–V curves of the different configurations under study.

Sample	J_{sc} (mA/cm ²)	V_{oc} (V)	FF(%)	η (%)
TiO ₂ /CdS/ZnS	10.5	0.459	58.6	2.8
TiO ₂ /CdSeTe/ZnS	2.9	0.522	83.3	1.2
TiO ₂ /CdS/CdSeTe/ZnS	20.3	0.608	51.0	6.4
TiO ₂ /CdSeTe/CdS/ZnS	4.0	0.582	55.0	1.3

Table 4-3. Photovoltaic parameters J_{sc} , V_{oc} , FF, and η extracted from J-V curves of the QDs sensitized TiO₂ solar cells with different configurations under study.

Detailed IPCE curves of the samples under study are displayed in Figure 4-19. Here it can be observed that the TiO₂/CdS/ZnS cell has a high light harvest region from ~ 400 nm to ~550 nm (IPCE > 75 %) corresponding to the CdS QDs absorption and a small tail around the range from 550 to 650 nm, probably due to trap states at the band gap. The IPCE curves for TiO₂/CdSeTe/ZnS indicate that the QE of these cells is very low in the visible and infrared region (<10%); however, the absorption study indicates that these samples effectively absorb light with $\lambda < 900$ nm, this result suggest that there is a problem in the electron transport from the CdSeTe gradient QDs to the TiO₂. The IPCE curve for TiO₂/CdS/CdSeTe/ZnS presents a wide range of photo generation with well-defined peaks at 450 nm and 800 nm with QE ~80% and ~40%, respectively. This behavior corresponds to the QE of the CdS QDs extended to the absorption range of the CdSeTe QDs, confirming that the increase of photocurrent observed for this sample in the J-V curve is due to the contribution of the photogenerated electrons of both kinds of QDs. However, for the TiO₂/CdSeTe/CdS/ZnS configuration, this behavior is not observed, even though this sample has a similar absorption spectra than TiO₂ /CdS/CdSeTe /ZnS, it has a very low QE in the visible region. Then, when CdSeTe QDs is placed between CdS and TiO₂ not only

the electrons photogenerated in the CdSeTe QDs do not reach the TiO₂ but also the electrons coming from the CdS QDs are reduced, indicating that something in this configuration inhibits the electron injection process from the QDs to the TiO₂ film, in comparison to the TiO₂/CdS/CdSeTe/ZnS configuration, where the electron injection process is fomented.

In addition to the JV curves, the integrated J_{sc} as a function of wavelength was estimated; the result is shown in Figure 4-19b. The resulting J_{sc} average is lower, for all samples, in comparison to the measured JV curves. This disagreement can be attributed to the light reflecting in the surface due to the low illumination, since the intensity illumination for JV curves was considerably higher [176]. In this spectrum, the dependence of the injected electrons on the TiO₂ with respect to the absorbed light wavelength is observed, for the configuration TiO₂/CdS/ZnS the curve grows until 650 nm, indicating that the injection of electrons finishes in this wavelength. The configuration TiO₂/CdSeTe/ZnS does not present electron injection in the NIR region, and only presents injection in the ultra violet region (450 nm). In consequence, this sample has a low photocurrent. The configuration TiO₂/CdS/CdSeTe/ZnS presents electron injection in the visible and NIR region (300-800 nm), this electron injection improves the photocurrent in the cell. However the configuration TiO₂/CdSeTe/CdS/ZnS does not present electron injection in the cells.

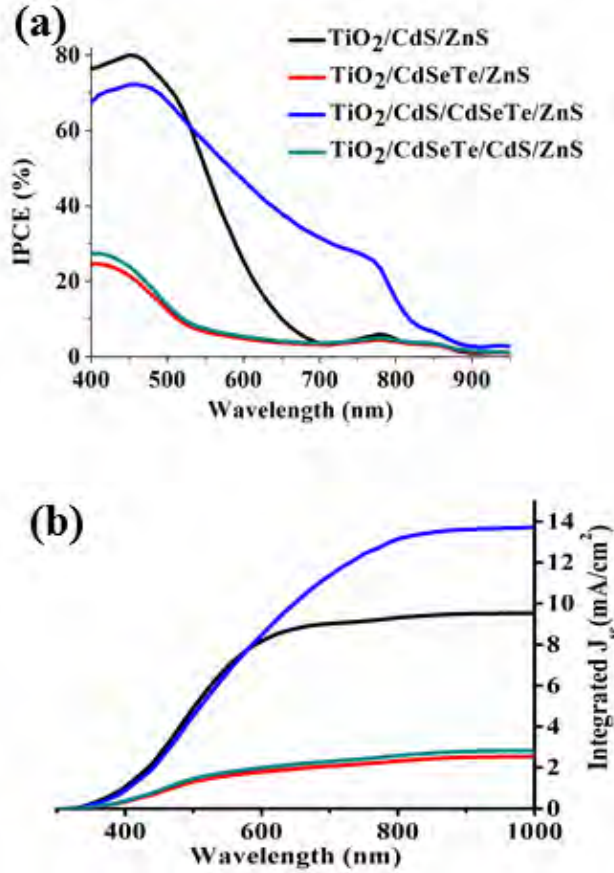


Figure 4-19 (a) IPCE curves of $\text{TiO}_2/\text{CdS}/\text{ZnS}$, $\text{TiO}_2/\text{CdSeTe}/\text{ZnS}$, $\text{TiO}_2/\text{CdS}/\text{CdSeTe}/\text{ZnS}$, and $\text{TiO}_2/\text{CdSeTe}/\text{CdS}/\text{ZnS}$ devices.. (b) Integrated J_{sc} obtained of IPCE curve.

4.5.3.2 CdS/CdSe/CdSeTe quantum dots sensitized solar cells

The absorption spectra of sensitized TiO_2 electrodes using different types of QDs are depicted in Figure 4-20. The shoulder in the absorption spectra centered at 450 nm is associated with CdS QDs deposited by SILAR process [88]. The addition of CdSe QRs increases the absorption band in the visible range and extends it from 550 nm to 650 nm being the characteristic band centered at 600 nm, but it is extended to the near infrared (NIR) up to 800 nm if CdSeTe QDs is added instead. Notice the reduction of absorption in the visible region in comparison with CdS/CdSe sensitized electrodes. Interestingly, the multi-stacked CdS/CdSe/CdSeTe configuration presents an extended absorption range in the NIR without loss of absorption in the visible region.

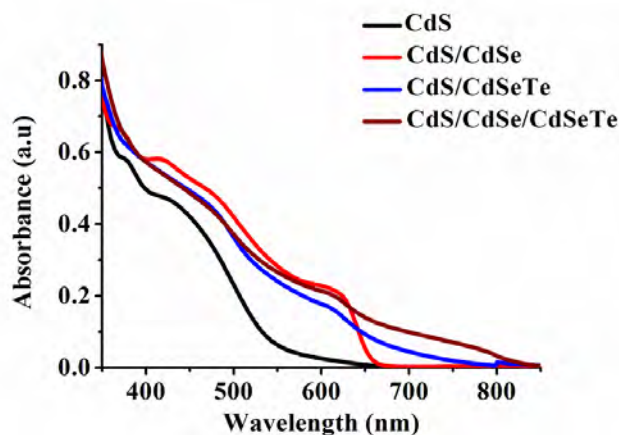


Figure 4-20. Absorption spectra of CdS QDs, CdSe QRs and CdSeTe QDs sensitized TiO_2 where CdS is deposited by SILAR method, CdSe QRs and CdSeTe QDs deposited by electrophoretic method.

Figure 4-21 shows the absorption spectra of sensitized electrodes using different sizes of CdSeTe QDs.

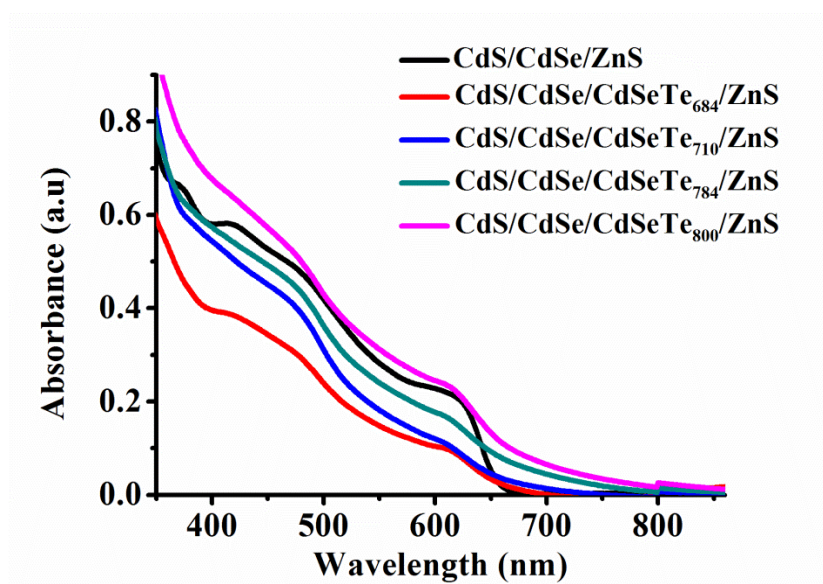


Figure 4-21. Absorption spectrum's of $\text{TiO}_2/\text{CdS}/\text{CdSe}/\text{CdSeTe}$ QDs, with different sizes of CdSeTe QDs.

The current density-voltage of multiple QDs in QDSSCs was measured and are displayed in Figure 4-22a. It is clearly observed that the PCE of 2.7% from CdS was improved with the addition of a second photoactive material, either CdSe QRs or CdSeTe QDs. Indeed, the use of multiple QDs sensitized electrodes CdS/CdSe/CdSeTe provide the

highest improvement of the solar cell device, see Figure 4-22a and Table 4.4. The PCE with the addition of CdSe QRs (CdS/CdSe) increased a 63 % with respect to CdS reference sample. In the Case of CdS/CdSeTe the efficiency is boost up to 4.9%, with a relative increase respect CdS reference of 81%. An outstanding PCE of 6.5% was obtained for multiple QDs, CdS/CdSe/CdSeTe, exhibiting a performance increase of 141% with respect to the reference device. The use of a SiO₂ layer increases the open circuit voltage from 0.588 V to 0.643 V for CdS/CdSe/CdSeTe/ZnS and CdS/CdSe/CdSeTe/ZnS/SiO₂ respectively, and enhances the PCE from 6.5 to 7.4%, respectively. Such increases in the PCEs are mainly attributed to the increase of the photocurrent J_{sc} as a result of the absorption bandwidth enlargement (~200 nm compared to CdS) as is confirmed from the IPCE measurements, see Figure 4-22b. However the increment of voltage is due to the introduction of the SiO₂ layer, this results from the control of the recombination rate.

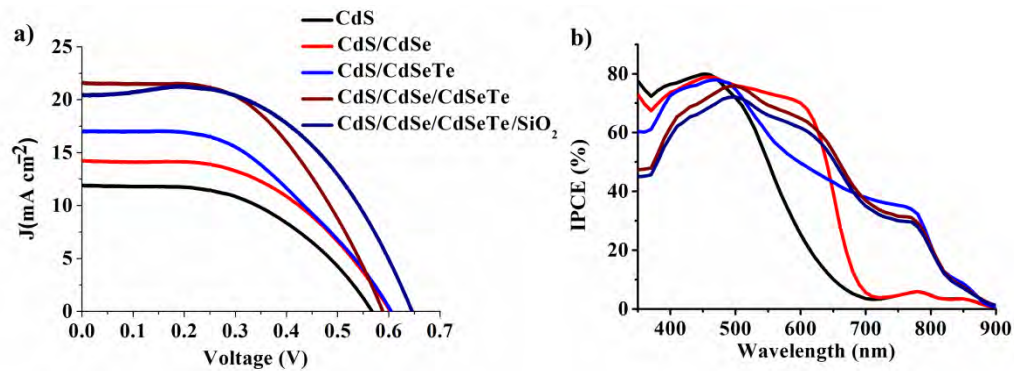


Figure 4-22. (a) J–V and (b) IPCE curves of CdS/ZnS, CdS/CdSe/ZnS, CdS/CdSeTe/ZnS, CdS/CdSe/CdSeTe/ZnS and CdS/CdSe/CdSeTe/ZnS/SiO₂ devices.

Sample	J_{sc} (mA cm ⁻²)	V_{oc} (V)	FF (%)	PCE(%)
CdS	8.8	0.546	55.6	2.7
CdS/CdSe	14.2	0.603	50.8	4.4
CdS/CdSeTe	16.9	0.604	47.5	4.9
CdS/CdSe/CdSeTe	21.5	0.588	51.5	6.5
CdS/CdSe/CdSeTe /SiO ₂	20.5	0.643	55.9	7.4

Table 4-4. Photovoltaic parameters J_{sc} , V_{oc} , FF, and PCE extracted from J-V curves of the best performing QDs and QRs sensitized TiO₂ solar cells with different configuration of multiples QDs

4.5.3.3 Tunable absorption with different sizes of CdSeTe QDs

Significant efficiencies have been also observed using other CdSeTe sizes, see Figure 4-23 and Table 4-5.

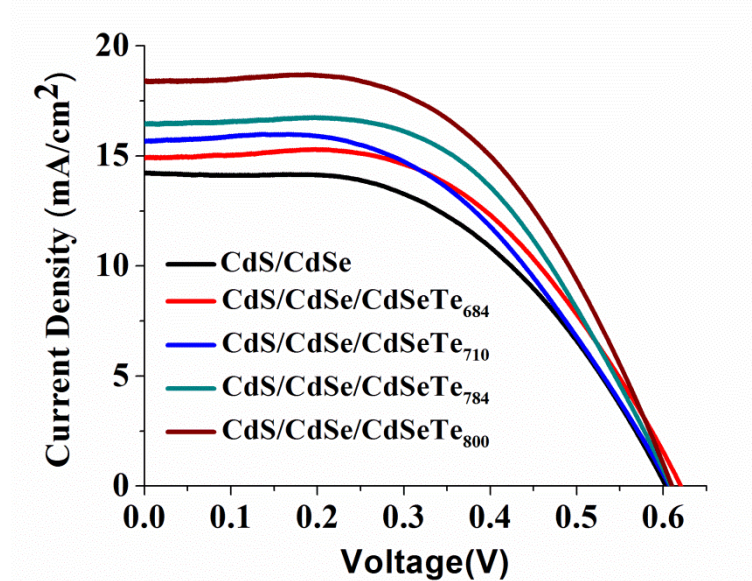


Figure 4-23. J–V curves of CdS/CdSe/ZnS, CdS/CdSeTe/ZnS with different sizes of CdSeTe QDs.

Sample	$J_{sc}(\text{mA}/\text{cm}^2)$	$V_{oc}(\text{V})$	FF(%)	$\eta(\%)$
CdS/CdSe	14.2	0.603	50.8	4.3
CdS/CdSe/CdSeTe ₆₈₄	14.3	0.609	52.8	4.6
CdS/CdSe/CdSeTe ₇₁₀	15.9	0.607	50.1	4.7
CdS/CdSe/CdSeTe ₇₈₄	16.4	0.608	54.5	5.4
CdS/CdSe/CdSeTe ₈₀₀	17.3	0.618	55.0	5.9

Table 4-5. Photovoltaic parameters J_{sc} , V_{oc} , FF, and PCE extracted from J-V curves of the various sized of QDs sensitized TiO₂ solar cells with different configuration of multi-stacked QDs.

Efficiency is decreased if just colloidal CdSe QRs or CdSeTe QDs are used as sensitizers without the previous deposition of CdS [63], obtaining 2 % and 0.07% efficiency respectively, see Figure 4-24.

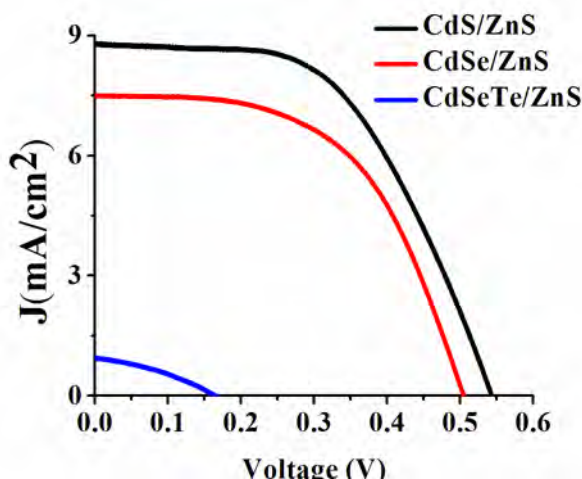


Figure 4-24. J–V curves of CdS/ZnS, CdSe/ZnS and CdSeTe/ZnS devices

4.5.4 Electrochemical impedance

Electrochemical impedance spectroscopy helped to determine the chemical capacitance, see Figure 4-25a. C_μ is plotted as a function of $V_f = V_{app} - V_{series}$ which is the voltage drop at the active electrode obtained from applied voltage, V_{app} , corrected by the voltage drop due to series resistance (V_{series}) [88, 173]. It can be observed in Figure 4-25a that the incorporation of CdSe QRs or CdSeTe QDs produces a slight upward shift of the chemical capacitance. This shift is most pronounced for multi-QDs CdS/CdSe/CdSeTe and indicates a downward shift of the TiO_2 conduction band. This observation is consistent with previous reports where an increase of the number of SILAR cycles [88] or the number of coating layers [122] produce the same effect. The progressive separation of the TiO_2 surface from the basic polysulfide electrolyte as different QDs are added originates the observed downward shifts in Figure 4-25a.

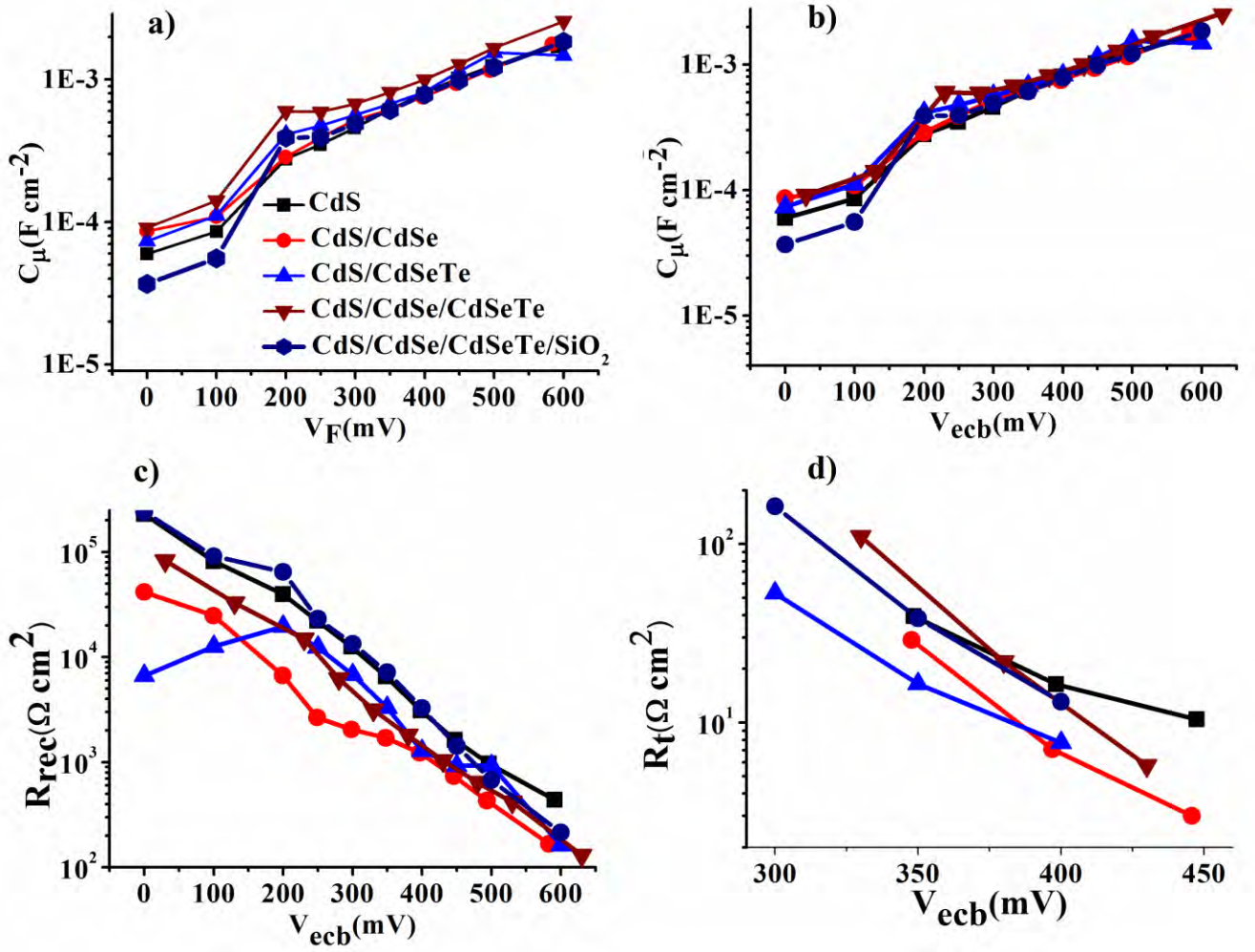


Figure 4-25. EIS characterization curves of devices fabricated in this work: a) and b) are Chemical capacitance (C_{μ}), c) Recombination resistance (R_{rec}), and d) Transport resistance R_t as a function of voltage equivalent conduction band (V_{ECB}).

For further investigation of the properties of the different electrodes the effect of the conduction band shift has been removed by the use of the equivalent conduction band (V_{ECB}), which is defined as: by, where V_F is a final voltage and is the voltage shift to the capacitance respect the sample used as reference, CdS sample, see Figure 4-25b were consequently the C_{μ} of the different samples overlaps when it is plotted against V_{ECB} . Other parameters such as recombination resistance, R_{rec} , and transport resistance, R_t , can be analyzed without the influence of the conduction band shift, see Figure 4-25c and 4-25d respectively. The introduction of additional sensitizers in the CdS reference sample produces an increase of recombination rate (lower recombination resistance) [87, 149], see

Figure 4-25c. An increase of recombination rate causes the reduction of V_{oc} . However, we can see that the V_{oc} of multi-QDs devices slightly increases, see Table 4-5, instead of being reduced as expected from the higher recombination rate and the slight downward shift of conduction band. This is due to a significantly higher photocurrent observed for multi-stacked cells that push V_{oc} up. In this sense, the deleterious effect of multi-QDs electrodes are compensated by a large increment of the photocurrent. Finally the use of the SiO_2 layer increased the recombination resistance (see Figure 4-25c), this indicates that the recombination rate is reduced and the voltage increased [163], see Table 4-5.

Chapter 5

Perovskite devices

5.1 Introduction

Organic halide Perovskites solar cells have attracted great attention due to their excellent performance in solar energy conversion. The typical structure of a perovskite solar cell is ABX_3 , where A corresponds to an organic cation i.e methylammonium $(CH_3NH_3)^+$, B is a large inorganic cation usually lead (II) (Pb^{2+}) and X_3 is a slightly smaller halogen anion usually chloride (Cl^-) , bromide (Br^-) or Iodide (I^-) .

The first report of perovskite solar cells was done by using dye sensitized solar cells, where the dye was replaced by perovskite material [179]. This type of cell provided a PCE of 3.8%. However, the electrolyte based iodides affected the perovskite material [179]. The next work was about perovskite sensitized QDs solar cells providing an PCE of 6.5% [180]. It was obtained using the mixture of CH_3NH_3I and PbI_2 in butyrolactone, which reduces the effect of contact between the perovskite and electrolyte. In 2012, a solid perovskite solar cell was reported where the electrolyte was replaced by an organic hole transport material (Spiro-Ometad), with the help of which the solar cell showed increased stability and a PCE of 9.7% [181].

The solid state perovskite solar cells were studied with different configurations, for example, replacing the TiO_2 layer by Al_2O_3 resulting in PCE of 10.7% [182]. Other configurations which reported a high voltage showed the replacement of PbI_2 by $PbBr_2$ resulting in $CH_3NH_3PbBr_3$ [183], or by mixing the halogens $CH_3NH_3PbI_{3-x}Br_x$, $CH_3NH_3PbI_{3-x}Cl_x$ with PCE of 12.7 and 11.7%, respectively [183]. Further the hole transport materials were studied where the spiro ometad was replaced by different materials like P3HT, PTAA and others obtaining a PCE of about 8.5% [184, 185]. The fabrication process of perovskite solar cells turns out to be very important. The implementation of sequential two step deposition method increase the crystal formation of perovskite films and pushes the PCE up to 15% [186]. Actually, the record PCE for perovskite solar cells is 22%, which was obtained with the mixture of two organic cations: methylammonium

iodide and formamidinium iodide, and further mixing the halogen anion bromide (Br-) and Iodide (I-) [21, 22, 187].

Organic halide perovskite has also been of great interest as emissive components in light emitting diodes (LEDs) [35]. It is possible to obtain highly luminescent nanoparticles with perovskite nanocrystals. Also this perovskite nanocrystals present quantum confinement effect and are named perovskite quantum dots (PQDs). The PQDs present high photoluminescence quantum yield (PLQY) of up to ~80% [76, 188]. The PQDs with this high PLQY can be introduced in solar cells and LEDs. [76, 189, 190].

Different types of PQDs are analyzed, of which the most important results are of $\text{CH}_3\text{NH}_3\text{PbBr}_3$, the mixing of halogen $\text{CH}_3\text{NH}_3\text{PbI}_{3-x}\text{Br}_x$ and $\text{CH}_3\text{NH}_3\text{PbCl}_{3-x}\text{Br}_x$ [191]. With these different compositions, it is possible to tune the emission in PQDs. The major problem with this type of nanocrystals is the degradation of the materials. Other types of PQDs can replace the $\text{CH}_3\text{NH}_3\text{X}$ by Cesium (CsX) where X is a smaller halogen anion usually chloride (Cl-), bromide (Br-) or Iodide (I-), obtaining all inorganic CsPbX_3 PQDs [192, 193].

5.3 Perovskite quantum dots

5.3.1 Synthesis of perovskite quantum dots

A series of CsPbX_3 QDs were synthesized using hot injection method with dry oleylamine (OLA) as the coligand and stabilizer. This synthesis process takes advantage of the ionic nature of chemical bond between the compounds, Cs^{2+} , Pb^{2+} and X^- . The CsPbX_3 nanocrystals were obtained by reacting cesium oleate with lead (II) halide (PbX_2) in octadecene at a temperature of 170°C. The Cs-oleate solution was prepared by mixing CsCO_3 (0.2 g, Sigma Aldrich, 99.9 %) with octadecene (10 ml, ODE, Sigma Aldrich, 99 %) and oleic acid (1 ml, OA, Sigma Aldrich, 99 %) in a 50 ml three-neck flask. The mixture is heated in the presence of nitrogen at 150 °C for complete solubilization of CsCO_3 and is kept at 100°C throughout the process. Further, a 1: 1 molar ratio of OA and

OLA with octadecene is added to the PbX_2 (0.376 mmol) for complete solubility and stabilization of synthesized nanocrystals. After complete solubilization, the PbX_2 mixture is heated to a temperature of 170°C , to which the Cs-oleate solution (1 ml in ODE) is added instantly. The reaction takes place so rapidly that the entire growth of nanocrystals occurs within 1-3 secs. It is observed that, the size of nanocrystals can be tuned just by controlling the reaction temperature instead of the growth time. The obtained crude solution is cooled in ice bath and the nanocrystals were separated by centrifugation. Finally the nanocrystals were dispersed in anhydrous chlorobenzene for their incorporation into the PSCs.

5.3.2 Optical characterization

CsPbX_3 ($\text{X}=\text{Cl}$, Br and I) QDs were synthesized using the hot injection method and characterized. Fig. 5.1(a) shows the picture image of one of the colloidal perovskite quantum dots (CPQDs) with different halogen compounds. The QDs are observed to have an average size of 9 nm with good homogeneity. Fig. 5.2(b) shows CIE color correspondent to the different CPQDs. Fig. 5.1(c) shows the photoluminescence spectra of the prepared QDs solution. The emission peak is tuned from 685 nm to 420 nm by replacing the lead (II) halide (PbX_2 , $\text{X}=\text{I}$, Br and Cl) in CsPbX_3 . Fig. 5.2(d) represents the UV-visible absorption spectra of the QDs solution.

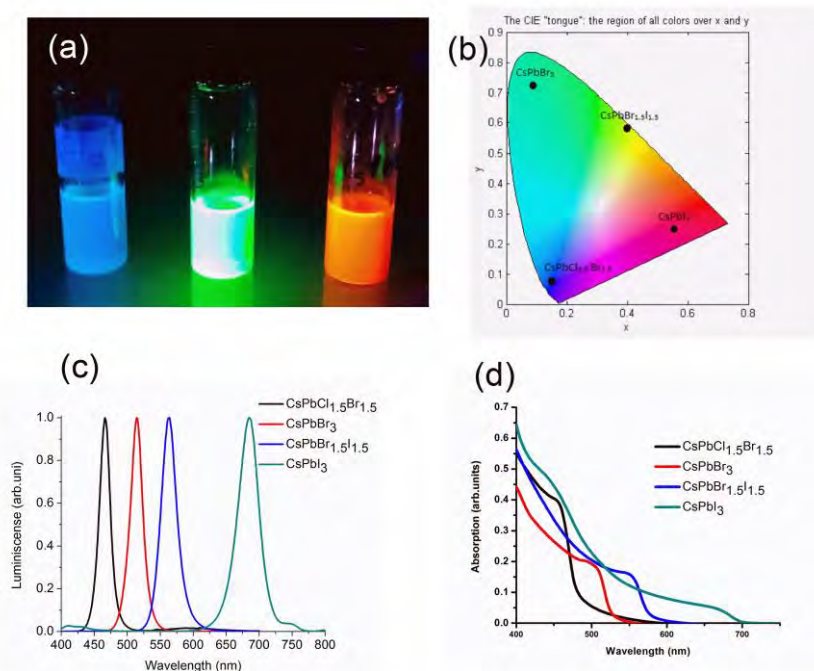


Figure 5.1 a) picture of the colloidal perovskite quantum dots. b) CIE color correspondent to the emission of the colloidal perovskite quantum dots. c) and d) Luminescence and absorption spectra of the perovskite quantum dots respectively.

5.2 Perovskite solar cells

5.2.1 Fabrication of perovskite solar cells

The fabrication procedure of the perovskite crystal in perovskite solar cells is very important, since the PCE enhancement depends on good crystal growth. A MAPbI₃ layer for perovskite solar cell can be prepared using different process like one step coating, sequential two step coating and vapor assisted method. One of the problems in the perovskite films is to resolve the solvent engineering methods. The Dimethylformamide (DMF) is a good solvent for MAPbI₃ dissolution and Dimethylsuloxano (DMSO) is used as a cosolvent in final solutions. Figure 5-2 shows a schematic representation of the fabrication processes involving one step spin coating. When the MAI+PbI₂ in DMF solvent is used, the MAPbI₃ crystal is not uniformly covering the total surface of the substrate, because the solubility of PbI₂ and MAI is different and the DMF rapidly evaporates. However, the use of DMSO helps the solubility and an adequate washing of DMF with

nonpolar solvent (diethyl ether in our case) turns out to be important to increase the crystal growth and making it possible to obtain highly regular films (Figure 5-1).

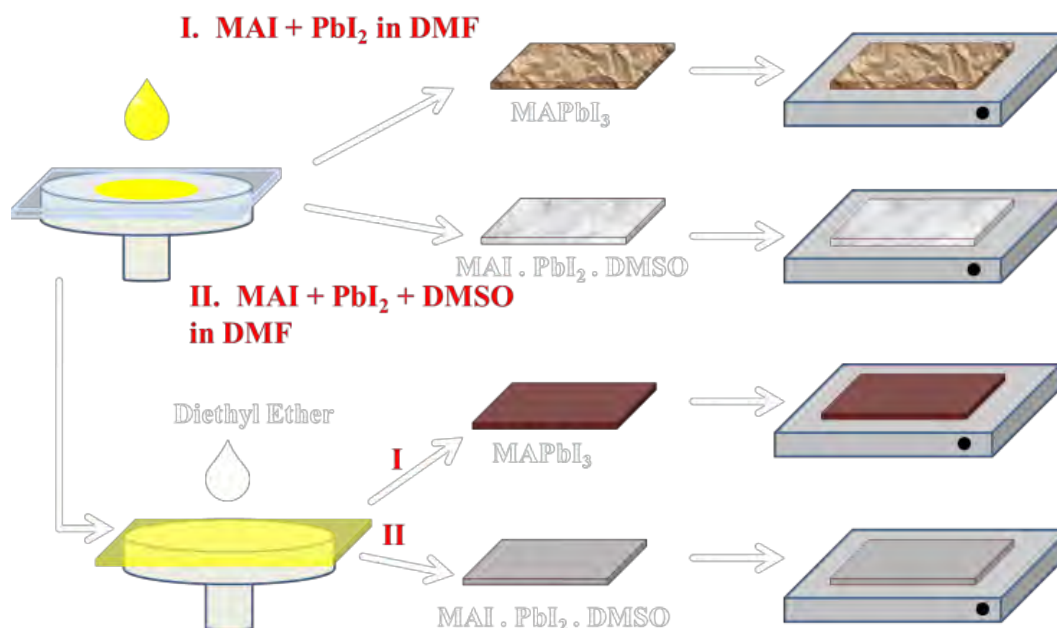


Figure 5-2 Schematically process to fabricate perovskite films, taken from reference [194]

5.2.2 Morphological characterization

One of the most important parameters to obtain good crystal growth is the time of diethyl ether deposition. Figure 5-3 shows that with only MAI+PbI₂+DMF, the crystal growth doesn't seem to be good and peeling effects are observed. However, the time of deposition of the nonpolar solvent, i.e diethyl ether, turns out to be very important. In our case, a good crystal growth and better morphology were obtained with a diethyl ether deposition of 3 secs. Increasing the time of deposition results in rapid evaporation of DMF and hence results in poor morphology of the perovskite films.

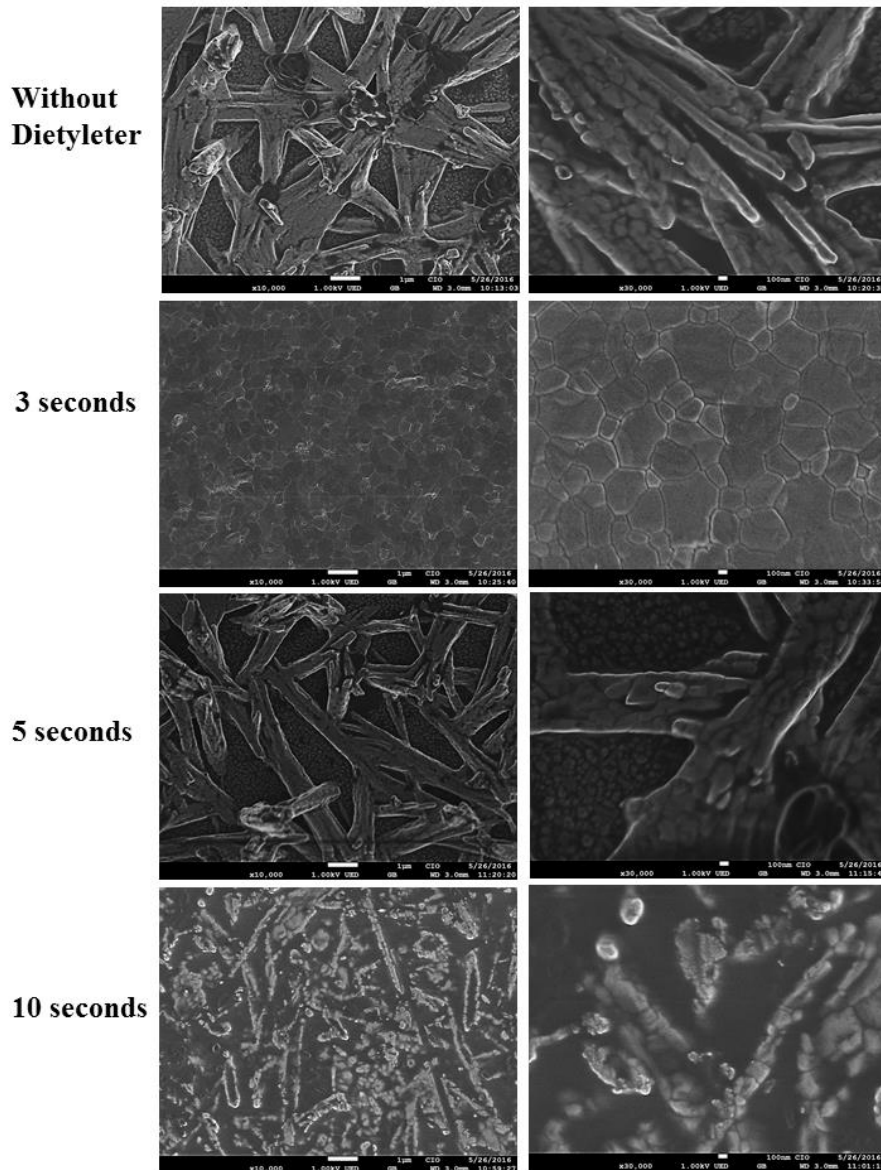


Figure 5-3 SEM images of perovskite films with different times of diethyl ether deposition.

Another parameter for consideration in the fabrication of perovskite solar cells is the annealing process. The controlled annealing process is very important for the formation of a better perovskite phase. Figure 5-4 shows the XRD spectrum for different compositions of perovskite solar cells. It shows TiO_2 with typical XRD peaks, peak for methylammonium lead iodide (MAPbI_3). However, the next configuration represents $\text{TiO}_2/\text{MAPbI}_3$ without annealing process. This XRD shows different peaks in the respective material, which is due to different phases of perovskite films. When the films are treated with an appropriate

annealing process the corresponding to orthorhombic crystal structure of perovskite film is obtained. Also the absorption of light, shown in Figure 5-5, depends on the annealing process of the perovskite films.

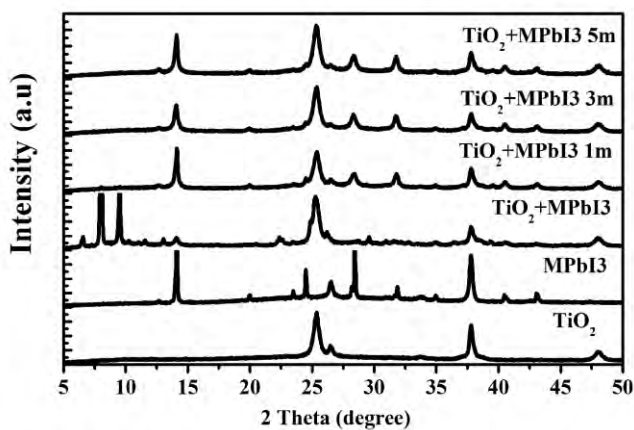


Figure 5-4 XRD spectra for the different materials in the perovskite solar cells.

5.2.3 Optical characterization

Figure 5-5 shows the absorption spectra of different configurations, depicting the importance of annealing time at 100°C. If the annealing time happens to be greater than 3 minutes, the absorption spectrum almost matches with the one with 3 minutes.

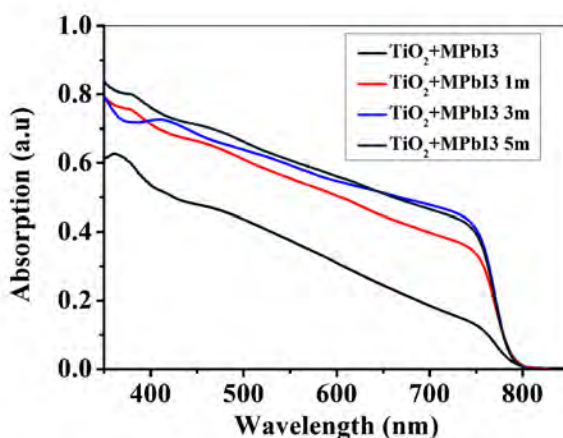


Figure 5-5. Absorption spectra of perovskite for different annealing times.

5.2.4 Electrochemical characterization

Figure 5.6 shows the JV curve for a perovskite solar cells obtained in our group. The configuration of the corresponding cell is FTO/TiO₂/MAPbI₃/Spiro-Ometad/Ag, which provides a PCE of 8% with 13 mA/cm² short circuit current, open circuit voltage of 0.95V and a fill factor of 64.2%.

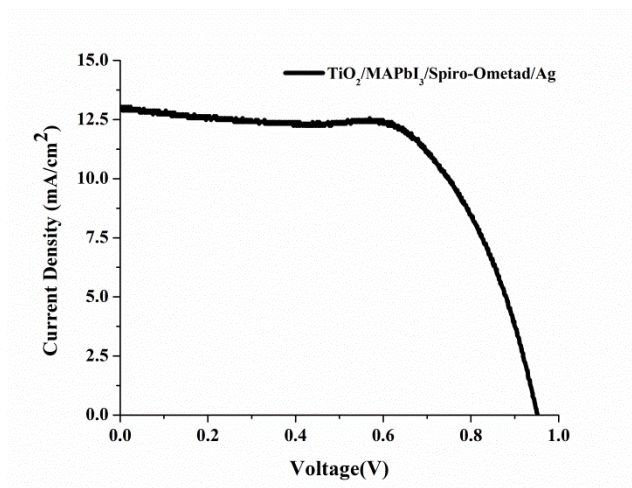


Figure 5-6 JV curve for perovskite solar cell

The high photocurrent shown in the IPCE spectrum (Figure 5-7), indicates electron photo-generation capacity from 800 to 400 nm.

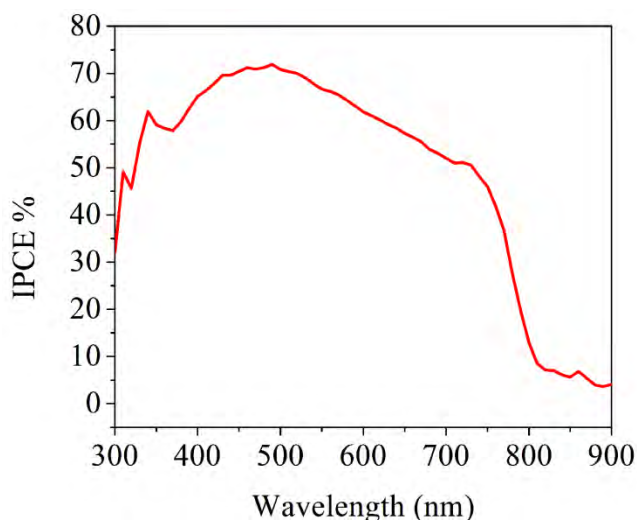


Figure 5-7 IPCE curve for perovskite solar cell

5.2.5 Perovskite quantum dots solar cells

The current-voltage (J-V) curves for the best PSC device with CsPbBr₃ and CsPbI₃ is shown in Fig. 5.8(a) and the corresponding photovoltaic parameters are indicated in Table.

5.1. The photovoltaic performance of the device has shown a significant change with the introduction of a layer of all-inorganic perovskite QD on top of bulk perovskite. The best control cell (FTO/TiO₂/CH₃NH₃PbI₃/HTM) provides a short current density (J_{sc}) of 13.17 mA/cm², open-circuit voltage (V_{oc}) of 0.95 V, fill factor (FF) of 62.34, yielding a PCE of 7.79 %. However, the introduction of CsPbBr₃ QDs at the interface of bulk perovskite and HTM increased the photo conversion efficiency to 9.24 % because of the increase in J_{sc} to 14.86 mA/cm² and FF to 67.21. Interestingly, the inclusion of CsPbI₃ QDs at the interface has shown much pronounced effect with an increment of PCE by 47 % when compared to the control cell. This device provides a J_{sc} of 17.73 mA/cm², V_{oc} of 0.92 V and FF of 70.21 corresponding to an efficiency of 11.51 %.

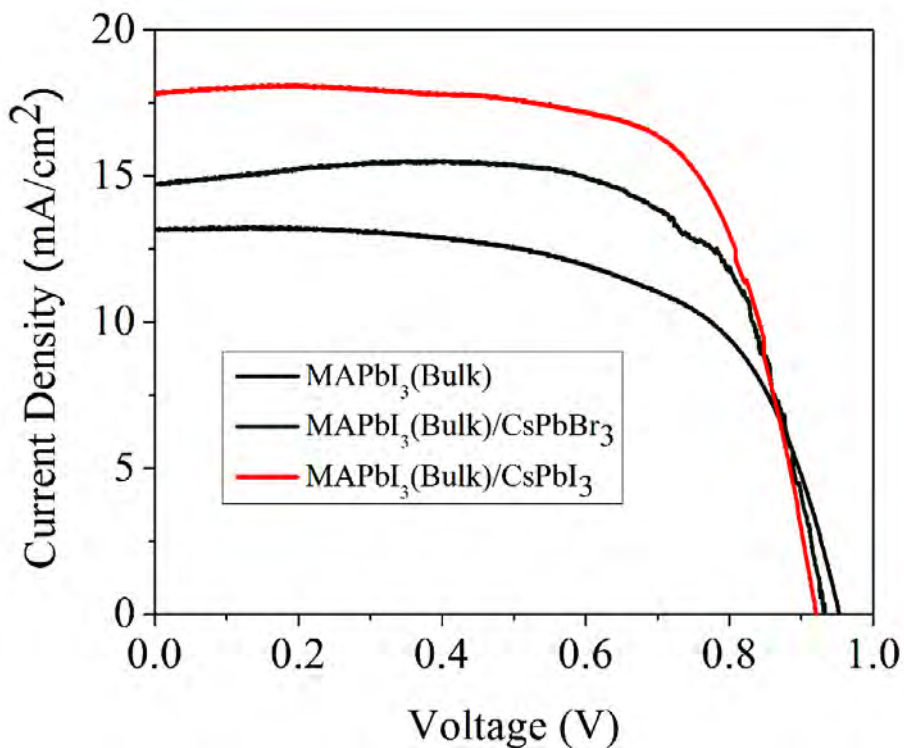


Figure 5.8 IV curves for MAPbI₃ perovskite solar cells in bulk, and add the CsPbBr₃ and CsPbI₃ perovskite quantum dots.

Table 5.1. Parameters of the perovskite solar cells in bulk, and add the CsPbBr₃ and CsPbI₃ perovskite quantum dots.

Device	J_{sc} (mA/cm ²)	V_{oc} (V)	FF(%)	PCE(%)
MAPbI ₃ (Bulk)	13.17	0.95	62.3	7.7
MAPbI ₃ (Bulk)/CsPbBr ₃	14.6	0.93	70.2	9.5
MAPbI ₃ (Bulk)/CsPbI ₃	17.7	0.92	70.6	11.5

Fig. 5.9 shows the incident photon conversion efficiency (IPCE) of each cell. The IPCE increases in the order of CH₃NH₃PbI₃ (Bulk) < CH₃NH₃PbI₃ (Bulk)/CsPbBr₃/ CH₃NH₃PbI₃ (Bulk)/CsPbI₃. The integrated current density values calculated from IPCE is in good agreement with the measured current density. The IPCE characteristics of QD based

tandem PSC is higher than the control cell (Fig. 4(b), due to a). extra carriers generated by the fluorescence phenomenon of corresponding QDs and b). matching VB edge properties of utilized QDs with the bulk perovskite. This happens to be the reason for the improved current density and FF for cells with an active layer of CsPbX₃ QDs. However, a slight decrement in V_{oc} with the addition of QD layer can be attributed to the recombination due to the generated extra charge carriers. The generation of fluorescence by QDs within the device can be verified from the raised shoulder in the IPCE curve along 420 – 600 nm, 700-780 nm for CsPbBr₃ and CsPbI₃ based tandem PSCs . As shown in Fig. 2(b), the VB edge of CsPbBr₃ (-5.56 eV), (without considering the quantum size effect) appears to be much lower than the VB edge of bulk perovskite (-5.43 eV). However, according to the measured absorption characteristics, J-V and IPCE curves, there is a clear indication that the VB edge of the CsPbBr₃ QD (with quantum size effect) is closer to band edge of the bulk perovskite for better charge extraction and hence improved PCE when compared to the control cell. (Note: VB edge properties are not measured due to limited lab facilities).

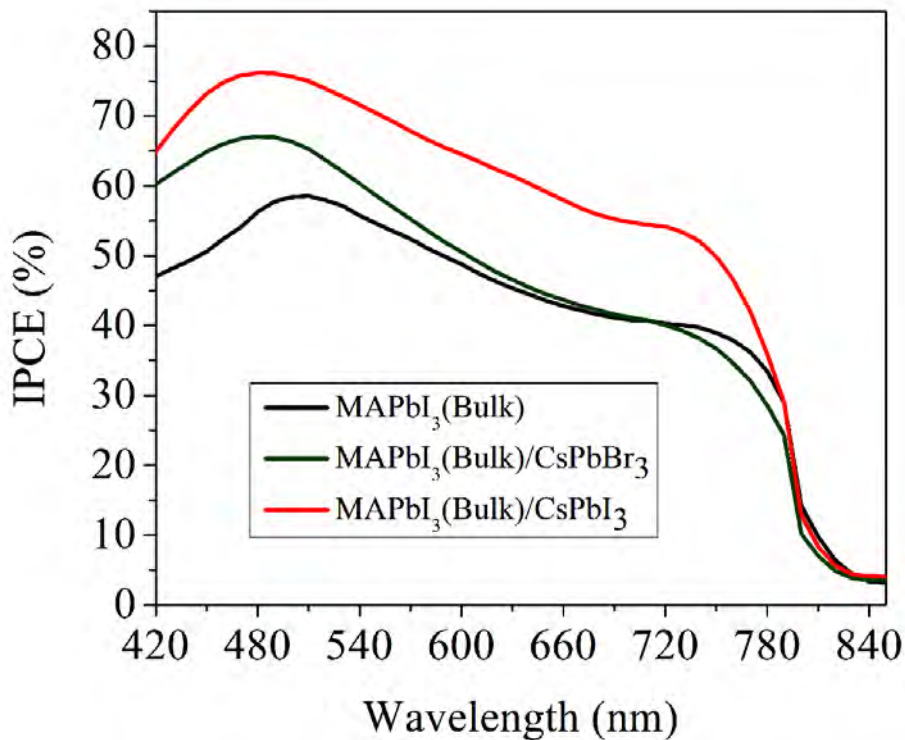


Figure 5.9. IPCE curves for MAPbI₃ perovskite solar cells in bulk, and add the CsPbBr₃ and CsPbI₃ perovskite quantum dots.

5.3.3 Light emitting diodes

The high color purity obtained by PQDs make this material very promising for light emitting diodes. These PQDs have high photoluminescence quantum yield (80%) and are an attractive material in electroluminescent (EL) devices. One problem with these devices is the fabrication of the films

The structure of the PQDs based LEDs device is: Indium Tin Oxide (ITO)/Poly (ethylenedioxythiophene) (PEDOT-PSS)/(Poly(9-vinylcarbazole (PVK)/PQDs/Al see Figure 7-10, where ITO is the contact, PEDOT-PSS is a hole conductor material with a thickness of 20 nm, PVK is an electron blocking layer, thickness of 20 nm, PQDs is a emission material and Al is contact. The energy band diagram of the PQDs-LEDs is show in figure 5-10.

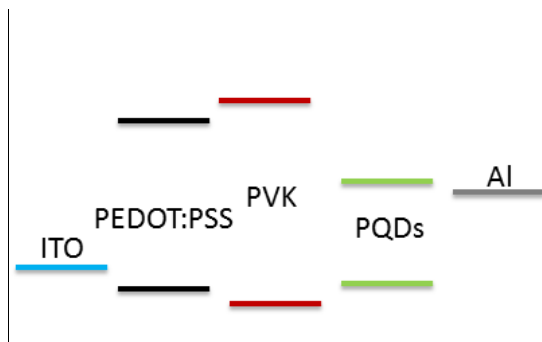


Figure 5-10. Structure of the PQDs-LEDs device and energy levels diagram.

The fabrication of the device has several problems which include the films fabrication, the diluted suspension used in a common spin coating, and problems with solvents. The first problem in our case is that the PQDs are dissolved in toluene and the PVK again is dissolved in toluene and modify the PVK layer when the perovskite is deposited; however, this problem is resolved using other solvent in the synthesis. It is necessary to optimize the film thickness in each layer. Figure 5-11 depicts the current density-voltage curve of the MAPBBBr₃ QDs-LEDs, revealing a turn on voltage of 9V, increasing the voltage increases the luminance.

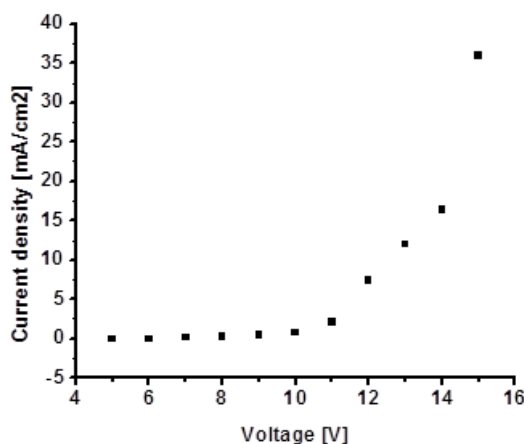


Figure 5-11 Current density-voltage curve of the MAPBBBr₃ PQDs-LEDs.

A narrow electroluminescence (EL) spectrum was observed for QDs-LEDs as shown in Figure 5-12. The emission of the QDs-LEDs corresponds to the emission peak of the colloidal QDs (515 nm). The emission peak is increased when

the voltage is increased. However for 15 V, the signal is less due to degradation of the layers in the device.

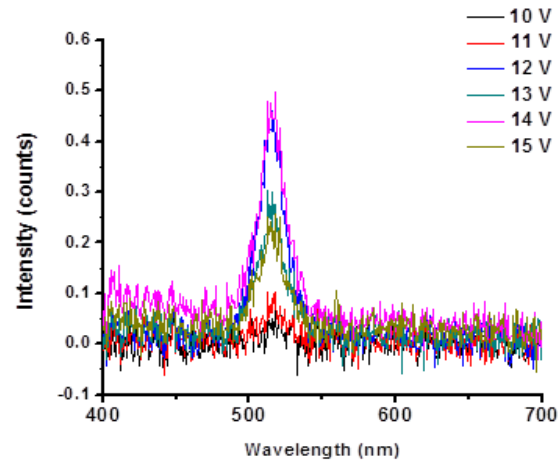


Figure 5-12. Electroluminescence spectrum for PQDs-LEDs

Figure 5-13 presents a picture of the QDs-LEDs showing that it is possible to obtain a QDs LEDs with this type of material.

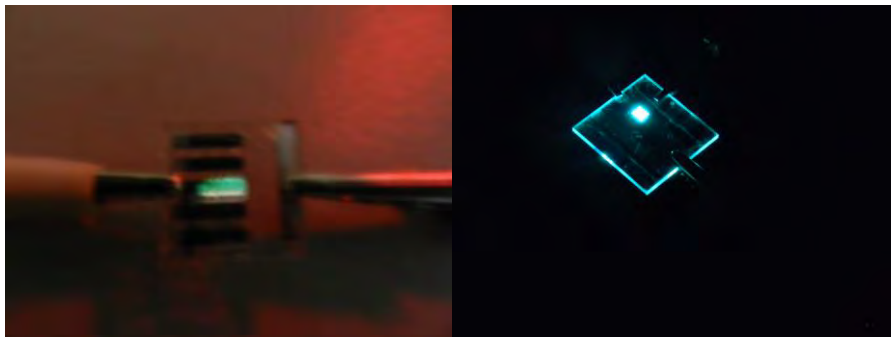


Figure 5.14 Picture of the PQDs-LEDs.

Chapter 6

Conclusions

Recently, there has been substantial interest in the visible and infrared absorption to determine the functionality of QDs due to their potential applications in solar cells and light emitting diode technology. In the present investigation, the author characterized various QDs in solar cells and LEDs.

The configuration $\text{TiO}_2/\text{CdS}/\text{CdSe}/\text{ZnS}$ with absorption of the QDs in the visible was used to study the effect of different sensitization methods of deposition such as SILAR, electrophoresis or pipetting and their impact on the PCE. The PCE of TiO_2/CdS sensitized with CdSe deposited by electrophoresis or pipetting presented a significant change of up to 4.0% and the combination of both methods enhanced the PCE upto 4.6%. J-V curves and impedance analysis indicated that the photocurrent ($13.1 \text{ mA}/\text{cm}^2$) and FF were responsible of the efficiency improvement due to the reduction of the transport resistance.

The near infrared absorption light was analyzed using different configurations. The first configuration was with PFN incorporated into the active layer of $\text{TiO}_2/\text{PbS}/\text{PFN}/\text{CdS}/\text{ZnS}$. Three main effects were observed: 1) A modification of the surface morphology by using PFN that enhanced the light absorption by light scattering. 2) The enhancement of the charge transport, resulting in an increment of J_{sc} . 3) PFN provides a protecting layer which reduces the recombination between QDs and polysulfide electrolyte. From the results of these investigations, it is concluded that the introduction of organic electron transport layers after TiO_2 could be useful to improve cell efficiency up to 3.6% in QDSSC.

With the $\text{TiO}_2/\text{CdS}/\text{Bi}_2\text{S}_3/\text{ZnS}$ configuration, the PCE, FF and photocurrent were found to be 2.52%, 53% and $9.3 \text{ mA}/\text{cm}^2$, respectively. These parameters were explained by the increment of absorption and shift towards the near infrared region along with favorable energy level arrangement. The low toxicity of Bi_2S_3 can enhance the photovoltaic properties of QDSSCs, which plays a similar role as PbS for other architectures.

The incorporation of CdSeTe QDs in the configuration $\text{TiO}_2/\text{CdS}/\text{CdSe}$ can increase the absorption upto 800 nm, it was shown that the CdS QDs interfaces between TiO_2 and CdSeTe QDs improved the PCE. The effect of multiple QDs on QDSSCs, using colloidal CdSe QRs and CdSeTe QDs with SILAR CdS QDs, to improve the PCE has been studied successfully. For the multiple QDs, the maximum PCE was found to be 6.5% in $\text{TiO}_2/\text{CdS}/\text{CdSe}/\text{CdSeTe}$ QDSSC. The maximum increment in the PCE of up to 7.4% due to an increment of the resistance recombination has been observed by utilization of a SiO_2 layer. J-V curves indicated that the higher efficiency was mainly due to the increase of photocurrent originated by the broadening of the absorption spectra as shown by IPCE measurements. The use of CdSeTe QDs allows the harvesting of NIR photons while the use of CdSe QRs avoids the reduction of absorbance in the visible region. The above results open a new window in QDSSCs by using different colloidal QDs to boost the cell efficiency.

In perovskite solar cells is make a device with 8% in photonconversion efficiency, showing that is necessary have a good grown grain in the perovskite films. The grown of the perovskite is increased with the use of anti-solvent material; this material increase the grown of the films and increase the photoconversion efficiency in the cell.

The use of perovskite quantum dots in the perovskite solar cells increase the efficiency until 11.5%, due to the engineering interfaces between perovskite bulk and hole transport material (spiro-ometad). This new type of quantum dots present high photoluminescence quantum yield of 80% and have interesting properties in light emitting diodes applications.

Publications

1. **Esparza, D.**, Zarazúa, I., López-Luke, T., Cerdán-Pasarán, A., Sánchez-Solís, A., Torres-Castro, A., De la Rosa, E. (2015). *Effect of Different Sensitization Technique on the Photoconversion Efficiency of CdS Quantum Dot and CdSe Quantum Rod Sensitized TiO₂ Solar Cells*. The Journal of Physical Chemistry C, 119(24), 13394-13403.
2. **Esparza, D.**, Zarazúa, I., López-Luke, T., Carriles R., Torres-Castro, A., De la Rosa, E. (2015). *Photovoltaic Properties of Bi₂S₃ and CdS Quntum Dots Sensitized Solar Cells*. Electrochimica Acta, 180, 486-492.
3. **Esparza, D.**, Oliva, J., López-Luke, T., Carriles, R., Zarazúa, I., De la Rosa, E. (2015). *Current improvement in hybrid quantum dot sensitized solar cells by increased light-scattering with a polymer layer*. RSC Advances, 5(45), 36140-36148.
4. Cerdán-Pasarán, A., López-Luke, T., **Esparza, D.**, Zarazúa, I., De la Rosa, E., Fuentes-Ramírez, R., Zhang, J. Z. (2015). *Photovoltaic properties of multilayered quantum dot/quantum rod-sensitized TiO₂ solar cells fabricated by SILAR and electrophoresis*. Physical Chemistry Chemical Physics, 17(28), 18590-18599.
5. Zarazúa, I., **Esparza, D.**, López-Luke, T., Ceja-Fdez, A., Reyes-Gomez, J., Mora-Seró, I., De la Rosa, E. (2015). *Effect of the electrophoretic deposition of Au NPs in the performance CdS QDs sensitized solar Cells*. Electrochimica Acta.
6. Cerdán- Pasaran, A., **Esparza, D.**, Zarazúa, I., Resendez, M., López-Luke, T., De la Rosa, E., Fuentes-Ramirez, R., Alatorre Ordaz, A., Martinez-Benitez, A. (2016). *Photovoltaic Study of Quantum Dot Sensitized TiO₂/CdS/ZnS Solar Cell with P3HT or P3OT added*. Journal of applied electrochemistry.
7. **Esparza, D.**, Oliva, J., López-Luke, T., Torres-Castro, A., Zarazúa, I., De la Rosa, E. (2014). *Effect of PFN in Hybrid Quantum Dots Solar Cells*. Latin America Optics and Photonics Conference (LAOP) OSA Conference paper LTh4A.39.

8. Martínez, A., Zarazua, I., **Esparza, D.**, Cerdan, A., López-Luke, T., De la Rosa, E. (2014). *Quantum Dots Solar Cells of CdS Deposited by Chemical Bath Method*, Latin America Optics and Photonics Conference (LAOP) OSA Conference paper LTh4A.37.
9. **Esparza, D.**, Oliva, J., López-Luke, T., Cerdán-Pasarán, A., ... & De la Rosa, E. (2016). *Improvement the Photoconversion Efficiency of Quantum Dots Sensitized TiO₂ Solar Cells by Tuning the Absorption with Multiple Quantum Dots*. In process.
10. Ramachari, D., **Esparza, D.**, Lopez Luke, T., Romero, V. H., Perez-Mayen, L., De la Rosa, E. and Jayasankar, C.K. (2016). *Synthesis of Co-doped Yb³⁺ -Er³⁺:ZrO₂ Upconversion Nanoparticles and Their Applications in Enhanced Photovoltaic properties of Quantum Dot Sensitized Solar Cells*. Submitted.
11. **Esparza, D.**, Bustos, G., Lopez-Luke, T., Zarazua, I., Martinez, A., De la Rosa E. (2016) *High performance of CdS interfaces in CdSeTe Gradient Quantum Dots Sensitized Solar Cells*. Submitted.
12. Sidhik, S, **Esparza D**, Lopez-Luke, T. De la Rosa, E, (2016) *Effect of nonpolar solvent deposition time and Co(III) complex doping on the performance of mesoscopic-perovskite based solar cells*. Submitted.
13. Sidhik, S, **Esparza D**, Lopez-Luke, T. De la Rosa, E, (2016) *perovskite quantum dots solar cells*. In process

References

1. Dresselhaus, M. and I. Thomas, *Alternative energy technologies*. Nature, 2001. **414**(6861): p. 332-337.
2. Kamat, P.V., *Meeting the clean energy demand: nanostructure architectures for solar energy conversion*. The Journal of Physical Chemistry C, 2007. **111**(7): p. 2834-2860.
3. Eisenberg, R. and D.G. Nocera, *Preface: Overview of the forum on solar and renewable energy*. Inorganic chemistry, 2005. **44**(20): p. 6799-6801.
4. Lior, N., *Energy resources and use: The present situation and possible paths to the future*. Energy, 2008. **33**(6): p. 842-857.
5. Chapin, D.M., C. Fuller, and G. Pearson, *A new silicon p-n junction photocell for converting solar radiation into electrical power*. Journal of Applied Physics, 1954. **25**(5): p. 676-677.
6. Green, M.A., et al., *Solar cell efficiency tables (Version 45)*. Progress in photovoltaics: research and applications, 2015. **23**(1): p. 1-9.
7. O'Regan, B. and M. Gratzel, *A low-cost, high-efficiency solar cell based on dye-sensitized colloidal TiO₂ films*. Nature, 1991. **353**(6346): p. 737-740.
8. Soga, T., *Nanostructured materials for solar energy conversion*. 2006: Elsevier.
9. Gregg, B.A., *Excitonic solar cells*. The Journal of Physical Chemistry B, 2003. **107**(20): p. 4688-4698.
10. Lokhande, C., et al., *Electrodeposition of TiO₂ and RuO₂ thin films for morphology-dependent applications*. Ultramicroscopy, 2005. **105**(1): p. 267-274.
11. Saunders, B.R. and M.L. Turner, *Nanoparticle-polymer photovoltaic cells*. Advances in colloid and interface science, 2008. **138**(1): p. 1-23.
12. Scharber, M.C., et al., *Design rules for donors in bulk-heterojunction solar cells—Towards 10% energy-conversion efficiency*. Advanced Materials, 2006. **18**(6): p. 789-794.
13. Brabec, C.J., et al., *Origin of the open circuit voltage of plastic solar cells*. Advanced Functional Materials, 2001. **11**(5): p. 374-380.
14. Ma, W., et al., *Thermally stable, efficient polymer solar cells with nanoscale control of the interpenetrating network morphology*. Advanced Functional Materials, 2005. **15**(10): p. 1617-1622.
15. Robel, I., et al., *Quantum Dot Solar Cells. Harvesting Light Energy with CdSe Nanocrystals Molecularly Linked to Mesoscopic TiO₂ Films*. Journal of the American Chemical Society, 2006. **128**(7): p. 2385-2393.
16. Kamat, P.V., *Quantum dot solar cells. Semiconductor nanocrystals as light harvesters†*. The Journal of Physical Chemistry C, 2008. **112**(48): p. 18737-18753.
17. Lopez-Luke, T., et al., *Nitrogen-doped and CdSe quantum-dot-sensitized nanocrystalline TiO₂ films for solar energy conversion applications*. The Journal of Physical Chemistry C, 2008. **112**(4): p. 1282-1292.
18. Goh, C., S.R. Scully, and M.D. McGehee, *Effects of molecular interface modification in hybrid organic-inorganic photovoltaic cells*. Journal of Applied Physics, 2007. **101**(11): p. 114503-114503.
19. van Hal, P.A., et al., *TiO₂ sensitized with an oligo (p-phenylenevinylene) carboxylic acid: a new model compound for a hybrid solar cell*. Journal of Materials Chemistry, 2003. **13**(5): p. 1054-1057.
20. Giordano, F., et al., *Enhanced electronic properties in mesoporous TiO₂ via lithium doping for high-efficiency perovskite solar cells*. Nature communications, 2016. **7**.

21. Saliba, M., et al., *Cesium-containing triple cation perovskite solar cells: improved stability, reproducibility and high efficiency*. Energy & Environmental Science, 2016. **9**(6): p. 1989-1997.
22. Jacobsson, T.J., et al., *Exploration of the compositional space for mixed lead halogen perovskites for high efficiency solar cells*. Energy & Environmental Science, 2016. **9**(5): p. 1706-1724.
23. Grätzel, M., *Dye-sensitized solar cells*. Journal of Photochemistry and Photobiology C: Photochemistry Reviews, 2003. **4**(2): p. 145-153.
24. O'regan, B. and M. Grätzel, *A low-cost, high-efficiency solar cell based on dye-sensitized. nature*, 1991. **353**: p. 737-740.
25. Chiba, Y., et al., *Dye-sensitized solar cells with conversion efficiency of 11.1%*. Japanese Journal of Applied Physics, 2006. **45**(7L): p. L638.
26. Grätzel, M., *Conversion of sunlight to electric power by nanocrystalline dye-sensitized solar cells*. Journal of Photochemistry and Photobiology A: Chemistry, 2004. **164**(1): p. 3-14.
27. Wang, X., L. Zhi, and K. Müllen, *Transparent, conductive graphene electrodes for dye-sensitized solar cells*. Nano letters, 2008. **8**(1): p. 323-327.
28. Horiuchi, T., et al., *High efficiency of dye-sensitized solar cells based on metal-free indoline dyes*. Journal of the American Chemical Society, 2004. **126**(39): p. 12218-12219.
29. Yella, A., et al., *Porphyrin-sensitized solar cells with cobalt (II/III)-based redox electrolyte exceed 12 percent efficiency*. science, 2011. **334**(6056): p. 629-634.
30. Mathew, S., et al., *Dye-sensitized solar cells with 13% efficiency achieved through the molecular engineering of porphyrin sensitizers*. Nat Chem, 2014. **6**(3): p. 242-247.
31. Kamat, P.V., *Meeting the Clean Energy Demand: Nanostructure Architectures for Solar Energy Conversion*. The Journal of Physical Chemistry C, 2007. **111**(7): p. 2834-2860.
32. Yong, K.T., et al., *Biocompatible Near-Infrared Quantum Dots as Ultrasensitive Probes for Long-Term in vivo Imaging Applications*. Small, 2009. **5**(17): p. 1997-2004.
33. Ceja-Fdez, A., et al., *Labeling of HeLa cells using ZrO₂: Yb³⁺-Er³⁺ nanoparticles with upconversion emission*. Journal of biomedical optics, 2015. **20**(4): p. 046006-046006.
34. Anikeeva, P.O., et al., *Quantum dot light-emitting devices with electroluminescence tunable over the entire visible spectrum*. Nano letters, 2009. **9**(7): p. 2532-2536.
35. Sanchez, R.S., et al., *Tunable light emission by exciplex state formation between hybrid halide perovskite and core/shell quantum dots: Implications in advanced LEDs and photovoltaics*. Science Advances, 2016. **2**(1): p. e1501104.
36. Dong, C., X. Li, and J. Qi, *First-Principles Investigation on Electronic Properties of Quantum Dot-Sensitized Solar Cells Based on Anatase TiO₂ Nanotubes*. The Journal of Physical Chemistry C, 2011. **115**(41): p. 20307-20315.
37. Cerdán-Pasarán, A., et al., *Photovoltaic properties of multilayered quantum dot/quantum rod-sensitized TiO₂ solar cells fabricated by SILAR and electrophoresis*. Physical Chemistry Chemical Physics, 2015. **17**(28): p. 18590-18599.
38. Kongkanand, A., et al., *Quantum dot solar cells. Tuning photoresponse through size and shape control of CdSe-TiO₂ architecture*. Journal of the American Chemical Society, 2008. **130**(12): p. 4007-4015.
39. Mor, G.K., et al., *Use of highly-ordered TiO₂ nanotube arrays in dye-sensitized solar cells*. Nano letters, 2006. **6**(2): p. 215-218.
40. Hanna, M.C. and A.J. Nozik, *Solar conversion efficiency of photovoltaic and photoelectrolysis cells with carrier multiplication absorbers*. Journal of Applied Physics, 2006. **100**(7): p. 074510.

41. Du, J., et al., *Zn–Cu–In–Se Quantum Dot Solar Cells with a Certified Power Conversion Efficiency of 11.6%*. Journal of the American Chemical Society, 2016. **138**(12): p. 4201-4209.
42. Ren, Z., et al., *Effects of Metal Oxyhydroxide Coatings on Photoanode in Quantum Dot Sensitized Solar Cells*. Chemistry of Materials, 2016. **28**(7): p. 2323-2330.
43. Ren, Z., et al., *Amorphous TiO₂ Buffer Layer Boosts Efficiency of Quantum Dot Sensitized Solar Cells to over 9%*. Chemistry of Materials, 2015. **27**(24): p. 8398-8405.
44. Hardin, B.E., H.J. Snaith, and M.D. McGehee, *The renaissance of dye-sensitized solar cells*. Nature Photonics, 2012. **6**(3): p. 162-169.
45. Hanna, M. and A. Nozik, *Solar conversion efficiency of photovoltaic and photoelectrolysis cells with carrier multiplication absorbers*. Journal of Applied Physics, 2006. **100**(7): p. 074510.
46. Schrödinger, E., *An undulatory theory of the mechanics of atoms and molecules*. Physical Review, 1926. **28**(6): p. 1049.
47. Sun, Q., et al., *Bright, multicoloured light-emitting diodes based on quantum dots*. Nature Photonics, 2007. **1**(12): p. 717-722.
48. Caruge, J., et al., *Colloidal quantum-dot light-emitting diodes with metal-oxide charge transport layers*. Nature Photonics, 2008. **2**(4): p. 247-250.
49. Sapsford, K.E., et al., *Biosensing with luminescent semiconductor quantum dots*. Sensors, 2006. **6**(8): p. 925-953.
50. Chan, W.C., et al., *Luminescent quantum dots for multiplexed biological detection and imaging*. Current opinion in biotechnology, 2002. **13**(1): p. 40-46.
51. Rühle, S., M. Shalom, and A. Zaban, *Quantum-dot-sensitized solar cells*. ChemPhysChem, 2010. **11**(11): p. 2290-2304.
52. Nozik, A., *Quantum dot solar cells*. Physica E: Low-dimensional Systems and Nanostructures, 2002. **14**(1): p. 115-120.
53. Hod, I. and A. Zaban, *Materials and Interfaces in Quantum Dot Sensitized Solar Cells: Challenges, Advances and Prospects*. Langmuir, 2014. **30**(25): p. 7264-7273.
54. Lee, H.J., et al., *Regenerative PbS and CdS quantum dot sensitized solar cells with a cobalt complex as hole mediator*. Langmuir, 2009. **25**(13): p. 7602-7608.
55. Franceschetti, A., J. An, and A. Zunger, *Impact ionization can explain carrier multiplication in PbSe quantum dots*. Nano letters, 2006. **6**(10): p. 2191-2195.
56. Lee, H.J., et al., *Multilayered Semiconductor (CdS/CdSe/ZnS)-Sensitized TiO₂ Mesoporous Solar Cells: All Prepared by Successive Ionic Layer Adsorption and Reaction Processes*. Chemistry of Materials, 2010. **22**(19): p. 5636-5643.
57. Mora-Seró, I., et al., *Large improvement of electron extraction from CdSe quantum dots into a TiO₂ thin layer by N3 dye coabsorption*. Thin Solid Films, 2008. **516**(20): p. 6994-6998.
58. Zeng, T.-W., et al., *Effects of bifunctional linker on the performance of P3HT/CdSe quantum dot-linker-ZnO nanocolumn photovoltaic device*. Optics express, 2010. **18**(103): p. A357-A365.
59. Ellingson, R.J., et al., *Highly efficient multiple exciton generation in colloidal PbSe and PbS quantum dots*. Nano letters, 2005. **5**(5): p. 865-871.
60. Parsi Benekohal, N., et al., *Colloidal PbS and PbSeS Quantum Dot Sensitized Solar Cells Prepared by Electrophoretic Deposition*. The Journal of Physical Chemistry C, 2012. **116**(31): p. 16391-16397.

61. Lv, P., et al., *Simple synthesis method of Bi₂S₃/CdS quantum dots cosensitized TiO₂ nanotubes array with enhanced photoelectrochemical and photocatalytic activity*. CrystEngComm, 2013. **15**(37): p. 7548-7555.
62. Ma, Y., H. Li, and J. Yuan, *In-situ solution chemical reaction deposition of Bi₂S₃ quantum dots on mesoscopic TiO₂ films for application in quantum-dot-sensitized solar cells*. Integrated Ferroelectrics, 2016. **169**(1): p. 42-49.
63. Esparza, D., et al., *Effect of Different Sensitization Technique on the Photoconversion Efficiency of CdS Quantum Dot and CdSe Quantum Rod Sensitized TiO₂ Solar Cells*. The Journal of Physical Chemistry C, 2015. **119**(24): p. 13394-13403.
64. Lee, Y.L. and Y.S. Lo, *Highly Efficient Quantum-Dot-Sensitized Solar Cell Based on Co-Sensitization of CdS/CdSe*. Advanced Functional Materials, 2009. **19**(4): p. 604-609.
65. Pawar, S.A., et al., *Quantum dot sensitized solar cell based on TiO₂/CdS/CdSe/ZnS heterostructure*. Electrochimica Acta, 2016. **203**: p. 74-83.
66. Huang, F., et al., *Doubling the power conversion efficiency in CdS/CdSe quantum dot sensitized solar cells with a ZnSe passivation layer*. Nano Energy, 2016. **26**: p. 114-122.
67. Lin, Y., et al., *CdS/CdSe co-sensitized SnO₂ photoelectrodes for quantum dots sensitized solar cells*. Optics Communications, 2015. **346**: p. 64-68.
68. Li, W., et al., *Fabrication of CdSe/CdTe Quantum Dots Co-Sensitized TiO₂ Nanorods by Electrochemical Atomic Layer Deposition Method*. Journal of The Electrochemical Society, 2015. **162**(4): p. D137-D141.
69. Maity, P., et al., *Cascading electron and hole transfer dynamics in a CdS/CdTe core-shell sensitized with bromo-pyrogallol red (Br-PGR): slow charge recombination in type II regime*. Nanoscale, 2015. **7**(6): p. 2698-2707.
70. Luo, S., et al., *Improved charge separation and transport efficiency in panchromatic-sensitized solar cells with co-sensitization of PbS/CdS/ZnS quantum dots and dye molecules*. RSC Advances, 2016. **6**(25): p. 21156-21164.
71. Esparza, D., et al., *Current improvement in hybrid quantum dot sensitized solar cells by increased light-scattering with a polymer layer*. RSC Advances, 2015. **5**(45): p. 36140-36148.
72. Braga, A., et al., *Panchromatic sensitized solar cells based on metal sulfide quantum dots grown directly on nanostructured TiO₂ electrodes*. The Journal of Physical Chemistry Letters, 2011. **2**(5): p. 454-460.
73. Song, X., et al., *One-Step Preparation and Assembly of Aqueous Colloidal CdS x Se_{1-x} Nanocrystals within Mesoporous TiO₂ Films for Quantum Dot-Sensitized Solar Cells*. ACS applied materials & interfaces, 2013. **5**(11): p. 5139-5148.
74. Yang, G., et al., *Probing Exciton Move and Localization in Solution-Grown Colloidal CdSe x S_{1-x} Alloyed Nanowires by Temperature-and Time-Resolved Spectroscopy*. The Journal of Physical Chemistry C, 2015. **119**(39): p. 22709-22717.
75. Pan, Z., et al., *Near Infrared Absorption of CdSe_xTe_{1-x} Alloyed Quantum Dot Sensitized Solar Cells with More than 6% Efficiency and High Stability*. ACS Nano, 2013. **7**(6): p. 5215-5222.
76. Huang, H., et al., *Emulsion Synthesis of Size-Tunable CH₃NH₃PbBr₃ Quantum Dots: An Alternative Route toward Efficient Light-Emitting Diodes*. ACS Applied Materials & Interfaces, 2015. **7**(51): p. 28128-28133.
77. Wei, H., et al., *Investigation on Interfacial Charge Transfer Process in CdSe x Te_{1-x} Alloyed Quantum Dot Sensitized Solar Cells*. Electrochimica Acta, 2015. **173**: p. 156-163.
78. Pan, Z., et al., *Highly efficient inverted type-I CdS/CdSe core/shell structure QD-sensitized solar cells*. ACS nano, 2012. **6**(5): p. 3982-3991.

79. Dworak, L., et al., *Ultrafast charge separation at the CdSe/CdS core/shell quantum dot/methylviologen interface: Implications for nanocrystal solar cells*. The Journal of Physical Chemistry C, 2011. **115**(10): p. 3949-3955.
80. Zare, H., et al., *High-efficiency CdTe/CdS core/shell nanocrystals in water enabled by photo-induced colloidal hetero-epitaxy of CdS shelling at room temperature*. Nano Research, 2015. **8**(7): p. 2317-2328.
81. Jiao, S., et al., *Band Engineering in Core/Shell ZnTe/CdSe for Photovoltage and Efficiency Enhancement in Exciplex Quantum Dot Sensitized Solar Cells*. ACS Nano, 2015. **9**(1): p. 908-915.
82. Jin, S., et al., *Ultrafast Charge Separation from Highly Reductive ZnTe/CdSe Type II Quantum Dots*. The Journal of Physical Chemistry Letters, 2012. **3**(15): p. 2052-2058.
83. Jiang, Z.-J. and D.F. Kelley, *Stranski–Krastanov Shell Growth in ZnTe/CdSe Core/Shell Nanocrystals*. The Journal of Physical Chemistry C, 2013. **117**(13): p. 6826-6834.
84. Yang, J., et al., *CdSeTe/CdS Type-I Core/Shell Quantum Dot Sensitized Solar Cells with Efficiency over 9%*. The Journal of Physical Chemistry C, 2015. **119**(52): p. 28800-28808.
85. Fan, G.-C., et al., *Enhanced Photoelectrochemical Immunosensing Platform Based on CdSeTe@ CdS: Mn Core–Shell Quantum Dots-Sensitized TiO₂ Amplified by CuS Nanocrystals Conjugated Signal Antibodies*. Analytical chemistry, 2016. **88**(6): p. 3392-3399.
86. Zhou, S., et al., *CdSeTe@ CdS@ ZnS Quantum-Dot-Sensitized Macroporous TiO₂ Film: A Multisignal-Amplified Photoelectrochemical Platform*. ChemPhysChem, 2015. **16**(13): p. 2826-2835.
87. Hod, I., et al., *Dye versus Quantum Dots in Sensitized Solar Cells: Participation of Quantum Dot Absorber in the Recombination Process*. The Journal of Physical Chemistry Letters, 2011. **2**(24): p. 3032-3035.
88. González-Pedro, V., et al., *Modeling High-Efficiency Quantum Dot Sensitized Solar Cells*. ACS Nano, 2010. **4**(10): p. 5783-5790.
89. Mora-Sero, I., et al., *Recombination in quantum dot sensitized solar cells*. Accounts of chemical research, 2009. **42**(11): p. 1848-1857.
90. Chen, C.-Y., et al., *Highly efficient light-harvesting ruthenium sensitizer for thin-film dye-sensitized solar cells*. ACS nano, 2009. **3**(10): p. 3103-3109.
91. Nazeeruddin, M.K., et al., *Engineering of efficient panchromatic sensitizers for nanocrystalline TiO₂-based solar cells*. Journal of the American Chemical Society, 2001. **123**(8): p. 1613-1624.
92. Hod, I. and A. Zaban, *Materials and interfaces in quantum dot sensitized solar cells: Challenges, advances and prospects*. Langmuir, 2013. **30**(25): p. 7264-7273.
93. CdS, C., *CdSe quantum dot-sensitized solar cell employing TiO₂ nanotube working-electrode and Cu₂S counter-electrode*. Applied Physics Letters, 2010. **97**: p. 123107.
94. Radich, J.G., R. Dwyer, and P.V. Kamat, *Cu₂S Reduced Graphene Oxide Composite for High-Efficiency Quantum Dot Solar Cells. Overcoming the Redox Limitations of S²⁻/S^{n 2-}-at the Counter Electrode*. The Journal of Physical Chemistry Letters, 2011. **2**(19): p. 2453-2460.
95. Jiang, Y., et al., *ITO@ Cu₂S tunnel junction nanowire arrays as efficient counter electrode for quantum-dot-sensitized solar cells*. Nano letters, 2013. **14**(1): p. 365-372.
96. Xu, J., et al., *Cu₂ZnSnS₄ hierarchical microspheres as an effective counter electrode material for quantum dot sensitized solar cells*. The Journal of Physical Chemistry C, 2012. **116**(37): p. 19718-19723.
97. Yang, Z., et al., *Electrocatalytic sulfur electrodes for CdS/CdSe quantum dot-sensitized solar cells*. Chemical Communications, 2010. **46**(30): p. 5485-5487.

98. Yang, Z., et al., *Quantum dot-sensitized solar cells featuring CuS/CoS electrodes provide 4.1% efficiency*. Advanced Energy Materials, 2011. **1**(2): p. 259-264.
99. Fan, S.-Q., et al., *Hierarchical nanostructured spherical carbon with hollow core/mesoporous shell as a highly efficient counter electrode in CdSe quantum-dot-sensitized solar cells*. Applied Physics Letters, 2010. **96**(6): p. 063501.
100. Sudhagar, P., et al., *Robust mesocellular carbon foam counter electrode for quantum-dot sensitized solar cells*. Electrochemistry Communications, 2011. **13**(1): p. 34-37.
101. Kim, H.-J., et al., *Highly efficient solution processed nanorice structured NiS counter electrode for quantum dot sensitized solar cells*. Electrochimica Acta, 2014. **127**: p. 427-432.
102. Tachan, Z., et al., *PbS as a highly catalytic counter electrode for polysulfide-based quantum dot solar cells*. The Journal of Physical Chemistry C, 2011. **115**(13): p. 6162-6166.
103. Lin, C.-Y., et al., *Photoactive p-type PbS as a counter electrode for quantum dot-sensitized solar cells*. Journal of Materials Chemistry A, 2013. **1**(4): p. 1155-1162.
104. Yu, H., et al., *Topotactically grown bismuth sulfide network film on substrate as low-cost counter electrodes for quantum dot-sensitized solar cells*. The Journal of Physical Chemistry C, 2014. **118**(30): p. 16602-16610.
105. Qu, L., Z.A. Peng, and X. Peng, *Alternative routes toward high quality CdSe nanocrystals*. Nano Letters, 2001. **1**(6): p. 333-337.
106. Wang, Z., *Transmission electron microscopy of shape-controlled nanocrystals and their assemblies*. The Journal of Physical Chemistry B, 2000. **104**(6): p. 1153-1175.
107. Singh, S., et al., *Luminescent behavior of cadmium sulfide quantum dots for gallic acid estimation*. Nanotechnology, 2013. **24**(11): p. 115602.
108. Empedocles, S.A., D. Norris, and M. Bawendi, *Photoluminescence spectroscopy of single CdSe nanocrystallite quantum dots*. Physical Review Letters, 1996. **77**(18): p. 3873.
109. Nelson, J., *The physics of solar cells*. Vol. 1. 2003: World Scientific.
110. Wright, M. and A. Uddin, *Organic-inorganic hybrid solar cells: A comparative review*. Solar energy materials and solar cells, 2012. **107**: p. 87-111.
111. Kongkanand, A., et al., *Quantum Dot Solar Cells. Tuning Photoresponse through Size and Shape Control of CdSe-TiO₂ Architecture*. Journal of the American Chemical Society, 2008. **130**(12): p. 4007-4015.
112. Guo, X.-Z., et al., *Study on the effect of measuring methods on incident photon-to-electron conversion efficiency of dye-sensitized solar cells by home-made setup*. Review of scientific instruments, 2010. **81**(10): p. 103106.
113. Fabregat-Santiago, F., et al., *Decoupling of Transport, Charge Storage, and Interfacial Charge Transfer in the Nanocrystalline TiO₂/Electrolyte System by Impedance Methods*. The Journal of Physical Chemistry B, 2002. **106**(2): p. 334-339.
114. Fabregat-Santiago, F., et al., *Influence of electrolyte in transport and recombination in dye-sensitized solar cells studied by impedance spectroscopy*. Solar Energy Materials and Solar Cells, 2005. **87**(1): p. 117-131.
115. He, C., et al., *Electrochemical impedance spectroscopy characterization of electron transport and recombination in ZnO nanorod dye-sensitized solar cells*. The Journal of Physical Chemistry C, 2009. **113**(24): p. 10322-10325.
116. Mora-Seró, I., et al., *Recombination rates in heterojunction silicon solar cells analyzed by impedance spectroscopy at forward bias and under illumination*. Solar Energy Materials and Solar Cells, 2008. **92**(4): p. 505-509.
117. De Jongh, P. and D. Vanmaekelbergh, *Trap-Limited Electronic Transport in Assemblies of Nanometer-Size TiO₂ Particles*. Physical review letters, 1996. **77**(16): p. 3427.

118. Van de Lagemaat, J. and A. Frank, *Effect of the surface-state distribution on electron transport in dye-sensitized TiO₂ solar cells: Nonlinear electron-transport kinetics*. The Journal of Physical Chemistry B, 2000. **104**(18): p. 4292-4294.
119. Chakrapani, V., D. Baker, and P.V. Kamat, *Understanding the Role of the Sulfide Redox Couple (S²⁻/Sⁿ⁻²⁻) in Quantum Dot-Sensitized Solar Cells*. Journal of the American Chemical Society, 2011. **133**(24): p. 9607-9615.
120. Franco, G., et al., *Frequency-Resolved Optical Detection of Photoinjected Electrons in Dye-Sensitized Nanocrystalline Photovoltaic Cells*. The Journal of Physical Chemistry B, 1999. **103**(4): p. 692-698.
121. Fabregat-Santiago, F., et al., *Characterization of nanostructured hybrid and organic solar cells by impedance spectroscopy*. Phys Chem Chem Phys, 2011. **13**(20): p. 9083-118.
122. Barea, E.M., et al., *Design of injection and recombination in quantum dot sensitized solar cells*. Journal of the American Chemical Society, 2010. **132**(19): p. 6834-6839.
123. Braga, A., et al., *Panchromatic Sensitized Solar Cells Based on Metal Sulfide Quantum Dots Grown Directly on Nanostructured TiO₂ Electrodes*. The Journal of Physical Chemistry Letters, 2011. **2**(5): p. 454-460.
124. Bisquert, J. and I. Mora-Seró, *Simulation of steady-state characteristics of dye-sensitized solar cells and the interpretation of the diffusion length*. The Journal of Physical Chemistry Letters, 2009. **1**(1): p. 450-456.
125. Diguna, L.J., et al., *High efficiency of CdSe quantum-dot-sensitized TiO₂ inverse opal solar cells*. Applied Physics Letters, 2007. **91**(2): p. 023116-023116-3.
126. Lee, H., et al., *Efficient CdSe quantum dot-sensitized solar cells prepared by an improved successive ionic layer adsorption and reaction process*. Nano letters, 2009. **9**(12): p. 4221-4227.
127. Guijarro, N., et al., *CdSe quantum dot-sensitized TiO₂ electrodes: effect of quantum dot coverage and mode of attachment*. The Journal of Physical Chemistry C, 2009. **113**(10): p. 4208-4214.
128. Mora-Seró, I., et al., *Factors determining the photovoltaic performance of a CdSe quantum dot sensitized solar cell: the role of the linker molecule and of the counter electrode*. Nanotechnology, 2008. **19**(42): p. 424007.
129. Chen, J., et al., *An oleic acid-capped CdSe quantum-dot sensitized solar cell*. Applied physics letters, 2009. **94**(15): p. 153115.
130. Giménez, S., et al., *Determination of limiting factors of photovoltaic efficiency in quantum dot sensitized solar cells: Correlation between cell performance and structural properties*. Journal of Applied Physics, 2010. **108**(6): p. 064310.
131. Trevisan, R., et al., *Harnessing infrared photons for photoelectrochemical hydrogen generation. A PbS quantum dot based "quasi-artificial leaf"*. The journal of physical chemistry letters, 2012. **4**(1): p. 141-146.
132. de la Fuente, M.S., et al., *Effect of Organic and Inorganic Passivation in Quantum-Dot-Sensitized Solar Cells*. The Journal of Physical Chemistry Letters, 2013. **4**(9): p. 1519-1525.
133. Zhang, H., et al., *Efficient CdSe quantum dot-sensitized solar cells prepared by a postsynthesis assembly approach*. Chemical Communications, 2012. **48**(91): p. 11235-11237.
134. Yu, X.-Y., et al., *Dynamic study of highly efficient CdS/CdSe quantum dot-sensitized solar cells fabricated by electrodeposition*. Acs Nano, 2011. **5**(12): p. 9494-9500.
135. Wang, S., et al., *CdS and CdSe quantum dot co-sensitized nanocrystalline TiO₂ electrode: Quantum dot distribution, thickness optimization, and the enhanced photovoltaic performance*. Journal of Power Sources, 2015. **273**: p. 645-653.

136. Blas-Ferrando, V.M., et al., *Efficient passivated phthalocyanine-quantum dot solar cells*. Chemical Communications, 2015. **51**(9): p. 1732-1735.
137. Chi, C.-F., et al., *Energy level alignment, electron injection, and charge recombination characteristics in CdS/CdSe cosensitized TiO₂ photoelectrode*. Applied Physics Letters, 2011. **98**(1): p. 012101-012101-3.
138. Hossain, M.A., et al., *Band engineered ternary solid solution CdS_xSe_{1-x}-sensitized mesoscopic TiO₂ solar cells*. Physical Chemistry Chemical Physics, 2012. **14**(19): p. 7154-7161.
139. Santra, P.K. and P.V. Kamat, *Tandem-layered quantum dot solar cells: tuning the photovoltaic response with luminescent ternary cadmium chalcogenides*. J Am Chem Soc, 2013. **135**(2): p. 877-85.
140. Tian, J., et al., *Enhanced Performance of CdS/CdSe Quantum Dot Cosensitized Solar Cells via Homogeneous Distribution of Quantum Dots in TiO₂ Film*. The Journal of Physical Chemistry C, 2012. **116**(35): p. 18655-18662.
141. Toyoda, T., et al., *Photovoltaic and Photoexcited Carrier Dynamics of Double-Layered CdS/CdSe Quantum Dot-Sensitized Solar Cells*. J. Mater. Sci. Eng., A, 2014. **3**: p. 601-608.
142. Hines, D.A. and P.V. Kamat, *Quantum Dot Surface Chemistry: Ligand Effects and Electron Transfer Reactions*. The Journal of Physical Chemistry C, 2013. **117**(27): p. 14418-14426.
143. Tang, J., et al., *Colloidal-quantum-dot photovoltaics using atomic-ligand passivation*. Nature materials, 2011. **10**(10): p. 765-771.
144. Mora-Sero, I., et al., *Recombination in quantum dot sensitized solar cells*. Acc Chem Res, 2009. **42**(11): p. 1848-57.
145. Guijarro, N., et al., *Uncovering the role of the ZnS treatment in the performance of quantum dot sensitized solar cells*. Physical Chemistry Chemical Physics, 2011. **13**(25): p. 12024-12032.
146. Shen, Q., et al., *Effect of ZnS coating on the photovoltaic properties of CdSe quantum dot-sensitized solar cells*. Journal of Applied Physics, 2008. **103**(8): p. 084304.
147. Nam, M., et al., *Efficient hybrid solar cells using PbS x Se 1- x quantum dots and nanorods for broad-range photon absorption and well-assembled charge transfer networks*. Nanoscale, 2013. **5**(17): p. 8202-8209.
148. Pang, Q., et al., *CdSe nano-tetrapods: controllable synthesis, structure analysis, and electronic and optical properties*. Chemistry of materials, 2005. **17**(21): p. 5263-5267.
149. Zarazúa, I., et al., *Impedance Analysis of CdSe Quantum Dot-Sensitized TiO₂ Solar Cells Decorated with Au Nanoparticles and P3OT*. Journal of The Electrochemical Society, 2014. **161**(3): p. H68-H74.
150. Zarazúa, I., et al., *Photovoltaic Conversion Enhancement of CdSe Quantum Dot-Sensitized TiO₂ Decorated with Au Nanoparticles and P3OT*. The Journal of Physical Chemistry C, 2011. **115**(46): p. 23209-23220.
151. Meng, K., et al., *Efficient CdS quantum dot sensitized solar cells made using novel Cu₂S counter electrode*. Journal of Power Sources, 2014. **248**: p. 218-223.
152. Santra, P.K. and P.V. Kamat, *Mn-doped quantum dot sensitized solar cells: a strategy to boost efficiency over 5%*. Journal of the American Chemical Society, 2012. **134**(5): p. 2508-2511.
153. Wu, Z., et al., *Enhanced photocurrent responses and antiphotocorrosion performance of CdS hybrid derived from triple heterojunction*. The Journal of Physical Chemistry C, 2012. **116**(23): p. 12829-12835.
154. Yu, W.W., et al., *Experimental Determination of the Extinction Coefficient of CdTe, CdSe, and CdS Nanocrystals*. Chemistry of Materials, 2003. **15**(14): p. 2854-2860.

155. Giménez, S., et al., *Improving the performance of colloidal quantum-dot-sensitized solar cells*. Nanotechnology, 2009. **20**(29): p. 295204.
156. Plass, R., et al., *Quantum Dot Sensitization of Organic-Inorganic Hybrid Solar Cells*. The Journal of Physical Chemistry B, 2002. **106**(31): p. 7578-7580.
157. Jasieniak, J., M. Califano, and S.E. Watkins, *Size-Dependent Valence and Conduction Band-Edge Energies of Semiconductor Nanocrystals*. ACS Nano, 2011. **5**(7): p. 5888-5902.
158. Polimeni, A., et al., *Temperature dependence of the optical properties of $\text{In}_x\text{Ga}_{1-x}\text{As}$ self-organized quantum dots*. Physical Review B, 1999. **59**(7): p. 5064-5068.
159. Santra, P.K. and P.V. Kamat, *Tandem-Layered Quantum Dot Solar Cells: Tuning the Photovoltaic Response with Luminescent Ternary Cadmium Chalcogenides*. Journal of the American Chemical Society, 2013. **135**(2): p. 877-885.
160. Cerdan-Pasaran, A., et al., *Photovoltaic properties of multilayered quantum dot/quantum rod-sensitized TiO₂ solar cells fabricated by SILAR and electrophoresis*. Physical Chemistry Chemical Physics, 2015. **17**(28): p. 18590-18599.
161. Wang, J., et al., *Core/Shell Colloidal Quantum Dot Exciplex States for the Development of Highly Efficient Quantum-Dot-Sensitized Solar Cells*. Journal of the American Chemical Society, 2013. **135**(42): p. 15913-15922.
162. Salant, A., et al., *Quantum Rod-Sensitized Solar Cell: Nanocrystal Shape Effect on the Photovoltaic Properties*. Nano Letters, 2012. **12**(4): p. 2095-2100.
163. Zhao, K., et al., *Boosting Power Conversion Efficiencies of Quantum-Dot-Sensitized Solar Cells Beyond 8% by Recombination Control*. Journal of the American Chemical Society, 2015. **137**(16): p. 5602-5609.
164. Bailey, R.E. and S. Nie, *Alloyed Semiconductor Quantum Dots: Tuning the Optical Properties without Changing the Particle Size*. Journal of the American Chemical Society, 2003. **125**(23): p. 7100-7106.
165. Lewis, E., et al. *Probing the core-shell-shell structure of CdSe/CdTe/CdS type II quantum dots for solar cell applications*. in *Journal of Physics: Conference Series*. 2014. IOP Publishing.
166. Shen, H., et al., *Size- and Shape-Controlled Synthesis of CdTe and PbTe Nanocrystals Using Tellurium Dioxide as the Tellurium Precursor*. Chemistry of Materials, 2010. **22**(16): p. 4756-4761.
167. He, Z., et al., *Enhanced power-conversion efficiency in polymer solar cells using an inverted device structure*. Nature Photonics, 2012. **6**(9): p. 591-595.
168. Schmid, M., et al., *Modeling plasmonic scattering combined with thin-film optics*. Nanotechnology, 2011. **22**(2): p. 025204.
169. Cao, X., P. Chen, and Y. Guo, *Decoration of textured ZnO nanowires array with CdTe quantum dots: enhanced light-trapping effect and photogenerated charge separation*. The Journal of Physical Chemistry C, 2008. **112**(51): p. 20560-20566.
170. Huang, F., et al., *Dual-Function Scattering Layer of Submicrometer-Sized Mesoporous TiO₂ Beads for High-Efficiency Dye-Sensitized Solar Cells*. Advanced Functional Materials, 2010. **20**(8): p. 1301-1305.
171. Ihara, M., M. Kanno, and S. Inoue, *Photoabsorption-enhanced dye-sensitized solar cell by using localized surface plasmon of silver nanoparticles modified with polymer*. Physica E: Low-dimensional Systems and Nanostructures, 2010. **42**(10): p. 2867-2871.
172. Tian, J. and G. Cao, *Semiconductor quantum dot-sensitized solar cells*. Nano reviews, 2013. **4**.

173. Fabregat-Santiago, F., et al., *Characterization of nanostructured hybrid and organic solar cells by impedance spectroscopy*. Physical Chemistry Chemical Physics, 2011. **13**(20): p. 9083-9118.
174. Peter, L.M., et al., *Band-edge tuning in self-assembled layers of Bi₂S₃ nanoparticles used to photosensitize nanocrystalline TiO₂*. The Journal of Physical Chemistry B, 2003. **107**(33): p. 8378-8381.
175. Jiang, J., et al., *Morphogenesis and crystallization of Bi₂S₃ nanostructures by an ionic liquid-assisted templating route: synthesis, formation mechanism, and properties*. Chemistry of materials, 2005. **17**(24): p. 6094-6100.
176. Jovanovski, V., et al., *A Sulfide/Polysulfide-Based Ionic Liquid Electrolyte for Quantum Dot-Sensitized Solar Cells*. Journal of the American Chemical Society, 2011. **133**(50): p. 20156-20159.
177. Bisquert, J., et al., *A review of recent results on electrochemical determination of the density of electronic states of nanostructured metal-oxide semiconductors and organic hole conductors*. Inorganica Chimica Acta, 2008. **361**(3): p. 684-698.
178. Guijarro, N., et al., *Direct correlation between ultrafast injection and photoanode performance in quantum dot sensitized solar cells*. The Journal of Physical Chemistry C, 2010. **114**(50): p. 22352-22360.
179. Kojima, A., et al., *Organometal halide perovskites as visible-light sensitizers for photovoltaic cells*. Journal of the American Chemical Society, 2009. **131**(17): p. 6050-6051.
180. Im, J.-H., et al., *6.5% efficient perovskite quantum-dot-sensitized solar cell*. Nanoscale, 2011. **3**(10): p. 4088-4093.
181. Kim, H.-S., et al., *Lead iodide perovskite sensitized all-solid-state submicron thin film mesoscopic solar cell with efficiency exceeding 9%*. Scientific reports, 2012. **2**: p. 591.
182. Lee, M.M., et al., *Efficient hybrid solar cells based on meso-superstructured organometal halide perovskites*. Science, 2012. **338**(6107): p. 643-647.
183. Edri, E., et al., *High open-circuit voltage solar cells based on organic-inorganic lead bromide perovskite*. The journal of physical chemistry letters, 2013. **4**(6): p. 897-902.
184. Heo, J.H., et al., *Efficient inorganic-organic hybrid heterojunction solar cells containing perovskite compound and polymeric hole conductors*. Nature Photonics, 2013. **7**(6): p. 486-491.
185. Abrusci, A., et al., *High-performance perovskite-polymer hybrid solar cells via electronic coupling with fullerene monolayers*. Nano letters, 2013. **13**(7): p. 3124-3128.
186. Burschka, J., et al., *Sequential deposition as a route to high-performance perovskite-sensitized solar cells*. Nature, 2013. **499**(7458): p. 316-319.
187. Baena, J.P.C., et al., *Highly efficient planar perovskite solar cells through band alignment engineering*. Energy & Environmental Science, 2015. **8**(10): p. 2928-2934.
188. Zhang, F., et al., *Brightly Luminescent and Color-Tunable Colloidal CH₃NH₃PbX₃ (X = Br, I, Cl) Quantum Dots: Potential Alternatives for Display Technology*. ACS Nano, 2015. **9**(4): p. 4533-4542.
189. Wei, M., et al., *Highly luminescent and stable layered perovskite as the emitter for light emitting diodes*. physica status solidi (a), 2016.
190. Song, J., et al., *Quantum Dot Light-Emitting Diodes Based on Inorganic Perovskite Cesium Lead Halides (CsPbX₃)*. Advanced Materials, 2015. **27**(44): p. 7162-7167.
191. Yan, J., et al., *Improving the Photoluminescence Properties of Perovskite CH₃NH₃PbBr_{3-x}Cl_x Films by Modulating Organic Cation and Chlorine Concentrations*. ACS Applied Materials & Interfaces, 2016. **8**(20): p. 12756-12763.

192. Shamsi, J., et al., *Colloidal Synthesis of Quantum Confined Single Crystal CsPbBr₃ Nanosheets with Lateral Size Control up to the Micrometer Range*. Journal of the American Chemical Society, 2016. **138**(23): p. 7240-7243.
193. Protesescu, L., et al., *Nanocrystals of cesium lead halide perovskites (CsPbX₃, X= Cl, Br, and I): novel optoelectronic materials showing bright emission with wide color gamut*. Nano letters, 2015. **15**(6): p. 3692-3696.
194. Ahn, N., et al., *Highly Reproducible Perovskite Solar Cells with Average Efficiency of 18.3% and Best Efficiency of 19.7% Fabricated via Lewis Base Adduct of Lead(II) Iodide*. Journal of the American Chemical Society, 2015. **137**(27): p. 8696-8699.